Study of the Consolidation Process under Macro- and Microscopic Thermal Effects in Selective Laser Sintering and Selective Laser Melting

THÈSE N^{O} 4609 (2010)

PRÉSENTÉE LE 17 MARS 2010
À LA FACULTÉ SCIENCES ET TECHNIQUES DE L'INGÉNIEUR
LABORATOIRE DE GESTION ET PROCÉDÉS DE PRODUCTION
PROGRAMME DOCTORAL EN SYSTÈMES DE PRODUCTION ET ROBOTIQUE

ÉCOLE POLYTECHNIQUE FÉDÉRALE DE LAUSANNE

POUR L'OBTENTION DU GRADE DE DOCTEUR ÈS SCIENCES

PAR

Jamasp JHABVALA

acceptée sur proposition du jury:

Prof. M.-O. Hongler, président du jury
Prof. R. Glardon, Dr E. Boillat, directeurs de thèse
Dr A. Jacot, rapporteur
P. Mognol, rapporteur
Dr V. Romano, rapporteur

ÉCOLE POLYTECHNIQUE
FÉDÉRALE DE LAUSANNE

Suisse
2010

Remerciements

Je remercie tout d'abord mes deux directeurs de thèse, Rémy Glardon et Eric Boillat, de m'avoir offert l'occasion d'effectuer ce travail dans une ambiance sereine et laissé beaucoup d'indépendance, tout en se rendant disponibles lorsqu'il le fallait. Je remercie également les membres de mon jury de thèse, Valerio Romano, Pascal Mognol, Alain Jacot et Max Hongler, pour leur soutien et commentaires lors de ce travail.

Ce travail a en partie été financé par le programme INTERREG IIIA Nr. 54/AJ/9.1/4. Merci aux partenaires de ce projet à l'ENSMM de Besançon, Guillaume Vansteenkiste, Nathalie Boudeau et Claude Roques-Carmes.

Merci également à mes collègues ayant travaillé sur le sujet: Cédric André, Alla Lozinskaya, Marc Matthey, François Girardet et Serguei Kolossov, ainsi qu'à ceux de l'équipe de gestion de production que j'ai côtoyés lors d'activités plus ou moins scientifiques: Souleiman Naciri, Grégoire Pépiot, Luca Canetta, Min-Yung Yoo. Merci à Ruth Fiaux et Claire Chabanel pour leur aide dans les méandres administratifs de l'EPFL. Je remercie en outre Marzio Bergomi et Florian Charrière pour repas divers et conversations philosophiques sur le sens de la vie.

Je remercie les mécaniciens de l'atelier pour les nombreuses modifications et réalisations effectuées sur le laser.

Je tiens également à remercier Mélanie Dafflon et Benoit Lorent du LSRO2 pour leurs idées et soutien lors de l'utilisation du robot Delta3 et le Prof. Clavel pour m'en avoir accordé les accès.

Les photos au microscope électronique se trouvant dans ce travail ont été réalisées au CIME à l'EPFL. Merci à Marco Cantoni, Fabienne Bobard et Emmanuelle Boehm-Courjaut pour leur aide dans ce domaine. Merci à la société Keyence et à Jan Stauffiger pour les photos et mesures de la section 5.5.1.

Durant cette thèse, j'ai eu l'occasion d'encadrer de nombreux étudiants dont les projets de semestre ou de master ont contribué au résultat final: Gabriel Capel-Lopez, Jean-Matthieu Belzung, Henning Mohr, Julien Moulin, Raphaël Moillen, Alain Michaël, Ivan Lasan, Thibaud Antignac, Giulia Spinato, Claude Loosli.

Je remercie enfin mes parents, frère, famille, amis et artistes qui ont supporté mes sautes d'humeur pendant ces cinq dernières années, et en particulier Stefaan qui est mon plus ancien ami et Annika, la plus belle.

Abstract

Selective Laser Sintering (SLS) and Selective Laser Melting (SLM) are parent Additive Manufacturing processes using a laser to solidify metallic, ceramic, polymer or composite powders. During the process, the object is built layer by layer. A laser source is responsible for the consolidation, by local heating. The light is deviated by a scanning head according to the instructions of an STL file. Then partial fusion of the particles takes place, followed by a solidification of the liquid created. Kinetics of these steps are very high and play an important role in the final microstructure (rearrangement of the particles, pore creation, residual stresses). In the case of polymers and composites the technique is now well understood and widely used, but for metals and ceramics it suffers from a lack of precision, surface roughness and poor mechanical properties.

The goal of this Ph.D. work is to understand the effect of the thermal gradients on the consolidation process, using different laser parameters (power, pulse frequency, scan speed,...).

In SLS, microscopic thermal gradients arise, due to the fact that the laser is pulsed and that only the exterior of the powder particles is molten. A thermal model to describe the interaction between a laser beam and a (spherical) grain is proposed. This model allows for the incorporation of the latent heat of fusion and for a realistic surrounding. The absorbed laser intensity is modeled by means of the Mie theory. Experiments where two particles of powder are isolated and illuminated by the laser are carried out in order to measure the interparticular necks and the volume of liquid formed for different repetition rates. The thermal model leads to good predictions of the particles final sintering state.

Fluid flow models are investigated in order to determine the dynamic of the molten liquid. The main issue is to explain the capillary flow mechanisms leading from the molten material to the neck formation. Two models are derived to simulate the fluid flow between the particles. The first one simulates a capillary flow between two parallel plates. The second one deals with energetic considerations arising from Frenkel's principle. In both cases, the final output is the liquid lifetime necessary to get the interparticular neck lengths experimentally observed. We point out that the two models predict the same liquid lifetime, although they are derived with different hypotheses.

In SLM, continuous lasers are used and one has to deal with macroscopic thermal gradients, since the particles are completely molten. A very high laser power is used and the negative thermal effects (like thermal stresses or balling effects) are important. A solution to control them is to adjust the scanning strategy. Four scanning strategies are investigated for material with different thermal conductivities. The three-dimensional model used to describe the laser-matter interactions and the temperature evolution of the scanned powder bed allows for a finite latent heat (Stefan-problem) and for conductivity modifications due to the consolidation. We show that this finite element thermal model can be efficiently used to anticipate most of the problems (like cracks or balling) arising in practice. The benefit of avoiding thermal gradients is shown, in particular by EBSD analysis.

Finally, applications of the SLS/SLM technique on different pieces built during this work are shown. A new way to build support structure is also proposed.

Keywords: Selective Laser Sintering, Selective Laser Melting, metallic powder, consolidation, thermal gradients, thermal model, finite elements, interparticular neck, fluid flow, capillary, Frenkel, scanning strategies, support structure

Résumé

Le frittage sélectif par laser (SLS) et la fusion sélective par laser (SLM) sont des procédés apparentés de fabrication additive utilisant un laser pour solidifier des poudres métalliques, céramiques, polymères ou composites. Au cours du processus, l'objet est construit couche par couche. Une source laser est responsable de la consolidation, par chauffage local. La lumière est déviée par une tête scanner conformément aux instructions d'un fichier STL. On assiste ensuite à une fusion partielle des particules, suivie par une solidification du liquide créé. Les cinétiques de ces étapes sont très élevées et ont un impact important sur la microstructure finale (réarrangement des particules, création des pores, contraintes résiduelles). Dans le cas des polymères et composites, la technique est maintenant bien comprise et largement utilisée, mais en ce qui concerne les métaux et céramiques, elle souffre d'un manque de précision, de rugosité de surface et de pauvres propriétés mécaniques. L'objectif de ce travail de thèse est de comprendre l'effet des gradients thermiques sur le processus de consolidation, à l'aide de différents paramètres du laser (puissance, fréquence de pulse, vitesse de balayage).

En SLS, des gradients thermiques microscopiques apparaissent, car le laser est pulsé et seulement l'extérieur des particules de poudre est fondu. Un modèle thermique pour décrire l'interaction entre un faisceau laser et un grain (sphérique) est proposé. Ce modèle permet l'utilisation d'une chaleur latente de fusion non-nulle et d'un environnement réal-

iste. L'intensité du laser absorbée est modélisée au moyen de la théorie de Mie. Des expériences où deux particules de poudre sont isolées et illuminées par le laser sont effectuées afin de mesurer les cous interparticulaires et le volume du liquide formé pour différentes fréquences de répétition. Le modèle thermique conduit à de bonnes prédictions du taux de frittage final des particules.

Des modèles d'écoulement de fluide sont ensuite étudiés afin de déterminer la dynamique du liquide en fusion. Le principal problème est d'expliquer les mécanismes capillaires conduisant de la matière en fusion à la formation du cou. Deux modèles sont dérivés afin de simuler l'écoulement du fluide entre les particules. Le premier simule un écoulement capillaire entre deux plaques parallèles. Le deuxième provient de considérations énergétiques découlant du principe de Frenkel. Dans les deux cas, l'information récoltée est la durée de vie du liquide nécessaire à l'obtention du cou interparticulaire observé expérimentalement. Nous soulignons que les deux modèles prédisent la même durée de vie du liquide, bien qu'elles soient obtenues à l'aide d'hypothèses différentes.

En SLM, des lasers continus sont utilisés, engendrant des gradients thermiques macroscopiques, puisque la particule entière est en fusion. Une très forte puissance laser est utilisée et les effets thermiques négatifs (comme les contraintes thermiques ou les effets de balling) sont importants. Une solution pour les contrôler est d'ajuster la stratégie de balayage. Quatre stratégies de balayages sont étudiées pour des matériaux de différentes conductivités thermiques. Le modèle 3D utilisé pour décrire les interactions laser-matière et l'évolution de la température du lit de poudre permet d'intégrer une chaleur latente finie (problème de Stefan) et des modifications de conductivité dues à la consolidation. Nous montrons que ce modèle en éléments finis peut être utilisé de manière efficace afin d'anticiper la plupart des problèmes qui se posent en pratique (fissures, balling). L'intérêt d'éviter des gradients thermiques est démontré, notamment par analyse EBSD.

Enfin, des applications de la technique SLS / SLM sont présentées pour différents objets construits au cours de ce travail. Une nouvelle façon de bâtir des structures de support est également proposée.

Mots-clés: frittage sélectif par laser, fusion sélective par laser, poudre métallique, consolidation, gradients thermiques, modèle thermique, éléments finis, cou interparticulaire, écoulement de fluide, capillaire, Frenkel, stratégies de balayage, structure de supports

Contents

List of Figures

List of Tables

List of Symbols

Roman

a	Interparticular neck length
b	Particles center displacement
Bi	Biot number
Bo	Bond number
Ca	Capillary number
C_p	Specific heat
E	Laser energy
e	Layer height
F	Force
f	Pulse frequency
Fo	Fourier number
g	Acceleration due to gravity
h	Distance between plates
h_0	Initial distance between plates
h_f	Final distance between plates
h_d	Hatching distance
I_0	Laser intensity
k	Thermal conductivity

L	Latent heat of fusion
M^2	Beam quality factor
M_p	Mass of one plate
P	Laser power
Q	Volumetric flow rate
R	Radius of the fluid cylinder between plates
R_0	Initial radius of the fluid cylinder between plates
R_f	Final radius of the fluid cylinder between plates
r	Radius of the particle
s	Lateral surface of the system
S	Sintering rate
T	Temperature
T_0	Heat sink temperature
T_∞	Asymptotic temperature
T_m	Melting temperature
T_{th}	Threshold temperature
t	Time
t_c	Time constant
t^*	Critical time for fusion
t_f	Final time
U	Contact line speed
V	Neck volume
v	Scan speed (or velocity in Chapter 4)
w_a	Weight in air
w_h, w_v	Chessboard unit cell width
w_p	Paintbrush scan width
w_{xw}	Weight in water with xylene
w_{xa}	Weight in air with xylene
w_w	Weight in water

Greek

α	Absorption coefficient
α_s	Surface absorption
γ_{SL}	Surface tension between solid and liquid
γ_{LG}	Surface tension between liquid and gas
γ_{SG}	Surface tension between solid and gas
ΔP	Pressure difference
ε	Dielectric constant
θ_D	Dynamic angle
θ_E	Equilibrium angle
κ	Heat transfer coefficient
λ	Wavelength
μ	Dynamic viscosity
ω	Spot size
ρ	Density
τ	Characteristic time

List of Abbreviations

3DP	3D Printing
BSE	BackScattered Electrons
CCP	Cubic Close Packing
DLP	Digital Light Processing
DMD	Direct Metal Deposition
DMLS	Direct Metal Laser Sintering
EBM	Electron Beam Melting
EBSD	Electron BackScattered Diffraction
FDM	Fused Deposition Modeling
HCP	Hexagonal Close Packing
LENS	Laser Engineered Net Shaping
MEM	Melted Extrusion Modeling
RP	Rapid Prototyping
SEM	Scanning Electron Microscopy
SLA	Stereolithography
SLS	Selective Laser Sintering
SLM	Selective Laser Melting
SMS	Selective Mask Sintering
SE	Secondary Electrons
UC	Ultrasonic Consolidation

Chapter 1

Overview

1.1 Additive Manufacturing

Additive Manufacturing is the name given to a host of related technologies used to create physical objects by sequential deposition of material layers. It was formerly named Rapid Prototyping (RP) since the produced parts couldn't be useable products. Today parts as molds or tools can be produced by these techniques also known by the names Additive Fabrication, Three Dimensional Printing, Solid Freeform Fabrication, Direct Fabrication, Direct Manufacturing, Rapid Manufacturing and Digital Manufacturing [1]. The originality of Additive Manufacturing is that material is added to form the part desired and not subtracted from a bigger part. All the non-used material can be recycled in the next construction.

The automated fabrication based on sliced 3D CAD files allows more three-dimensional freedom, complying with modern design requirements. The number of operations is decreased, while the overall efficiency of industrialization increases. Fabrication times are not sensitive to complexity, but only to the consolidated material volume [2] [3]. The fabrication of small and complex parts with freeform features can be achieved: shapes that may not be realizable by conventional machining can be built by these techniques, such as conformal cooling channels in injection molds (see figure 1.1) [4].

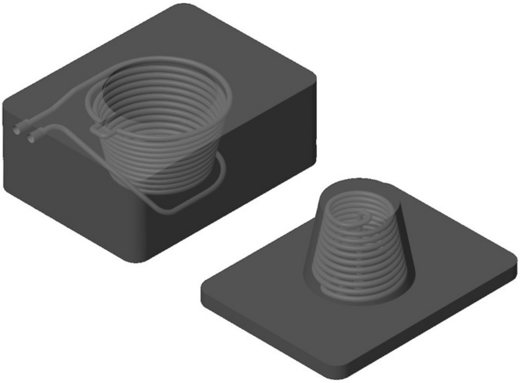

Figure 1.1: Mold with conformal cooling channels

Other advantages like the gain of time and money when dealing with small series and the possibility to use multiple materials have also contributed to the rise of these technologies.

These properties have resulted in their wide use as a way to reduce time to market in manufacturing. Today's systems are heavily used by engineers to better understand and communicate their product designs as well as to make rapid tooling to manufacture those products. Surgeons, architects, artists and individuals from many other disciplines also routinely use the technology.

The process steps for all Additive Manufacturing techniques are the following:

- creation of a 3D CAD model of the part (figure 1.2(a))
- export in STL format to the process planning software which generates the slicing of the part into thin layers and the scanning path for each layer (figure 1.2(b) and 1.2(c))
- use the Additive Manufacturing machine to build the part (figure 1.2(d))

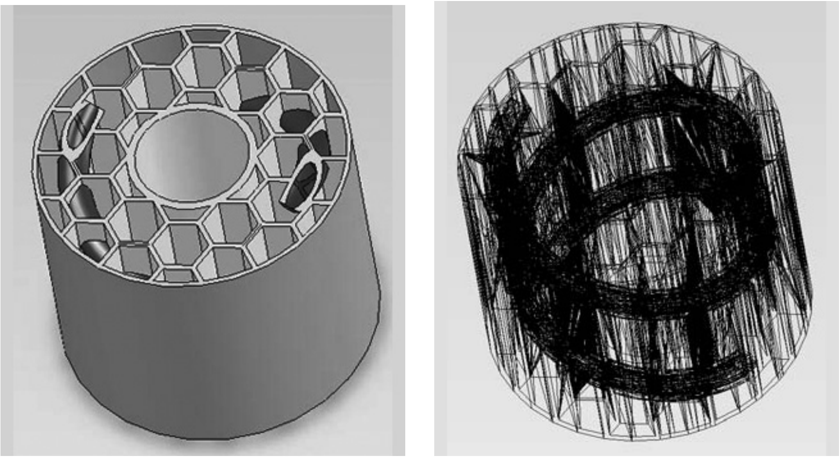

(a) CAD file (b) STL file

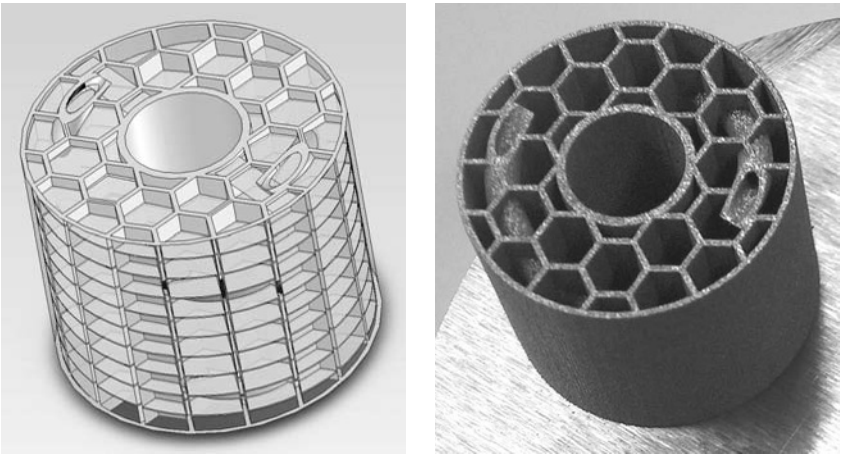

(c) sliced STL file (d) Final part

Figure 1.2: Additive Manufacturing techniques process steps (images taken from [5])

Many different techniques have arisen from this simple scheme, and due to the constant innovation and mutation in existing technologies it is difficult to get an exhaustive classification. However here is an attempt to sort the additive manufacturing technologies and related companies existing in 2009 [6][7]:

- **Stereolithography (SLA)**: 3D systems, DWS
- **3D Printing (3DP)**: 3D systems, Desktop Factory, Ex One, Mcor, MTT (SLP), Objet Geometries, Solido, Solidscape, Voxeljet, Z corp
- **Selective Laser Sintering (SLS) / Selective Laser Melting (SLM)**: 3D Systems, Concept laser, EOS, MTT, Phénix Systems, ReaLizer
- **Laser Fusing**: Accufusion, Optomec (LENS), POM (DMD)
- **Fused Deposition Modeling Process**: Fab@Home, RepRap, Stratasys (FDM), Beijing Yinhua (MEM)
- **Digital Light Processing (DLP)**: Envisiontec, Araldite Digitalis (Huntsman)
- **Electron Beam Melting (EBM)**: Arcam
- **Selective Mask Sintering (SMS)**: Sintermask
- **Ultrasonic Consolidation (UC)**: Solidica

Benchmarking of some of these techniques have been made in [8] in terms of geometrical accuracy and mechanical properties.

1.2 Selective Laser Sintering

Selective Laser Sintering (SLS) is an Additive Manufacturing process using a laser to solidify metallic, ceramic, polymer or composite powders. It was developed and patented by Dr. Deckard from the University of Texas at Austin in 1986. The process is schematically described in figure 1.3

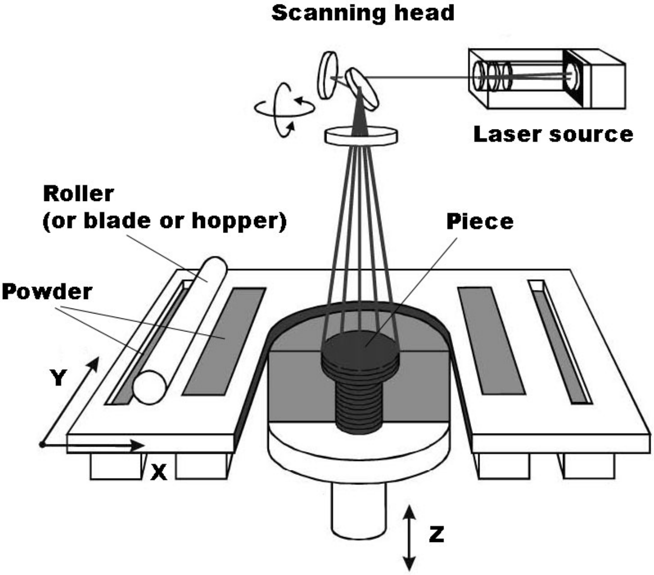

Figure 1.3: The SLS process (image modified from [9])

In the case of polymers and composites the technique is now well understood and widely used, but for metals and ceramics it suffers from a lack of precision, surface roughness and poor mechanical properties. During the process, the object is built layer by layer. A laser source is responsible for the consolidation, by local heating. The light is deviated by a scanning head according to the instructions of the STL file. Then partial fusion of the particles takes place, followed by a solidification of the liquid created. Kinetics of these steps are very high and play a important role in the final microstructure (rearrangement of the particles, pore creation, residual stresses).

The deposition of the powder is a crucial point for high density and good mechanical properties of the final part [3]. Spherical particles ensure the best powder flowability as well as a good powder bed density.

Most SLS machines use a blade or a roller. A hopper is also a possibility. Additional pressing of the powder during the deposition is always beneficial.

The SLS processes can be classified in two categories [9] :

1.2.1 Different binder and structural materials

The structural material can be a metal as well as a ceramic material. The binder materials however are mostly polymers or low fusion point metallic materials. Binder particles are usually much smaller than the structural ones. Therefore, the high surface-to-volume ratio of the grains - in combination with their relatively low melting point - favors the preferential melting of the binder material [3]. The structural and binder material can be separate grains, composite grains or coated grains.

1.2.2 No distinct binder and structural material

When the heat supplied to a powder particle is insufficient to melt the whole particle, only a shell at the grain border is molten. The core of the grain stays solid. In that way the molten material acts as a binder between the non-molten particle cores. This binding mechanism can arise with metals as well as with polymers, although the consolidation of polymer powders results also from other mechanisms (consolidation at the glass transition temperature, which is lower than the melting temperature, polymer chain rearrangement and cross-linking). The partial melting phenomenon has been modeled using a simple thermal model [3]. Skin and core temperatures of the powder particles were calculated. In this way the minimal pulse energy to fully melt the particle can be calculated. Below this value, the core temperature never exceeds the melting temperature and only partial melting is obtained. This technique is sometimes called Direct Metal Laser Sintering (DMLS).

1.3 Selective Laser Melting

Selective Laser Melting (SLM) is essentially the same process, with the difference that the particles are completely molten under the laser beam and form a liquid bath. This development was driven by the need to produce near full dense objects, with mechanical properties comparable to those of bulk materials and by the desire to avoid post processing cycles. But due to the difficulty to find process-windows, the range of commercially available SLM metals is limited today [9]. The powder can be a single material powder (pure Titanium [10])), an alloyed material powder (stainless steel, chrome-cobalt, Inconel,... [11] [12]) or a mixture of powders. This technique is already widely used in different fields such as aerospace, machinery, medical and dental applications, art and jewelry [6].

A benchmark study on pieces made by SLS with polymer binder, SLS with metallic binder and SLM has been achieved in [13].

1.4 Problematic

The physical phenomena involved in Selective Laser Sintering and Melting are at the border of several scientific fields:

- light propagation and electromagnetism for the interaction between the laser and the metal
- fluid mechanics for the dynamic of the liquid formed
- solid mechanics and heat transfer
- solidification and phase transformation
- chemistry and powder processing

To understand the phenomena involved in the process, several theoretical models must be taken into account. One has to know which simplifications and hypotheses can be made and what are their relative effects on the entire model. The goal is to get simple tools describing the laser sintering/melting process.

Many experiments have been made during this work, involving different materials and powder sizes, in order to verify the simulations, and to get some universal laws for any material or powder size.

1.5 Previous works in *Laboratoire de Gestion et Procédés de Production* (LGPP)

In 2002 Nakis Karapatis [3] proposed "A Sub-Process approach of Selective Laser Sintering". The objective of this study was to present a wide overview of the processes governing Selective Laser Sintering, on the basis of experimental data and conceptual models. Three subprocesses were identified in the SLS cycle: powder layer preparation, energy transfer from laser to powder with thermalization, and consolidation.

In 2005 Serguei Kolossov [14] developped a "Non-Linear Model and Finite Element Simulation of the Selective Laser Sintering Process". In this thesis, a theoretical model of the process is developed. This model considers the laser-matter interaction, the non-linear heat diffusion and the phase transformations. The evolution of the material properties due to the sintering phenomena is analyzed by a microscopic sub-model. For solving the governing equations, a numerical method based on finite element analysis is proposed. A combination of non-conformal adaptive mesh for space discretization with a Chernoff's scheme for time discretization is used. The results of the numerical simulations are compared to experimental results. In particular the temperature field evolution predicted by the model is validated by experimental measurements performed with an infra-red camera.

In 2007 Cédric André [15] submitted his work "Modélisation quantitative du procédé de frittage sélectif par laser: relation paramètres/ microstructure". The main goal of this thesis was to improve the understanding of the DMLS manufacturing process in order to be able to make parts that could be used without post-processing. A microstructural index η is defined. This index is an adimensional number between 0 and 1 and represents the degree of sintering (η is close to 0 if the sintering process has just begun, η tends towards 1 if the sample's density is close to full density).

This index permits to characterize quantitatively the microstructure of all the parts built by the DMLS process. In this work, three key parameters are identified : the pulse duration, the energy density of the laser and the powder bed density. Cédric André developed phenomenological models predicting that the microstructure of a monolayer becomes finer if the pulse duration as well as the powder bed density increase and if the energy density of the laser decreases.

1.6 Structure of this work

The structure of this work is the following. The experimental setups used are described in Chapter 2. This includes the setup used to build parts (the SLS/SLM station, the powders and the substrates) as well as the systems used for manipulation and analysis (the Delta3 robot, the scanning electron microscope (SEM) and the density measurements).

Chapters 3 and 4 are about SLS and focus on microscopic phenomena: the formation of liquid necks between two particles and their dynamics when spreading and solidifying. Since the laser is pulsed, the absorption of light in the particles and the formation of liquid are complicated and the absorbing media cannot be modelized as continuous. Microscopic simulations are used in this case.

Chapter 5 is about SLM and macroscopic phenomena on the powder bed. Here the laser is used in continuous mode. The powder bed is modeled as homogeneous and macroscopic simulations can be used.

Chapter 6 describes the application of the SLS/SLM technique on different pieces built during this work. A new way to build support structure for the pieces is also proposed.

Chapter 2

Experimental setup

2.1 The SLS/SLM experimental platform

The installation consists of a laser, a vacuum chamber containing the deposition systems and a computer piloting both (see figure 2.1).

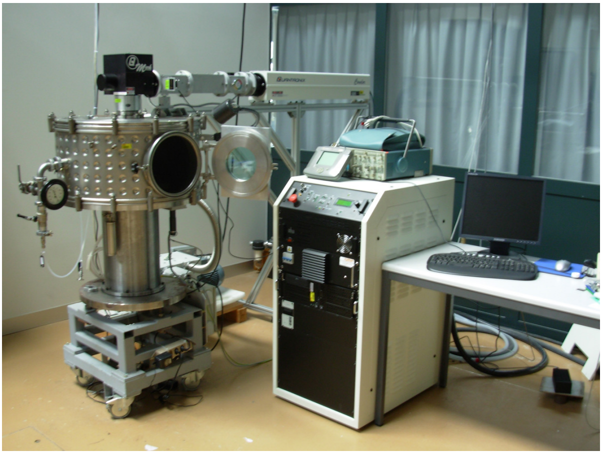

Figure 2.1: The SLS/SLM experimental platform

2.1.1 The laser

The laser is a Nd:YAG (Quantronix Condor) operating with an average power of 100 W. It can be used either in continuous mode or in pulsed mode (repetition rate: 2 to 50 kHz and pulse duration: ∼225 ns). In normal mode (multimode) the focal beam radius is ∼150 μm (M^2=13). A diaphragm can be introduced on the laser beam path. In that case, the focal beam reduces to ∼100 μm and the laser beam shape is gaussian ($M^2 < 1.3$).

A dedicated software pilots the laser. The power can be adjusted by changing the lamp current. The range of reachable powers goes from 10 W to 100 W. The pulse frequency and the scanning speed can be controlled as well.

A scanner head with galvanometric mirrors deflects the laser beam according to computer instructions.

Several optical elements are mounted between the laser and the scanning head. They are divided in three blocks (see figure 2.2) .

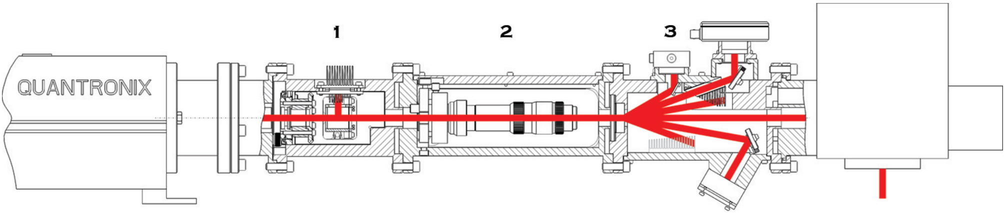

Figure 2.2: Optical elements on the beam path

1. A block containing a polarizer, a 1/2 wavelength plate and a beam splitter permits to reach powers lower than 10 W. The polarized light is rotated by the 1/2 wavelength plate and the beam splitter cuts one component of the electrical field. The adjustment of the 1/2 wavelength plate allows to control the laser power between 0W and the value determined by the lamp current.

2. A Π-shaper (Moltech 6-6-532/1064) transforms the laser intensity profile into a top-hat one (see figure 2.3). The input beam intensity profile has to be gaussian. This optical element can only be used with the diaphragm introduced on the laser beam path, due to its small input diameter.

Figure 2.3: Π-shaper

3. A holographic beam-splitter (Gentec HBS-1064-100-1C-10) splits the beam into several parts. The primary beam is left quite unaffected, but small amount of energies are deviated according to different angles.

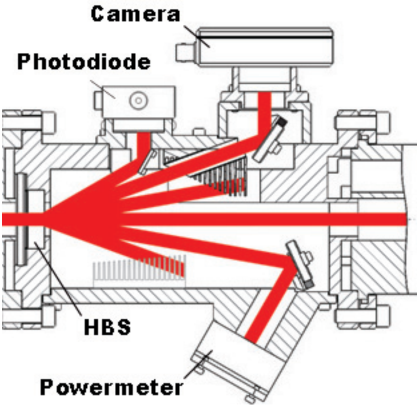

Figure 2.4: The holographic beam splitter (HBS) and the beam characterization devices

Three of these secondary beams are focused on different measuring devices (see figure 2.4): 1% of the beam is focused on a powermeter (Gentec), to measure the power during the experiments. A camera (Gentec Beamage) allows a control of the beam intensity profile. Finally a photodiode (Thorlabs DET10A/M) measures the pulse duration. Black computer heatsinks are put on the non-used deviated beams in order to evacuate heat.

2.1.2 The chamber

The deposition chamber is made of stainless steel. A vacuum pump permits to reach $5 \cdot 10^{-2}$ mbar. Argon can then be reinjected inside to avoid possible reactions with the atmosphere.

Two motors (Maxon DC 118778) control the system. One of them is lowering the work table, while the other one controls the deposition system via a strap (see figure 2.5).

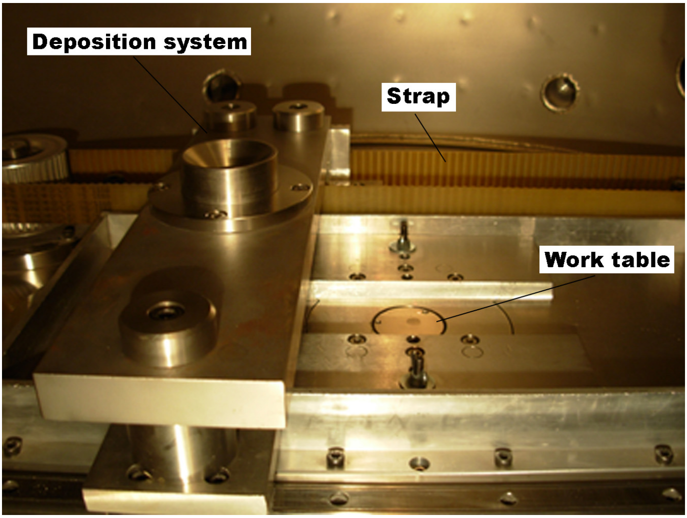

Figure 2.5: The chamber and deposition system

2.1.3 The deposition system

The powder is deposited by a hopper with an inner angle of 45° to achieve good layers.

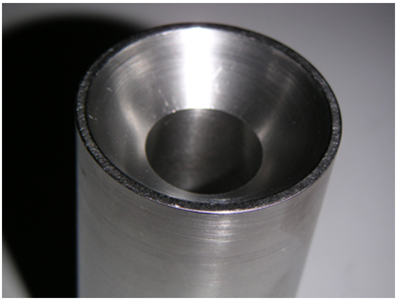

Figure 2.6: The hopper

In this way the maximum density reachable is 64 % which is the density of a random packed bed of monosized spheres. The maximum density with monosized spheres can reach 74% with a CCP or HCP structure, but these structures are not stable and any perturbation will break them.
In general the powder is not monosized but multisized. Therefore the powder bed cannot be fully packed and the density is in general lower than 64 %. An idea to improve this density is to use bimodal powders. The study of the best way to improve density using multimodal spheric powders is called Apollonian packing. It is named after the Greek mathematician Apollonius of Perga. It follows the Apollonian gasket or Apollonian net which is a fractal generated from triples of circles, where any circle is tangent to two others. Figure 2.7 from [16] shows a dense packing using Apollonian packing.

Table 2.1 lists the size ratios to get a maximally dense N-component sphere mixture [17] [18].

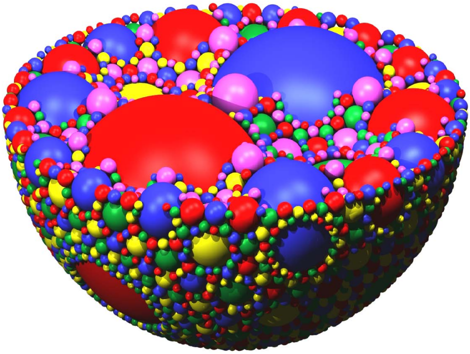

Figure 2.7: Apollonian sphere packing from [16]

N	size ratio(s)
1	1
2	1:77
3	1:7:77
4	1:7:38:316

Table 2.1: Size ratios of Apollonian packing

In general the 1:7 is the only reachable ratio when dealing with powders suitable for SLS/SLM.

Another possibility to get a better density is to press the powder before illumination. A specific deposition system has been developed to allow pressing the powder bed before illumination (see figure 2.8).

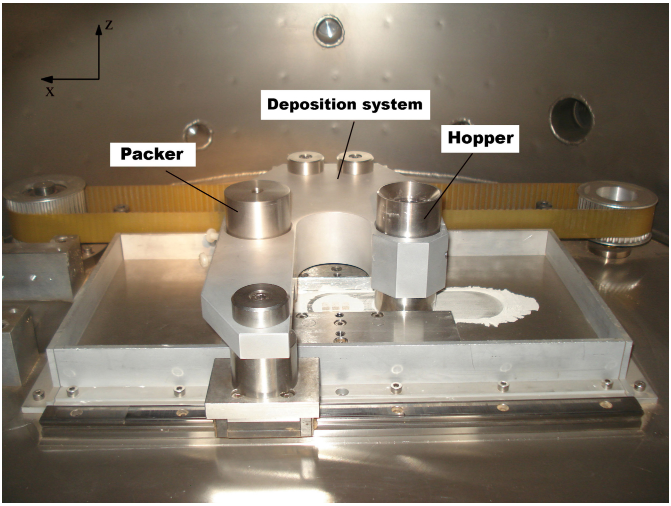

Figure 2.8: The deposition system with packer

2.2 The substrates

Substrates are needed to build SLS pieces. Their role consists in avoiding deformation of the part caused by the thermal stresses induced by the laser. They also stabilize the piece when the hopper deposits powder. Usually the substrates are made in a material leading to a good wettability of the used powder. In this work, substrates made of EOS type bronze powder and sintered with the EOSint M250 machine are used. They ensure a good bonding with most metallic materials used, due to their heat evacuation capability and their native porosity.

The EOS bronze powder is a mixture of Cu, Sn, Ni, and P forming different phases as shown in figure 2.9. The different phases visible on this figure are: 1) nickel 2) porosity 3) Cu-Sn-P 4) CuP 5) CuSn.

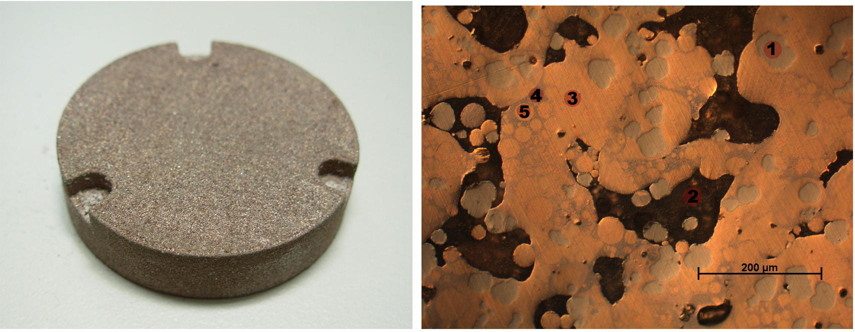

Figure 2.9: The EOS substrate and its different phases (1: nickel, 2: porosity, 3: Cu-Sn-P, 4: CuP, 5: CuSn)

Experiments with gold powder (see section 2.3.4) have also been carried out with a dense gold substrate or an EOS substrate covered with a thin layer of gold (see figure 2.10).

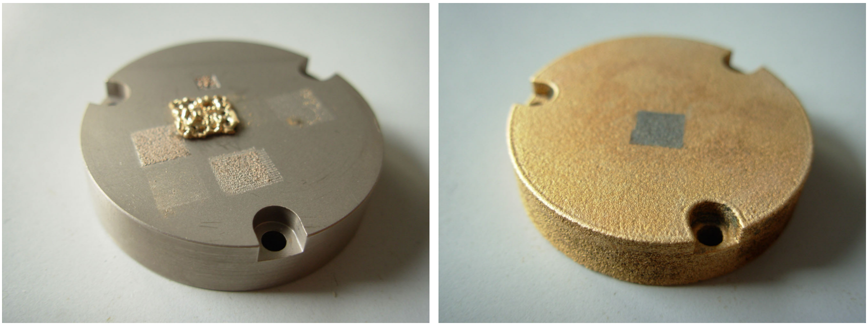

Figure 2.10: Dense gold substrate and gold covered EOS substrate

2.3 The powders

Many metallic materials have been used during this work. The most important are:

2.3.1 Titanium powder

The titanium powder (see figure 2.11(a)) is supplied by Alfa Aesar [19]. It is smaller than 150 mesh. The powder is 99.9% pure.

2.3.2 Tool Steel powder

The H13 tool steel powder (see figure 2.11(b)) is supplied by Sandvik Osprey [20]. It is strictly distributed between 8 μm and 13 μm.

2.3.3 Silver powder

The silver powder (see figure 2.11(c)) is supplied by Nippon Atomized Metal Powders Corporation [21]. It is water atomized and distributed around 10 μm. It is 99.9% pure.

2.3.4 18 carats Gold powder

The 18 carats gold powder (see figure 2.11(d)) is supplied by Hilderbrand [22]. Its composition is 75 %wt Gold, 12,5 %wt Silver and 12,5 %wt Copper. It is gas atomized and distributed around 10 μm.

2.3.5 WC-steel coated powder

The WC-steel coated powder (see figure 2.11(e)) is supplied by the University of Aveiro using a self developed method [23]. The Steel (304L) coating is a few nanometers thick.

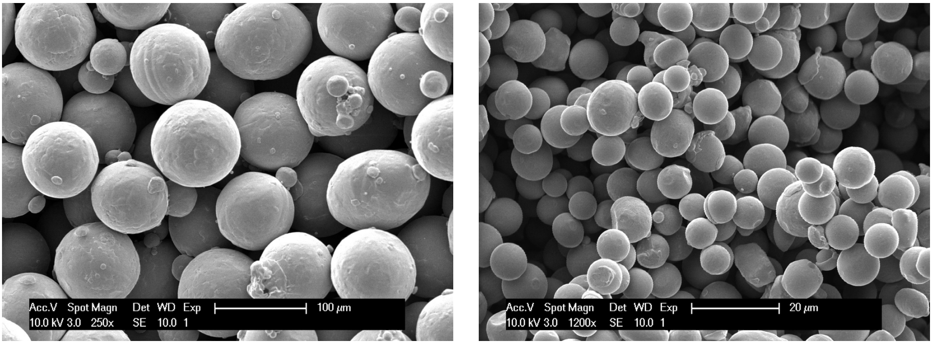

(a) Titanium powder

(b) H13 powder

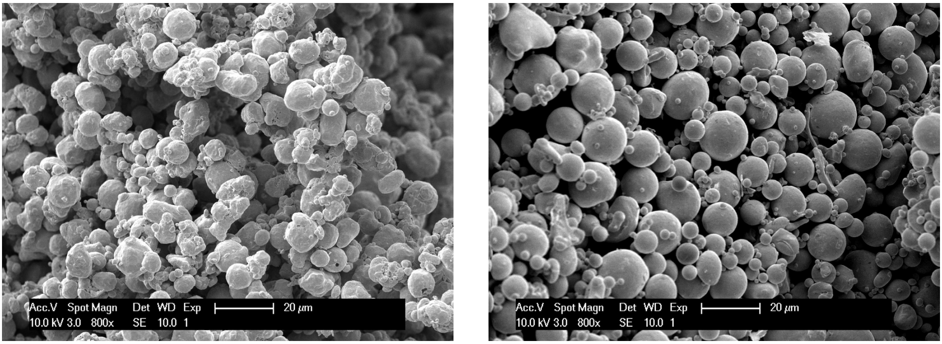

(c) Silver powder

(d) 18 carats gold powder

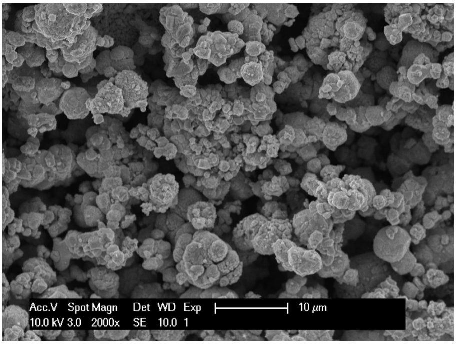

(e) WC-steel coated powder

Figure 2.11: The powders

2.4 The Delta3 robot

In Chapter 3 two single powder particles are isolated and precisely deposited into holes. For this purpose, a high precision robot, the Delta3 robot [24], is used.

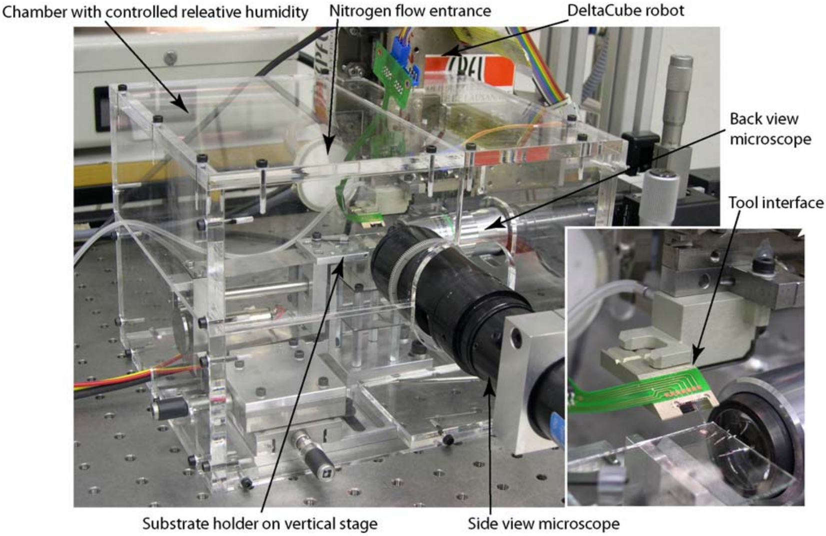

Figure 2.12: The Delta3 robot

It is based on parallel kinematics with three degrees of freedom and built with flexure hinges and non contact actuators and sensors allowing movements without friction. It presents a bandwidth of 400 Hz and stroke of 4 mm in all directions with a position repeatability of ±10 nm. This compact robot fits in a cube of 210 mm side.

Manipulation of beads was operated with a glass pipette (see figure 2.13) with a tip diameter of 5 to 15 μm. Picking operations are carried out using vacuum. But releasing such micro-parts is difficult because gravity becomes negligible compared to adhesive forces: by interrupting the vacuum, objects still remain on the glass tip. The vibration of the pipette is an efficient solution to release the objects once they are touching their final position. The vibration can be induced by a piezoelectric element (square signal of 2 kHz @ 0.3-0.6 V) at the settling point.

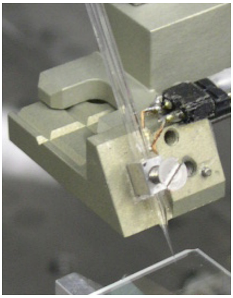

Figure 2.13: The pipette

2.5 Optical microscopy

Optical microscopy pictures were taken using an Olympus AX-70 microscope. The samples were enrobed with the SpeciFast resin from Buehler and polished with SiC paper up to 2400 mesh.

2.6 Scanning electron microscopy (SEM)

Scanning Electron Microscopy was prefered to optical microscopy to get pictures of the samples due to a bigger depth of field. It provided also informations about the crystalline orientations (EBSD). All analysis have been made on a SEM Philips XL-F30 at the Interdisciplinary Centre for Electron Microscopy (CIME) in EPFL.

2.6.1 Secondary electrons (SE)

Secondary electrons are produced when an incident electron excites an electron in the sample and loses some of its energy in the process. They come from the surface of the sample (a few $\dot{A}$) and their energy is less than 30 eV. Their number is highly dependant of the angle of incidence of the primary beam on the surface. So they provide topographic informations of the sample surface, similar to photography.

2.6.2 Backscattered electrons (BSE)

Backscattered electrons are primary electrons returning out of the sample after elastic collisions. The probability of the electrons to be backscattered depends on the atomic number of the sample material. A backscattered electron picture provides therefore a composition contrast.

Electron backscattered diffraction (EBSD)

If a material is crystalline, the backscattered electrons can be diffracted by the lattice, following Bragg's law [25]. To collect this information a diffraction camera must be mounted in the SEM.

It consists of a phosphor screen and a CCD camera to register the image on the screen. The sample has to be flat and polished. It is tilted ($\sim 70^\circ$ from horizontal) towards the diffraction camera.

Each crystallographic plane corresponds to two parallel lines on the screen, called Kikuchi lines, and the distance between these lines is related to the Bragg angle. A diffraction figure is drawn for each scanned point, consisting of Kikuchi lines intersecting. Then a software identifies automatically the crystallographic structure and the orientation of each zone.

Samples for EBSD have to be coated with a conductive resin (Konductomet from Buehler) and polished with diamond paste down to 0.25 microns. A chemical attack is necessary to remove the hardened layer at the surface of the sample. It consists of successive bufferings of

NaCN (10 g/100 ml water) and oxygenated water 30% (beginning and ending with NaCN) [26].

2.7 Density measurement

2.7.1 Archimedes weighing method

Density measurements of complex parts are usually achieved using Archimedes principle. A modified weight balance is used. Ours is a Mettler AG245 with a Mettler Archimedes kit (see figure 2.14).

Figure 2.14: The balance and Archimedes kit

One has to measure the weights of the piece in air w_a and in water w_w. The density is found using equation (2.1).

$$\rho = \frac{w_a}{w_a - w_w}(\rho_w - \rho_a) + \rho_a \tag{2.1}$$

with ρ_w the density of water (variable with temperature) and ρ_a the density of air.

But problems occur when dealing with porous pieces with open porosity. In this case, water penetrates into the pieces and w_w is bigger than it should be. The result is that the density is overestimated, sometimes reaching the bulk material density.

In order to solve this problem, we use the method described in [27] and used in [28]. The piece is impregnated with xylene which is a hydrophobic liquid. With this method three measurements are needed: one in air without xylene (w_a), one in water with xylene ($w_{xw)}$ and one in air with xylene (w_{xa}). The density is then calculated using equation (2.2)

$$\rho = \frac{w_a}{w_{xa} - w_{xw}} (\rho_w - \rho_a) + \rho_a \tag{2.2}$$

under the assumption that the xylene exactly fills all the pores.

2.7.2 2D image analysis

Another method used to determine the density of the pieces is image analysis after enrobing and polishing (see section 2.5). In this case a 2D density is actually obtained. Images with a black and white contrast are analyzed with a Labview program: Imaq vision builder. A threshold has to be chosen manually and the proportion of solid to pore is then calculated by the program. The choice of the threshold is a crucial point, because it is highly dependant on subjective appreciations. Note also that this 2D density analysis is only an assessment of the pieces real density. A statistical analysis on different layers and on profile cuts would be needed to approach the global 3D density.

Chapter 3

Study of the interparticular necks in SLS

The SLS process is limited by two antagonist processes. If too much energy is given, all the material melts and part precision is lost. On the other hand, if the particles do not receive enough energy, the bonding between the particles is weak and the parts have poor mechanical properties. The understanding of the molten phase evolution and of its influence on the inter-particular necks evolution is essential to play between these two limitations.

In the SLS process, pulsed lasers are mostly used. Since only the surface of the powder particles is molten, consolidation can be achieved at much lower average power. Liquid bridges appear between the powder particles and are responsible for the bonding. The mechanical properties of the final part depend on the shape of these bonds. The goal of this study is to understand how the evolution of the liquid bridges (also called necks) is influenced by the laser parameters.

Our idea is to collect enough experimental information concerning the sintered state of a few particles under different laser conditions. Comparing these results with the the liquid phase evolution (predicted by the thermal model) we hope to get a better understanding of the binding mechanisms involved in SLS.

This work is divided into two parts. The first one is an experimental study. We analyze the geometrical features of a few particles after different types of laser treatment corresponding to different values of the power, repetition rate and pulse duration. These results are obtained thanks to the development of an adequate system for the separation and the transport of the two particles. A Π-shaper (see section 2.1.1) is also mounted on the laser, so that the gaussian shape of the beam becomes a top-hat profile. The evolution of the inter-particular neck is then obtained by image processing on electron micrographs.

The experimental results are used to clarify the exact relationships between the melting kinetics and the bounding mechanisms. They should be a keystone in developing a comprehensive model of the SLS process taking the thermal phenomena and the flow of molten material into account.

In the second part of this work we present a thermal model of the interaction between the laser beam and a single (metallic) grain. This model demonstrates the deep influence of the laser parameters, like power, pulse duration and repetition rate, onto the melting kinetics and the liquid phase behavior. The experimental results are compared to the thermal model output.

3.1 State of the art

3.1.1 Consolidation process

The global consolidation process is essentially driven by the minimization of the total surface energy [29]. Under laser heating, the material wants to group in a sphere. When too much energy is given, giants balls tend to form inside the part (balling effect) [30] [31].

The kinetics of the material reorganization is slowed down by viscous effects and material re-solidification. Because of these two phenomena, the control of the quantity of molten material and of its lifetime is essential to ensure a strong microscopic bounding and a good macroscopic precision of any part made by SLS [32]. The quantity of liquid and the time it takes to get back to solid state can be influenced by the laser parameters. It can be shown that metallic particles essentially undergo superficial melting under short laser pulses [33].

3.1.2 Thermal model

There are several thermal models describing the laser-matter interactions [32], [14]. They are usually based on unrealistic assumptions about the latent heat of fusion which is often neglected and about the thermal exchange between the grain and the exterior (insulated (or single) grain model). These assumptions all result in considerable simplifications of the numerical model.

3.2 Experimental setup

The material we investigate is pure Titanium. We use a powder with radii distributed between 45 and 50 μm (see section 2.3.1). Two methods are used.

3.2.1 Method A: Isolation of two particles

Two particles of powder are deposited on copper substrates. Copper has been chosen because of its high thermal conductivity. In this way, the observation should not be modified by an unwanted melting of the substrates. A network of holes is created on the substrate to avoid the particles to be blown away over long distances when they are hit by the laser. Each hole has a depth and a diameter of 300 μm.

The Delta3 robot described in section 2.4 is used to isolate two Titanium particles. They are deposited into the holes of the substrate and irradiated by the laser under inert gas (argon).

A given amount of energy is brought to the particles by the laser in multimode (see section 2.1.1) and a SEM micrograph is taken afterwards. The cycle is then repeated: a) irradiation of the particles, b) micrograph analysis.

In this way we obtain pictures of the bonding of two particles and we can observe precisely the neck formation.

3.2.2 Method B: Observation of particles on a powder bed

A Π-shaper is mounted in the laser (see section 2.3). This optical element transforms the laser gaussian beam in a top-hat profile (see Appendix C). In this way, we know the exact energy delivered to the particles.

Powder beds of Titanium are made and irradiated with different scanning speeds of the laser. Knowing the spot radius of the laser ($\omega = 0.1\,\mathrm{mm}$), the exact time of illumination is known. In the case of continuous mode, a preheating of the powder has to be taken into account (see section 3.3.1). For each speed, a SEM micrograph is taken. Then the cycle a) irradiation of the particles, b) micrograph analysis is repeated.

This manipulation is appropriate to quantitative measurements, while the previous one (section 3.2.1) essentially leads to qualitative observations of the bonding phenomena.

3.2.3 Measurements on micrographs

We obtain different fixed stages of the consolidation process. Electron micrographs are suitable because of their large depth of field.

To compute the energy given to the particles, we measure precisely the power of the laser and the irradiation time at each step.

The electron micrographs are analyzed with a Labview program: Imaq vision builder. It measures the quantities listed in table 3.1:

measured quantities	symbol
particles radii	r_1, r_2
neck diameter	a
particles centers displacement	b

Table 3.1: Direct measurements from Imaq vision builder.

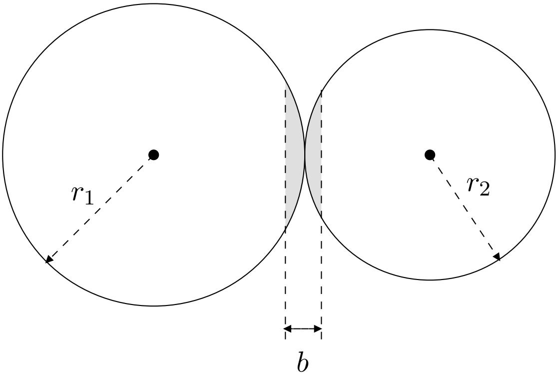

Figure 3.1: 2D representation of the pair of particles.

From this data, indirect values describing the sintering process can be computed by simple geometry (see table 3.2).

characteristic	symbol
lateral surface of the system	s
neck volume	V
sintering rate	S

Table 3.2: Geometrical characteristics of a sintered system

The volume of liquid contributing to the neck is assumed to be the volume of two spherical caps of height $\mathrm{b\,r_1/(r_1{+}r_2)}$ and $\mathrm{b\,r_2/(r_1{+}r_2)}$ for the particles of radius $\mathrm{r_1}$ and $\mathrm{r_2}$ respectively (see figure 3.1).

The lateral surface s of the system is the surface of the two particles minus the indented surface. The sintering rate S characterizes the surface minimization. It is the ratio $100\,(s_0 - s)/(s_0 - s_{min})$ where s_{min} is the surface of one single sphere and s_0 the surface of two separate spheres with the same volume of material (see figure 3.2). A similar parameter has been defined in [30]. The difference is that they relate it to the radii of the particles while we relate it to the surface of the system.

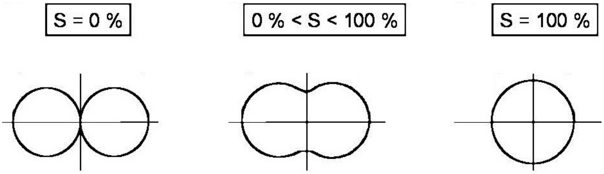

Figure 3.2: Sintering rate (image modified from [30])

3.3 Numerical model and simulations

We propose a thermal model to describe the interaction between a laser beam and a (spherical) grain. This model allows for a non-vanishing latent heat of fusion and for a realistic surrounding. The absorbed laser intensity is modeled by means of the Mie theory [34]. It expresses the absorbed intensity as a function of the spherical coordinates r, ϑ and φ with respect to the center of the grain.

Our model demonstrates how the laser parameters influence the molten material behavior. The examples presented below are the simulations of a Titanium grain. The grain radius r is $50\,\mu$m and the physical properties of bulk Titanium are summarized in table 3.3.

density ρ	$4.5{\times}10^{-3}$ [g/mm^3]
specific heat c_p	0.528 [J/g^{o}C]
thermal conductivity k	$17.0{\times}10^{-3}$ [W/mm^{o}C]
dielectric constant[1] $\varepsilon_R + i\varepsilon_I$	0.3375-22.78i [$-$]
melting temperature T_m	1660 [^{o}C]
latent heat of fusion L	435.4 [J/g]

Table 3.3: Physical properties of bulk Titanium

The laser is a Nd:YAG operating at a power of $4.5\,W$ (power used in the following experiments). It is used either in continuous mode or

---

[1] for the Nd:YAG fundamental radiation.

in pulsed mode (pulse duration: 200 ns).

Two important entries of this model are the absorption coefficient α of the laser into the grain (ratio between the absorbed and the irradiated power) and the heat exchange coefficient κ with the exterior. Since the grain is surrounded by air and other grains in random positions, these entries are difficult to calculate theoretically. The following remarks can be made about α and κ:

- The absorption coefficient α of the laser into a single $50\,\mu$m radius Titanium particle with no electromagnetic interaction with the exterior is 0.48 according to the Mie Theory [34]. In the case of a grain reposing in a powder bed, this coefficient should be higher due to multiple reflections on the other grains.

- In our model the exterior is considered as a heat sink of fixed temperature. The heat exchange between the grain and the exterior is proportional to the difference $T - T_0$ where T is the grain surface temperature and T_0 the sink temperature. The proportionality constant is denoted by κ and called heat exchange coefficient.

Arising from these remarks, a new method to easily determine α and κ is developed. It is presented in the following section.

3.3.1 Determination of α and κ (continuous mode)

In the case of a continuous laser, one can assume homogeneous heating of the $50\,\mu$m radius Titanium particle. The Biot number, $Bi{=}\kappa\,\mathrm{r}/3k$, determines whether or not the temperatures inside a body under a stationary heat source varies significantly in space. For our particle, $Bi \ll 1$ which means that the homogeneous heating hypothesis can be made. In this case, the uniform grain temperature converges exponentially towards an asymptotic value T_∞ with a time constant t_c.

$$T(t) = T_\infty + (T_0 - T_\infty)e^{-\frac{t}{t_c}} \tag{3.1}$$

The equilibrium temperature depends on α and κ and also on the laser parameters (power P and spot radius ω):

$$T_\infty = T_0 + \frac{\alpha P}{4\kappa\pi\omega^2} \tag{3.2}$$

This relation is another way of writing the balance equation $4\pi \mathrm{r}^2\kappa(T_\infty - T_0) = \alpha\pi \mathrm{r}^2 \mathrm{I}_0$ where $\mathrm{I}_0 = \mathrm{P}/\pi\omega^2$.

The time constant is related to κ and to the physical properties of the grain:

$$t_c = \frac{\rho C_p r}{3\kappa}. \tag{3.3}$$

To determine the value of α and κ, two experiments with different powers P_1 and P_2 are made. We denote t_1^* and t_2^* the critical times when the melting temperature T_m is reached. Using (3.1), (3.2) and (3.3) we get a system of two equations for the two unknowns α and κ:

$$\begin{cases} T_m - T_0 = \dfrac{\alpha P_1}{4\kappa\pi\omega^2}(1 - e^{-\frac{3\kappa\, t_1^*}{\rho C_p r}}) \\ \\ T_m - T_0 = \dfrac{\alpha P_2}{4\kappa\pi\omega^2}(1 - e^{-\frac{3\kappa\, t_2^*}{\rho C_p r}}) \end{cases} \tag{3.4}$$

The numerical values we use for P_1 and P_2 are 5.8 W and 4.2 W respectively. The laser spot is $\omega = 0.1\,\mathrm{mm}$. The transition between the situation where no particles are fused and the situation where a lot of molten material appears turns to be quite sharp. In our case, we get $t_1^* \simeq 30\,\mathrm{ms}$ and $t_2^* \simeq 60\,\mathrm{ms}$ respectively. These experiments are done using Method B (see section 3.2.2). The related pictures are shown in Appendix B. Since the laser is drawing lines, a preheating of the powder has to be taken into account, and a temperature T_0=500° is used. The absorption coefficient α and the heat transfer coefficient κ are found by solving (3.4) ([35]):

$$\alpha = 60\,\% \qquad \kappa = 0.013\,\mathrm{W/mm^2K} \tag{3.5}$$

3.3.2 Grain simulations in pulsed mode

In the case of pulsed laser, one can no longer assume homogeneous heating of the grain, since the heat source is not constant in time. Numerical simulations have to be used instead of equations (3.1) to (3.4). However, we consider that the coefficients α and κ found in equation (3.5) are valid.

In our model, the heat source is divided in two parts, in order to have the 60 % absorption predicted by the experiments (see equation (3.5).

The space and time depending heat source (48 %) describing the effect of the laser on a single particle is computed by solving the Maxwell equations [34]. The resulting 12 % are distributed homogeneously on the surface to account for the multiple reflections.

For the first part of the heat source (48 %), the dielectric constant of the media (see table 3.3) has to be used as an input. The direct output of the Maxwell equations is the electrical field distribution $\mathbf{E}$ inside the particles. The heat source q is calculated:

$$q = -\frac{1}{2}\varepsilon_0 \varepsilon_I \Omega \|\mathbf{E}\|^2 \tag{3.6}$$

where ε_0 is the permittivity of free space (8.85×10^{-12} F/m) and Ω the angular pulsation of the radiation (1.77×10^{15} Hz for the Nd:YAG fundamental mode)[2].

Since particles are assumed to be spherical, the generalized coordinates (r, θ, ϕ) are well adapted. The heat source has a special dependency with respect to the polar angle ϕ and the 3D thermal problem can be reduced by a standard truncated Fourier analysis. In this way we are left with a finite number (one for each Fourier mode) of coupled and non-linear 2D heat equations in the (r, θ) plane[3]. They can be

---

[2] $\Omega = 2\pi\, c/\lambda$ where c is the speed of light and λ the corresponding wavelength

[3] The coupling of the 2D heat equations in the (r, θ) plane is due to the non-vanishing latent heat

solved by the Chernoff scheme [36] with adequate time steps and mesh sizes.

Figures 3.3(b) and 3.3(c) represent the time evolution of the ratio between the volume of the molten material and the volume of the grain for different repetition rates with α and κ as in equation (3.5). The heat sink temperature T_0 is set to 0° since the powder has time to cool down between each pulse.

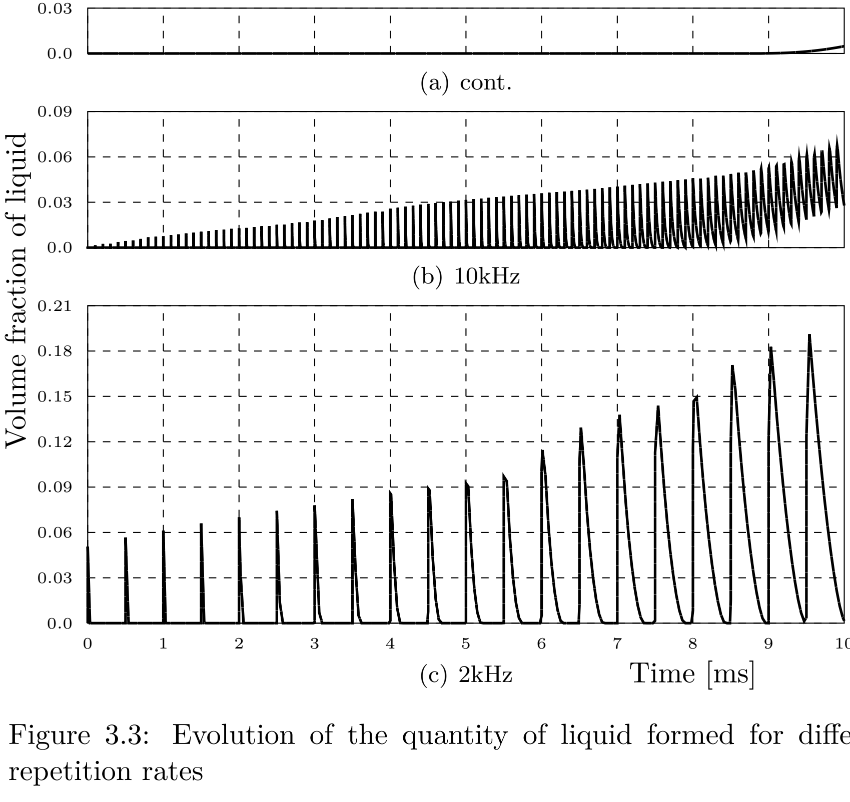

Figure 3.3: Evolution of the quantity of liquid formed for different repetition rates

For these two simulations the laser power is $4.5\,W$. With the same power the whole particle stays nearly solid in continuous mode (see figure 3.3(a)). But in pulsed mode we get liquid almost immediately. The grain is partially fused but has time to cool down completely between pulses. At 2 kHz repetition rate, the volume of liquid reaches 18 percent of the total particle volume at each pulse. This behaviour is not favorable to good sintering. With a big amount of liquid formed at the same time, balling can occur. Consequently, a repetition rate of 10 kHz or more seems suitable to get good bondings between the particles. In the following experiments the selected repetition rates will be in the range 10-50 kHz.

3.4 Results

We studied three different pairs of particles, each at a different repetition rates (10, 20 and 50Hz). Each of them has been irradiated two times with increasing laser power. The behaviors we can observe are illustrated by the pictures of figure 3.4. These pictures have been obtained by using method A (see section 3.2.1).

This method essentially gives qualitative informations but since the beam is multimodal, the laser energy absorbed by the particles is not easy to compute. Quantitative informations can only be derived by applying method B (see section 3.2.2).

The measurements presented on table 3.4 are made using method B and directly obtained from the Imaq vision builder. In all cases, the irradiation time is 10 ms, the laser power is 4.5 W and the associated pulse duration is 200 ns. The beam radius of the laser is 100 μm and the total energy, E, irradiated on the particles is calculated for each step with an uniformly distributed intensity due to the Π-shaper.

The measurements obtained directly from the Imaq vision builder are summarized in table 3.4.

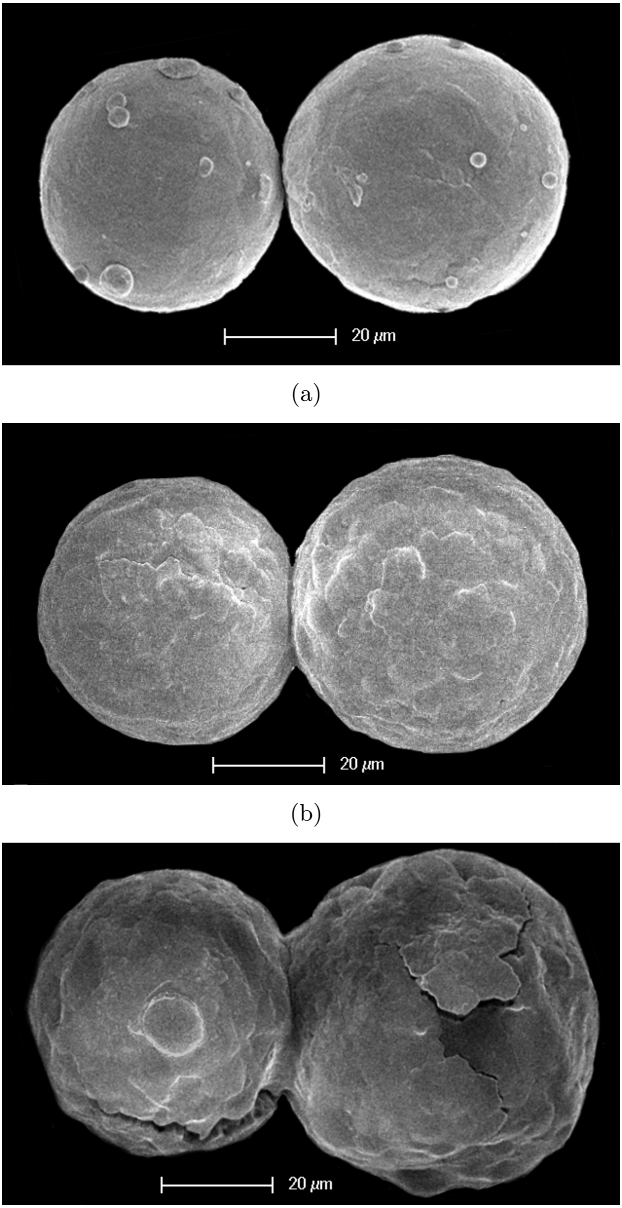

(a)

(b)

(c)

Figure 3.4: Particles before (a) and after (b) (c) irradiation

	E $[mJ]$	r_1 $[\mu m]$	r_2 $[\mu m]$	a $[\mu m]$	b $[\mu m]$
10 kHz	0	45	49	0	0
	20	45	50	56	23
	40	45	50	76	28
20 kHz	0	40	48	0	0
	18	40	48	57	3
	36	40	47	58	5
50 kHz	0	41	42	0	0
	16	41	42	60	1
	32	41	41	62	4

Table 3.4: Data directly deduced from Imaq vision builder

We get the lateral surface of the system s, the neck volume V and the sintering rate S (see table 3.2) by processing the data of table 3.4. The results of these computations are summarized in table 3.5:

	$E[mJ]$	$s[\mu m^2]$	$V[\mu m^3]$	$S[\%]$
10 kHz	0	55321.0	0.0	0.0
	20	49998.0	36586.0	47
	40	48506.0	53188.0	61
20 kHz	0	49015.0	0.0	0.0
	19	48230.0	630.0	8
	38	46499.0	1708.0	26
50 kHz	0	43187.0	0.0	0.0
	16	43030.0	65.0	2
	32	41727.0	1014.0	22

Table 3.5: Processed data.

As expected, the lateral surface decreases and the volume of the neck increases from one step to the other. This phenomenon is even more marked for the 10 kHz repetition rate, because the quantity of involved liquid is bigger.

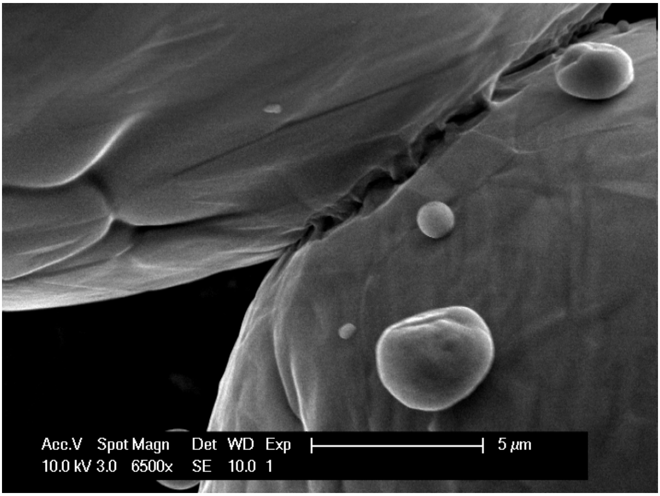

(a) neck after first irradiation

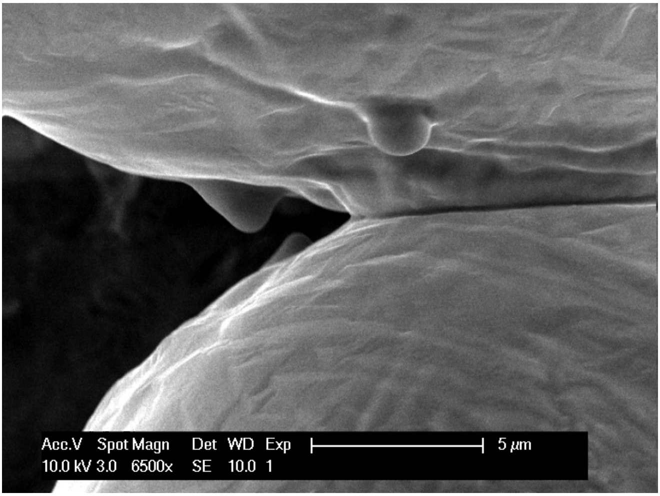

(b) neck after second irradiation

Figure 3.5: Necking phenomena

More precise observations (method A) of the sintering process between the two grains show that the first stage of the inter-particular necks was not homogeneous. Many little bridges are formed and hold the particles together (figure 3.5 a). Then the entire neck forms and grows as expected (figure 3.5 b).

After irradiation, we observed, as pointed out in [37], the formation of droplets on the surface of the particles which means that a part of liquid formed cannot contribute to the interparticular neck.

We also remarked that the particles often separate after laser irradiation. This could be the effect of the pressure brought by the laser itself. Another explanation is that the wetting between the two grains is not always ideal. As pointed out in [38], the formation of a thin layer of liquid on the particle surface can be energetically preferable in certain cases. In particular, when the powder is not spherical, the energy given by the laser is used to minimize the surface energy of each particle by making spheres. The result is that they repulse each other.

The following experiment emphasizes this effect. A non-spherical powder is used. On figure 3.6(a) two particles of powder are illuminated by the laser. The effect is shown on figure 3.6(b).

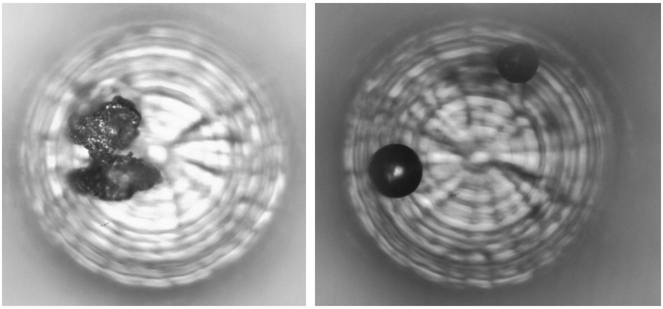

(a) (b)

Figure 3.6: Repulsion of non spherical powder grains

3.5 Comparison between simulation and experiments

For the 10 kHz frequency, the simulations (see figure 3.3(b)) predict that 6 % of the grain is molten after 10 ms irradiation. In the related experiment, the neck volume is found to be 4 % of the entire material for the first laser illumination, and 6 % for the second. The simulations are in agreement with the experiments and good predictions about the final stage of the bonding of the particles for different laser parameters are provided by the thermal model.

To predict exactly the amount of liquid contributing to the neck a flow model describing the motions of the molten material would be needed [38]. Capillary driven flow models unfortunately lead to complex free surface problems [39] and simplifying hypotheses need to be made. This is the subject of the Chapter 4.

3.6 Conclusion

This chapter leads to a better understanding of the necking phenomena involved in the SLS consolidation process. We have developed an experimental set-up to observe and quantify the final state of a small amount of laser sintered grains. This process has been shown to be replicable and trustful. To interpret the experimental data we get, we simulate the time evolution of liquid by using a thermal model of the laser-matter interaction. A new method to find easily the absorption coefficient α of the laser into the grain and the heat exchange coefficient κ with the exterior is developed. The thermal model leads to good predictions of the particle final sintering state.

The main issue is then to explain the capillary flow mechanisms leading from the molten material to the neck formation. This analysis should ideally result in a comprehensive SLS model combining the thermal description and an adequate (and possibly not too complex) fluid flow model (see Chapter 4).

Chapter 4

An approach to a fluid flow model

4.1 Capillary rise: state of the art

The liquid motion between two solid particles in selective laser sintering can be compared to a capillary flow, in a cylindrical capillary or between two parallel plates.

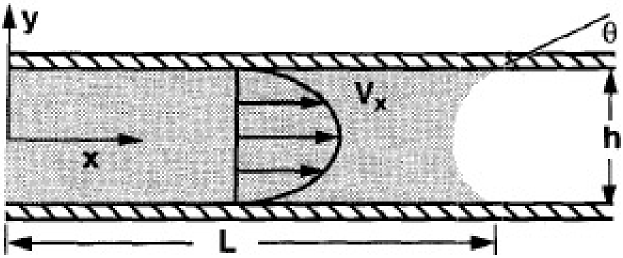

Figure 4.1: Capillary flow (from [40])

The advantage of dealing with capillary flows is that they are incompressible and laminar viscous. The classical analysis [41] is to treat the motion of the incompressible fluid within the assumption of Poiseuille flow. The complexity of the flow pattern in the vicinity of the meniscus is neglected. Laminar flows in a pipe are characterized by a parabolic velocity profile with zero velocity at the walls (the no-slip condition).

This is also true for a capillary flow: far from the meniscus, there exists no radial component of the velocity vector, since the walls are non-penetrable. However, it is clear that a convex velocity profile can not produce a concave meniscus at the end of the capillary. There must be a lateral flow in the head zone [42]. This situation is depicted in figure 4.2. The departure from Poiseuille flow in the vicinity of the advancing meniscus is studied in [43] where the Washburn equation is modified to account for the flow near the meniscus. But since the length of the affected zone does not exceed a few times the radius of the pipe, these effects can safely be neglected for fine capillaries [42].

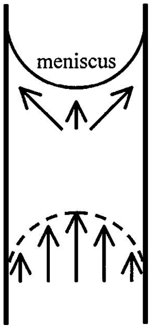

Figure 4.2: Departure from Poiseuille flow (from [42])

Gravity is in general neglected when dealing with narrow capillaries with a small characteristic length h (tube radius or distance between plates). This can be justified by computing the Bond number Bo measuring the importance of gravity compared to surface tension forces. The formula for the Bond number is $Bo = \rho g h^2/\gamma_{LG} \ll 1$ where ρ is the liquid density, g the acceleration due to gravity and γ_{LG} the surface tension of the liquid-gas interface. In all the cases we will consider, $Bo \ll 1$ [44].

4.1.1 Background

The understanding of liquid rise in capillaries is important in many fields going from film flows in coating devices and dynamics of drops in ink-jet printing to biological and biomedical applications of fluid mechanics, bioengineering and microfluidics. During the last two centuries the complexity of the involved phenomenas have led to extensive studies [45] [46].

The attempts to describe mathematically capillary flows by combining well-known elements from classical fluid mechanics lead in some cases to solutions with unphysical properties. As we shall see in section 4.1.3 and 4.1.4 the main difficulty is that dynamic wetting operates on a scale that extends from the macroscopic to the molecular, while the observations usually involve only macroscopic quantities such as wetting speed, viscosity, surface tension and contact angle.

The main parameters used to quantify the dynamics of wetting are the relative velocity at which the liquid moves across the solid: the wetting-line velocity U, and the angle formed between the moving liquid interface and the solid surface at the line of three-phase contact: the dynamic contact angle θ_D (also called apparent contact angle). The dynamic contact angle is the key boundary condition. The experimentally observed dynamic angle generally differs significantly from its equilibrium value θ_E and may refer to either an advancing (wetting) or a receding (dewetting) interface. This point will be discussed later in section 4.1.3 and 4.1.4.

4.1.2 The dynamic contact angle

In a solid-liquid-gas system, the equilibrium angle θ_E has been introduced into macroscopic fluid mechanics by Young (1905) through the well-known Young's equation:

$$\gamma_{SL} + \gamma_{LG} \cos\theta_E = \gamma_{SG} \tag{4.1}$$

where γ_{SL}, γ_{LG} and γ_{SG} are respectively the surface tension of the solid-liquid, liquid-gas and solid-gas interfaces

Since that time, experimental observations have led researchers to the view that, when a contact line is moving, the angle deviates from its equilibrium value. This dynamic contact angle θ_D is bigger than θ_E if the liquid is moving forward and smaller if it is receding.

The force balance equation is then:

$$\gamma_{SL} + \gamma_{LG} \cos \theta_D = \gamma_{SG} + F \tag{4.2}$$

where F is the resulting force acting on the fluid. Substituting equation (4.1) in equation (4.2) we have:

$$F = \gamma_{LG} \cos(\theta_D) - \gamma_{LG} \cos(\theta_E) = \gamma_{LG}(\cos \theta_D - \cos \theta_E) \tag{4.3}$$

4.1.3 Hydrodynamic theory

This classical approach holds on dissipation due to viscous flow near the moving contact line. In that case, one can see three relevant length scales (see figure 4.3): macroscopic (scale of observation), microscopic (scale of the atoms) and mesoscopic (between them).

The basic idea of this theory is the following: changes in the experimentally observed dynamic contact angle θ_D in the macroscopic region are attributed to viscous bending of the liquid-gas interface in the mesoscopic region.

There is also a microscopic angle θ_m, which is usually assumed to be governed by short-range intermolecular forces and to have a static value.

The hydrodynamic theory does not result in a physically acceptable solution. Because of the conflict between a contact line that moves and the conventional no-slip boundary condition between a liquid and a solid, stresses are unbounded at the wetting line, and the force exerted by the liquid on the solid becomes infinite [47]. This can be easily understood by the following reasoning [46]. There is a no-slip condition on the solid surface which allows the solid substrate to remove the

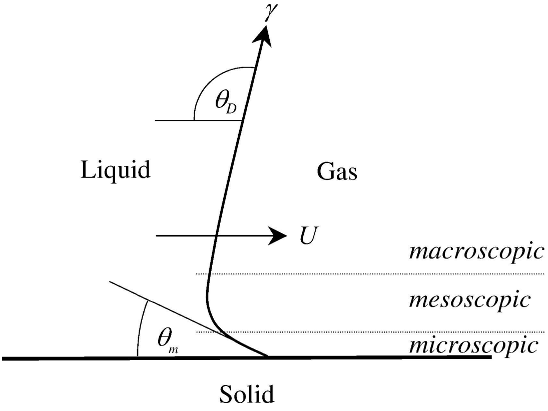

Figure 4.3: Relevant scales in hydrodynamic theory (from [45])

liquid from the vicinity of the contact line, reducing pressure here. The capillary pressure tries to compensate the difference between a constant pressure in the gas and the reduced pressure in the liquid by bending the free surface towards the gas (see figure 4.3). The no-slip condition is so efficient in removing the liquid and reducing the pressure that the capillary pressure has to bend the surface so strongly that the latter cannot meet the solid surface to form a contact angle.

One approach to dealing with this singularity has been to truncate the solution artificially at the molecular scale where the continuum description breaks down. For example, Voinov [48] assumes that the curvature of the fluid near the end of the angle is relatively insignificant and corresponds to the fact that the free surface is nearly straight. He then uses the work of Moffat [49] to take a creeping fluid motion inside a corner into account. He was the first to derive the formula describing the apparent contact angle:

$$\chi(\theta_D) - \chi(\theta_m) = Ca \ln(\frac{L}{L_m}) \tag{4.4}$$

where the function $\chi(\theta) = 1/2 \int_0^{\theta} [\hat{\theta}/sin\hat{\theta} - cos\hat{\theta}] d\hat{\theta}$.
For $\theta_D < 3\pi/4$, the integrand may be approximated by $2\hat{\theta}^2/3$; hence 4.4 becomes:

$$\theta_D^3 - \theta_m^3 = 9\, Ca \ln(\frac{L}{L_m}), \quad \theta_D < 3\pi/4 \tag{4.5}$$

where Ca holds for Capillary number ($Ca = \mu U/\gamma_{LG}$ with μ the viscosity and U the speed of the contact line) and L, L_m are appropriately chosen macroscopic and microscopic length scales, respectively.

Alternatively, the flow equations and boundary conditions have been modified by relaxing the no-slip condition in the vicinity of the contact line [47] [50] [51] [52]. In this case, the force exerted on the solid is finite, though the stresses in the liquid remain unbounded. In both cases, the capillary number is presumed small, so that far from the wetting line the liquid-gas interface takes its static shape. It is only on the mesoscale that viscous bending becomes important. The macroscopic dynamic contact θ_D angle is then determined by extrapolating the static interface to the solid surface.

This reasoning also leads to the derivation of equation (4.4).

In a lot of works, the preference is given to the parent equation [53] [54] [55]:

$$Ca = \frac{\mu U}{\gamma_{LG}} = \kappa(\theta_D^3 - \theta_E^3) \tag{4.6}$$

where κ is 0.013 for most materials.

4.1.4 Molecular-kinetic theory

At a nanoscopic point of view, the fluid can no longer be consider as continuous, and one has to turn to molecular kinetics in order to understand the dynamic of the moving line.

This approach focuses on the dissipation occurring in the immediate vicinity of the moving contact line due to the process of attachment or detachment of fluid particles (see figure 4.4). In this case, only two length scales are relevant: the molecular scale, where the dissipation occurs, and the macroscopic scale where its effects are seen. The key parameters are κ^0, the equilibrium frequency of the random molecular displacements, and λ, the average distance of each displacement.

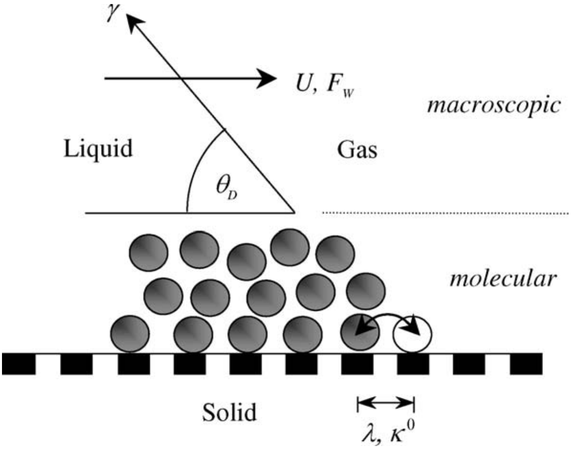

Figure 4.4: Relevant scales in molecular-kinetic theory (from [45])

Molecular dynamics simulations have been made in [56]. They proved that the contact angle measured on the molecular length scale deviates from the static one when the contact line is moving, as observed from a continuous point of view. In [57], the authors found that the usual no-slip boundary condition is not valid at a smaller distance than ~ 2 atomic spacings from the contact line, but is satisfied at larger distance.

4.1.5 The Shikmurzaev model

A more radical approach for modelling the moving wetting line and the dynamic contact angle is proposed by Shikhmurzaev [58][59][39]

. He takes into account dissipation through standard hydrodynamic channels, but also uses non-equilibrium thermodynamics to describe dissipation due to the interfacial creation and destruction processes occurring as the contact line moves across the solid surface. The microscopic dynamic contact angle is coupled directly to the flow and is not an independent quantity. Analytical expressions can be obtained for certain simplifying conditions (including low capillary and Reynolds numbers) which successfully describe experimental results found in the literature. A key element of the model is the fact that as a liquid advances across a solid surface, liquid at the liquid-gas interface becomes transferred to the solid-liquid interface, so there is a material flux from one interface to the other through the contact line.

4.2 Modeling

In this section we present two different models developed during this work to simulate the spreading of a cylinder of liquid between two parallel plates. The first one simulates a capillary flow between the plates, and will be called *Washburn model* in the following sections. The second one deals with energetic considerations arising from Frenkel's principle, and it will be named *Frenkel model.* In both cases, the final output is the liquid lifetime necessary to get the interparticular neck lengths a observed in section 3.4.

4.2.1 Washburn model

As we are interested in macroscopic phenomena, we will only use the hydrodynamic theory to develop this model.

On figure 4.5(a) we see the particles before laser illumination. We assume that the liquid contributing to the neck is formed in the vicinity of the contact between the particles and that its volume V is the volume of two spherical caps:

$$V = \frac{\pi}{3}(\frac{h_0 r_1}{r_1 + r_2})^2(3r_1 - \frac{h_0 r_1}{r_1 + r_2}) + \frac{\pi}{3}(\frac{h_0 r_2}{r_1 + r_2})^2(3r_2 - \frac{h_0 r_2}{r_1 + r_2}). \quad (4.7)$$

The liquid is then modeled as a cylinder of height h_0 and radius R_0 (see figure 4.5(b)) between two parallel plates. Its volume is

$$V = \pi h_0 R_0^2. \quad (4.8)$$

This modeling is only valid if $h_0 \ll r_1, r_2$, otherwise the regrouping of the fluid in a central cylinder would be too artificial.

The liquid tries to minimize the interface with the atmosphere by flowing between the plates. In order to keep the volume constant the particles have to get closer. At the end of the flow, the cylinder has a height h_f and a radius R_f (see figure 4.5(c)).

We relate the quantities h and R to the measured values a and b of Chapter 3 (see table 3.1) in the following way:

- h_0 is set equal to the particles center displacement b.
- R_0 is found by volume conservation using equations (4.7) and (4.8).
- R_f corresponds to half the final neck diameter $a/2$.
- h_f is found by volume conservation ($V = \pi h_f R_f^2$).

Actually the particles centers displacement is equal to $h_0 - h_f$ (see figure 4.5(a) and 4.5(c)). But in general $h_f \ll h_0$ and the initial condition $h_0 \simeq b$ is justified.

We consider a fluid of density ρ and viscosity μ. The surface tension of the liquid-gas interface is denoted by γ_{LG} and the dynamic angle by $\theta_D(t)$ (cf. figure A.1). The equation to solve in order to find the evolution of the liquid cylinder radius $R(t)$ and of its speed $\dot{R}(t)$ is:

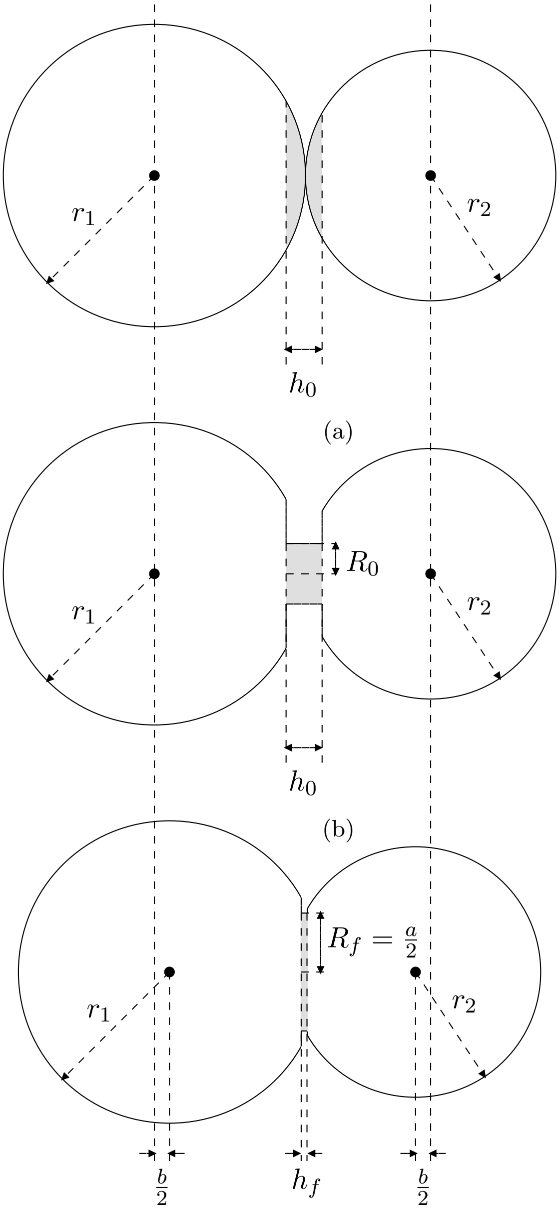

(a)

(b)

(c)

Figure 4.5: Modeling of the bonding phenomena (Washburn model)

$$\rho(R(t)\ddot{R}(t) + 2\dot{R}^2(t)) = \frac{4\gamma_{LG}}{h(t)}\cos\theta_E - \frac{12\mu}{h(t)^2}R(t)\dot{R}(t). \tag{4.9}$$

For the complete development of this formula see Appendix A. Similar equations for a cylindrical capillary can be found in [42] and [60].

Flows in capillaries with varying diameter are calculated in [61]. The resulting equations could be translated for our case but are heavy and not essential. We relate the length $h(t)$ to $R(t)$ by volume conservation, which leads to:

$$h(t) = \frac{h_0 R_0^2}{R(t)^2} \tag{4.10}$$

$$\rho(R(t)\ddot{R}(t) + 2\dot{R}^2(t)) = \frac{4\gamma_{LG}R(t)^2}{h_0 R_0^2}\cos\theta_E - \frac{12\mu}{h_0^2 R_0^4}R(t)^5\dot{R}(t). \tag{4.11}$$

Values of γ_{LG} and μ

The values γ_{LG} and μ do vary with temperature. To evaluate the isothermal or non-isothermal behaviour of our system of dimension l, we compute the Fourier number $Fo = k\,t/C_p\rho\,l^2$, where k is the thermal conductivity, C_p the specific heat and ρ the density. This number is the ratio of the liquid lifetime with the time necessary to reach thermal equilibrium in the sample by conduction. This change should be accounted for through the temperature sensitive parameters γ_{LG} and μ [38]. If Fo is large ($\gg 1$) the system will reach equilibrium within the considered time frame and has to be treated as non-isothermal. If it is small ($\ll 1$) the system will react in an isothermal way.

For all the times predicted by the models (see section 4.3), the Fourier number is smaller than 1. It means that the temperature of the system has no time to change during the time of the rearrangement process. This criterion leads to the use of a constant temperature value and steady values of $\gamma_{LG}(T)$ and $\mu(T)$ can be used.

The chosen value of the surface tension γ_{LG} of liquid titanium is 1.650+T_{max}(-0.00026) J/m^2 [62] where T_{max} is the maximum value predicted by the simulations of section 3.3.2. For the liquid titanium viscosity, we use $T_{max} = T_m$ because the variation of viscosity with temperature is negligible. We get [62]:

$$\gamma_{LG} = 1.650 + T_{max}(-0.00026)\,\mathrm{J/m^2} \qquad \mu = 0.0052\,\mathrm{Ns/m^2}. \quad (4.12)$$

4.2.2 Frenkel model

The liquid between the particles is modeled as a cylindrical column of fluid with axis z, height $2h_0$ and radius R_0 (see figure 4.6). The fluid is incompressible and has a density ρ, a viscosity μ and a surface tension γ_{LG} with the air. The extremities ($z = -h_0$) and ($z = +h_0$) are in contact with two solid plates. There is no surface tension between the plates and the liquid ($\gamma_{SL} = 0$) because they are assumed to be the same material.

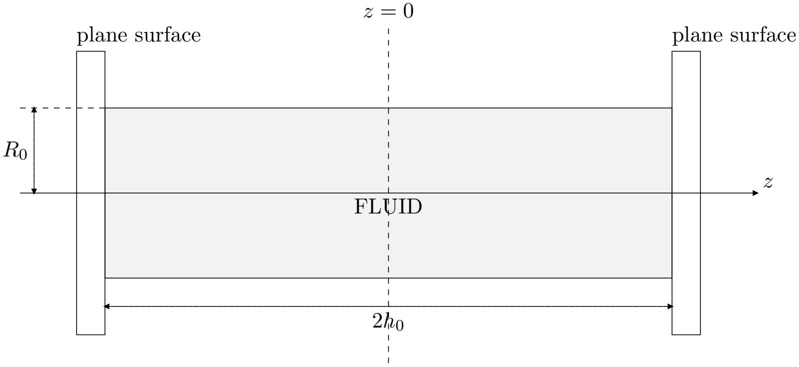

Figure 4.6: The fluid column (Frenkel model)

We assume that the fluid volume is a cylinder (height $2h$ and radius R) throughout the experiment. Since the fluid is incompressible, the volume is kept constant which means that the evolution of the height and of the radius are not independent: $hR^2 = h_0 R_0^2$. In the sequel, it will be convenient to eliminate h, as much as possible

$$h = h_0 \left(\frac{R_0}{R} \right)^2 \tag{4.13}$$

The lateral surface $S = 4\pi hR$ is not constant. Its initial value is $S_0 = 4\pi h_0 R_0$. From (4.13) we get that

$$S = S_0 \frac{R_0}{R}. \tag{4.14}$$

Due to capillary forces, R has the tendency to increase and S to decrease. Since the surface tension between the plates and the liquid is assumed to be zero, the power P_{cap} associated to the capillary forces is simply $P_{cap} = -\gamma_{LG}\dot{S}$, or in terms of h and $\dot{R}$:

$$P_{cap} = \gamma_{LG} S_0 \frac{h}{h_0} \frac{\dot{R}}{R_0}. \tag{4.15}$$

According to the Frenkel's principle, a part of the power P_{cap} is turned into kinetic energy (E_{kin}^{plates} for the plates and E_{kin}^{fluid} for the fluid) and the rest is dissipated by viscous forces (with power P_{vis}). The resulting balance equation:

$$P_{cap} = P_{vis} + \dot{E}_{kin}^{plates} + \dot{E}_{kin}^{fluid}. \tag{4.16}$$

is an equation of motion for R. However, before exploiting it, we still have to express the three terms on the right-hand side as functions of R and of its two first time derivatives $\dot{R}$ and $\ddot{R}$.

We start with the kinetic energy of the plates. It is the easiest to compute. We have

$$E_{kin}^{plates} = M_p \dot{h}^2 \tag{4.17}$$

where M_p denotes the mass of one of the plates[1]. Computing the kinetic energy of the fluid and its viscous power is more intricated. It requires some knowledge about the velocity field inside the fluid. This question is addressed in the next section.

The velocity field inside the fluid column

The velocity field **v** is a divergence free,

$$\operatorname{div} \mathbf{v} = 0, \tag{4.18}$$

solution of the Stokes (or Navier-Stokes) equation for some hydrostatic pressure. Moreover it has to satisfy specific boundary conditions like no-slip and non-penetration boundary conditions on the plates, as well as free surface boundary conditions on the lateral border.

Solving such a complex problem falls of course far from the scope of this work. Since no convenient answers can be found in the literature so far, the goal of this section is simply to build a reasonable velocity field **v**. The construction of **v** will be based on symmetry arguments and on the incompressibility condition (4.18). At the end, we will see that one can define an hydrostatic pressure to satisfy the Stokes equation. Unfortunately the boundary conditions will not be entirely fulfilled. But if we assume that their influence is limited, the prediction we expect for global quantities like the fluid kinetic energy E_{kin}^{fluid} or the total viscous power P_{vis} should be accurate.

The basic symmetry assumption we make is that the velocity has no radial component $v_\theta = 0$ and that the longitudinal velocity v_z is only a function of the longitudinal coordinate z. We go further by applying a first order Taylor expansion and linearizing the dependency of v_z with respect to z. Since v_z must be zero by symmetry (see Fig. 4.6) on the middle plane ($z = 0$), we end up with $v_z = -vz$. The velocity gradient v may depend on time and will be related to h later on. The minus sign in the formula for v_z anticipates the fact the the fluid should flow

---

[1] The plates are assumed to have both the same mass to ensure symmetry.

in the direction of the middle plane ($z = 0$).
At this point, with v_θ and v_z being given, the incompressibility relation uniquely determines the radial component of the velocity. The conclusion is that $\mathbf{v} = v\left(-z\mathbf{e}_z + \frac{1}{2}r\mathbf{e}_r\right)$ with $r = \|\mathbf{r}\|$, $\mathbf{e}_r = \mathbf{r}/r$ and $\mathbf{r} = x\mathbf{e}_x + y\mathbf{e}_y$. If we go back to cartesian coordinates, we get

$$\mathbf{v} = v\left(-z\mathbf{e}_z + \frac{1}{2}x\mathbf{e}_x + \frac{1}{2}y\mathbf{e}_y\right). \tag{4.19}$$

The field $-z\mathbf{e}_z + \frac{1}{2}x\mathbf{e}_x + \frac{1}{2}y\mathbf{e}_y$ between brackets in formula (4.19) has a zero Laplacian and a zero rotational. It derives from the potential $\frac{x^2+y^2}{4} - \frac{z^2}{2}$. Hence, if we define the hydrostatic pressure as $p = \rho\dot{v}(\frac{z^2}{2} - \frac{x^2+y^2}{4})$, we conclude that the evolutive Stokes equation is satisfied.

Unfortunately and as already mentioned, the velocity field (4.19) cannot be consistent with all the boundary conditions which are characteristic of the fluid flow inside the column represented on Fig. 4.6. In particular, the no-slip condition on the plates and the free surface condition on the lateral border are not fulfilled. The only relation we can impose is the non-penetration boundary condition on the plates, at $z = \pm h$. This is done by relating the velocity gradient v to the height h of the column (see Fig. 4.6): $-vh = \dot{h}$ or, using (4.13),

$$v = -\frac{\dot{h}}{h} = 2\frac{\dot{R}}{R}. \tag{4.20}$$

We are now in a position to compute the kinetic energy of the fluid. It is obtained by integrating the density $\frac{1}{2}\rho\mathbf{v}^2$ inside the cylindrical column represented on Fig. 4.6. With $\mathbf{v}$ as in (4.19), we get a simple expression of the kinetic energy density: $\frac{1}{2}\rho v^2(z^2 + \frac{1}{4}r^2)$. Replacing v by its expression (4.20) and integrating, we get

$$E_{kin}^{fluid} = \frac{1}{6}\rho V_0\dot{h}^2 + \frac{1}{4}\rho V_0\dot{R}^2 \tag{4.21}$$

where $V_0 = 2\pi h_0 R_0^2$ is the constant volume of the fluid.
The last step is to compute the viscous power P_{vis}. The heat dissipation

rate (per unit volume) due to viscous effects is related to the viscosity μ and to the strain rate tensor $\varepsilon_{\mathbf{v}}$ by the relation $\mu\varepsilon_{\mathbf{v}} : \varepsilon_{\mathbf{v}}$. The strain rate tensor corresponding to the velocity field (4.19) is constant in space. The distribution we have to integrate to get P_{vis} is simply $\frac{3}{2}\mu v^2$. If we denote again by $V_0 = 2\pi h_0 R_0^2$ the constant volume of the fluid and if we eliminate v by means of (4.20), we obtain:

$$P_{vis} = 6\mu V_0 \left(\frac{\dot{R}}{R}\right)^2 . \tag{4.22}$$

The equation of motion for the height of the column

We substitute the expressions (4.15) and (4.22) of the capillary and viscous powers as well as the expressions(4.17) and (4.21) of the kinetic energies inside the Frenkel balance equation (4.16):

$$(2M_p + \frac{1}{3}\rho V_0)\dot{h}\ddot{h} + \frac{1}{2}\rho V_0 \dot{R}\ddot{R} = \gamma_{LG} S_0 \frac{h}{h_0}\frac{\dot{R}}{R_0} - 6\mu V_0 \left(\frac{\dot{R}}{R}\right)^2 .$$

It is convenient to multiply this relation by the factor $\frac{2R}{V_0\dot{R}}$:

$$(4\frac{M_p}{V_0} + \frac{1}{3}\rho)\frac{R\dot{h}}{\dot{R}h}h\ddot{h} + \rho R\ddot{R} = 2\gamma_{LG}\frac{S_0}{V_0}\frac{h}{h_0}\frac{R}{R_0} - \frac{12\mu}{R}\dot{R}.$$

Further simplifications occur. The factor $\frac{R\dot{h}}{\dot{R}h}$ in the first term of the right-hand side is -2 (see (4.20)) while the ratio $\frac{S_0}{V_0}$ on the right hand-side gives $\frac{2}{R_0}$. As a conclusion, the factor $S_0\, h\, R/V_0\, h_0\, R_0$ after $2\gamma_{LG}$ reduces to $\frac{2hR}{h_0 R_0^2}$ which is exactly $\frac{2}{R}$ because of (4.13). The conclusion is

$$\rho R\ddot{R} - (8\frac{M_p}{V_0} + \frac{2}{3}\rho)h\ddot{h} = \frac{4\gamma_{LG}}{R} - \frac{12\mu}{R}\dot{R}. \tag{4.23}$$

The equation (4.23) has two interesting limiting cases. We discuss them in the next subsections.

The purely viscous case

If the inertia of the fluid and of the plates can be neglected: $M_p \simeq 0$ and $\rho \simeq 0$, we end up with a simple relation:

$$\dot{R} = \frac{R_0}{\tau_1}$$

which balances only the viscous and capillary effects. The characteristic time is

$$\tau_1 = \frac{3\mu R_0}{\gamma_{LG}}.$$

This equation tells that R grows linearly from its initial condition R_0 with a slope $\frac{R_0}{\tau_1} = \frac{\gamma_{LG}}{3\mu}$. Because of (4.13), h vanishes when $t \to \infty$ like t^{-2}:

$$R = R_0(1 + t/\tau_1) \quad \text{and} \quad h = \frac{h_0}{(1 + t/\tau_1)^2}.$$

The non-viscous case

An other limiting case is when the inertia and the viscosity of the fluid are small: $\rho \simeq \mu \simeq 0$. In that situation, the capillary forces only accelerate the plates and the equation of motion (4.23) reads:

$$2M_p\ddot{h} = -\frac{\gamma_{LG}}{hR}V_0$$

and is conservative. After integration, we get back to a balance equation between the kinetic energy of the plates and the free surface energy: $M_p\dot{h}^2 + \gamma_{LG}S = E_0$ for some initial energy E_0. If we use (4.14) and (4.13) to express the surface S in term of h and if we take into account that the plates are initially at rest ($\dot{h}(0) = 0$) we get that

$$\tau_2^2 \left(\frac{\dot{h}}{h_0}\right)^2 = 1 - \sqrt{\frac{h}{h_0}} \tag{4.24}$$

where the characteristic time is

$$\tau_2 = \sqrt{\frac{M_p h_0^2}{\gamma_{LG} S_0}}.$$

Taking into account that h decreases with time from its initial value h_0, we can deduce from (4.24) an integral equation for h. It reads:

$$t = \tau_2 \int_{\frac{h}{h_0}}^{1} \frac{\mathrm{d}u}{\sqrt{1-\sqrt{u}}}.$$

The integrand in the right hand-side has a rational primitive. We conclude that

$$\frac{t}{\tau_2} = \frac{4}{3}(2+\sqrt{\frac{h}{h_0}})\sqrt{1-\sqrt{\frac{h}{h_0}}}. \tag{4.25}$$

This relation is a timetable for the height h. It implies that the two plates collapse ($h = 0$) at a finite time $t_{end} = \frac{8}{3}\tau_2$.

The universal case

None of the simplifications previously presented apply to our situation. Both the viscosity of the fluid and the inertia of the plates (i.e of the grains) have to be taken into account for a proper modelling of the capillary driven flow in selective laser sintering.
As a consequence, the time evolution of the column height h and of the column radius R (see Fig. 4.6) will be obtained after an integration of the full equation of motion (4.23) from the initial data $R(0) = R_0$ and $\dot{R}(0) = 0$ (start at rest) by using the Runge-Kutta method.

4.3 Results

We simulate the fluid flow with the Washburn and Frenkel models (section 4.2.1 and 4.2.2) for the 20 kHz experiment exposed in section 3.3.2. We use the data $h_0 = b$ for the Washburn model, and $h_0 = b/2$ in the case of the Frenkel model. The value of V is taken from table 3.4. We compute R_0 by volume conservation: $R_0 = \sqrt{V/\pi h_0}$. The values of ρ, γ_{LG} and μ are given in table 3.3 and equation (4.12).

With the Washburn model, the result is that the liquid moves within a time t_f=10 μs to get the final neck $a = 56\,\mu$m predicted in table 3.4.

The Frenkel model predicts that the liquid moves within a time t_f=14 μs to reach the same state. The evolution of h and R can be seen on figure 4.7.

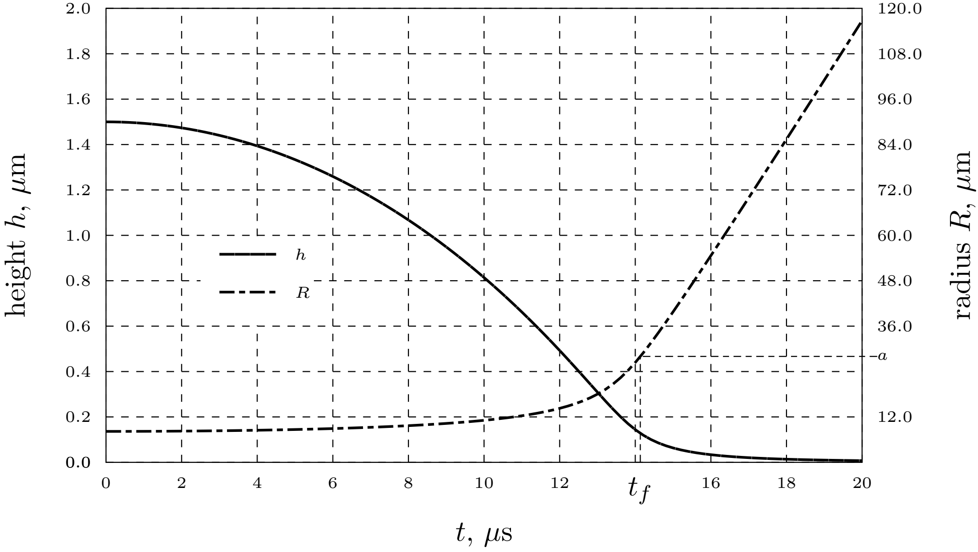

Figure 4.7: Time evolution of the column dimensions (obtained with the Frenkel model)

Both models are in accordance about the liquid lifetime to produce the final neck a. Since the two models are derived with completely different considerations, this result is of great interest.

On the one hand, the Frenkel model allows for the grain inertia, which is neglected by the Washburn model. On the other hand, the Washburn model accounts for a wetting angle and a meniscus. These features are missing in the Frenkel approach.

The next step would be to compare the semi-experimental liquid lifetime t_f to a corresponding quantity obtained from the simulations based on single grain models.

In the particular case of the simulations discussed in section 3.3.2

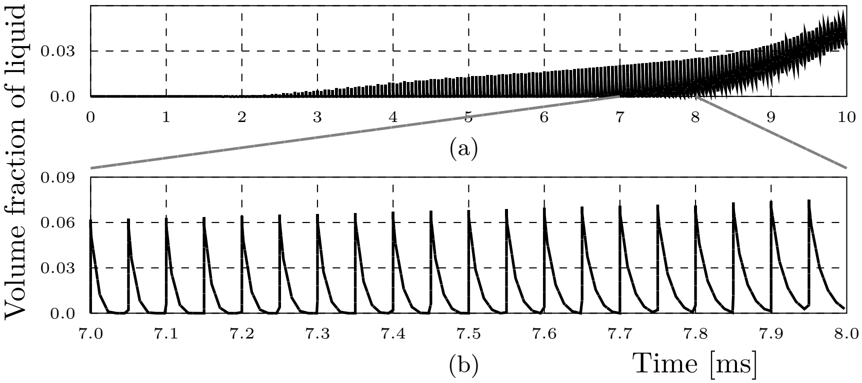

Figure 4.8: Evolution of the quantity of liquid formed for a repetition rate of 20 kHz: (a) full time scale, (b) partial scale

for a 20 kHz repetition rate, there is evidence of liquid lifetime during ~50 μs for each pulse (see figure 4.8). Moreover a part of the particle stays liquid for almost 2 ms at the end of the laser exposition. It is for now difficult to relate these observations to the time t_f needed by the necks to reach their final dimension which is somewhat shorter: $t_f \simeq$10-14 μm from the Washburn or Frenkel models (see figure 4.7). A clue to understand the situation is that all the liquid formed on the particle surface cannot contribute to the neck. Further investigations would anyway be needed to compare the information about liquid lifetime to pure numerical results deduced from mathematical models of selective laser sintering.

4.4 Conclusion

Two approaches have been developed to model the experimental results of Chapter 3. One is based on capillary flow (Washburn model) and the other one on energy considerations (Frenkel model). Both are efficient in predicting a liquid lifetime needed to get the observed interparticular necks. It is encouraging that the times predicted are consistant with each other, although they are derived with completely different hypotheses. This is an argument for the validation of the liquid lifetime predicted. A link to the thermal simulations of Chapter 3 is still missing.

Chapter 5

Scanning strategies in SLM

In SLS, the main parameters are the laser power, the pulse frequency and the scan speed. The scanning strategy is of less importance. In SLM, the goal is to completely melt the powder in order to have dense parts. Consequently, a very high laser power is used and the negative thermal effects (like thermal stresses (see [63]) or balling effects (see [31]) are important. A solution to control them is to adjust the scanning strategy.

In most cases, balling effects can be due to Marangoni convection related to inhomogeneous temperature distributions [64]. In the same way, thermal stresses are related to thermal gradients [65]. The main idea to avoid most of the negative thermal effects is to reproduce the thermal conditions governing classic sintering. In an oven, the whole part is heated smoothly and the temperature gradients are always very low.

In all cases, selecting good scanning strategies might be seen as a constrained optimization problem: The cost function to be minimized measures the amplitude of the thermal gradient ∇T (e.g the time and space average of $||\nabla T||^2$) while the constraint to be satisfied is related to the accuracy of the consolidation. If Ω denotes the volume to be consolidated (according to the CAD data of the part) and if Ω' is the volume really molten (or sintered) after the laser exposition, the constraint can be defined as the measure of the difference between Ω and Ω': $(\Omega' \cup \Omega)/(\Omega' \cap \Omega)$ should be less than a given tolerance.
An algorithmic solution to this optimization problem could be based on

gradient methods, neural networks or genetic algorithms. A possible idea would be to combine those techniques to FEM models for computing the cost and the constraint functions. This very general approach goes however beyond the scope of this work.

Our goal is to present some scanning strategies which help to control the temperature gradient inside the part. We will test them in practice. To allow for the fact that the optimal scanning strategy parameters (e.g the scan speed) have to be adapted to the thermal conductivity of the material, two different powders will be used in the experiments. A gold alloy serves as an example of highly conductive materials while the behavior of poorly conductive materials is illustrated by a tungsten carbide powder coated with stainless steel (304L). Our interest is also to show that a finite element thermal model of the SLS-SLM processes can be efficiently used to anticipate most of the problems (like cracks or ballings) arising in practice. For the sake of simplicity, the simulation will only cover the case of a high conductive material (pure gold).

5.1 State of the art

In SLS pulsed laser have some advantages (see Chapter 3). But in SLM all the powder has to be molten, so continuous mode is preferable.

When too much energy is given to the powder, "balling" occur due to surface energy minimization [31]. At the same time, inhomogeneous thermal shrinkage can cause residual stresses inside the consolidated layers.

Both balling and residual stresses are negative effects. Balling leads to bad surface quality, high porosity and poor consolidation. Residual stresses are responsible for low mechanical properties of the part. They might even cause cracks and failures during the consolidation process itself.

A solution which can be applied to avoid the negative effects is to adapt the scanning strategy (i.e the laser path and the laser speed). Scanning strategy is poorly reviewed in the literature. However, in [66], the authors propose a model for calculating the evolution of temperature and thermal stresses within a single metallic layer on a powder bed using different scanning patterns. They conclude that the best scanning strategy is based on fractals. In [67] a three dimensional FE-model is developed to identify the heat impact on deformations and residual stresses, according to different scanning strategies.

5.2 Numerical model

The three-dimensional model we use to describe the laser-matter interactions and the temperature evolution of the scanned powder bed is described with more details in the references [32], [14]. It is quite similar to the model described in [68]. It allows for a finite latent heat (Stefan-problem [69]) and for conductivity modifications due to the consolidation [70] [71]. One of its main characteristics is to use non-conformal FEM grids [72]. In this way, it can easily limit the influence of imprecise boundary conditions and take the multi-scale aspect of the problem into account: the scale of the powder bed is at least 1000× bigger than the scale of the powder grains. The thermal characteristics of the material to be used in the simulation are listed below.

	bulk	powder	unit
surface absorption α_s[1]	0.885	17.7	%
density ρ	19.32	12.56	g/cm^3
specific heat C_p	0.1323		J/g^{o}C
thermal conductivity k	301	3.01	W/m^{o}C
melting temperature T_m	1064.4		^{o}C
latent heat of fusion L	66.2		J/g

Table 5.1: Thermal properties of gold

---

[1] for a Nd:YAG laser, normal incidence

They correspond to pure gold as illustration of a high conductive material. The values for the bulk material are obtained from [73] and the values for the loose powder are interpolated according to the theory developed in [14].

5.3 Experimental approach

The powders used are WC-steel coated (low conductive) and alloyed gold (high conductive) described in section 2.3.5 and 2.3.4.

Four types of scanning strategy are considered to consolidate a square zone ($5{\times}5\,\mathrm{mm}$) in a single layer (thickness of $50\,\mu$m). The first strategy is a parallel scanning (figure 5.1(a)), the second is a spiral scanning (figure 5.1(b)), the third one is a so-called paintbrush scanning (figure 5.1(c)) and the last one the chessboard scanning (figure 5.1(d)).

The hatching distance h_d is set to be $h_d = 50\,\mu$m. Only the power P and the scan speed v are variable and adapted to the material.
The consolidation effect of each strategy will first be discussed on the basis of melting experiments on different materials (high conductive and low conductive). The results will be compared to simulations (see section 5.2). Two linear probes and five thermocouples (figure 5.2) are used to analyze the temperature field resulting from the simulation.

5.4 Results

5.4.1 Parallel scanning

The parallel scanning (figure 5.1(a)) has the advantage of being the easiest to generate from a CAD file. At low speed, it leads to large temperature gradients all over the square surface to be consolidated which is an unfavorable situation (see section 5.1).

Simulation results show that a feasible solution to decrease temperature gradients is to use higher scan speed v. By letting $v \to \infty$, we

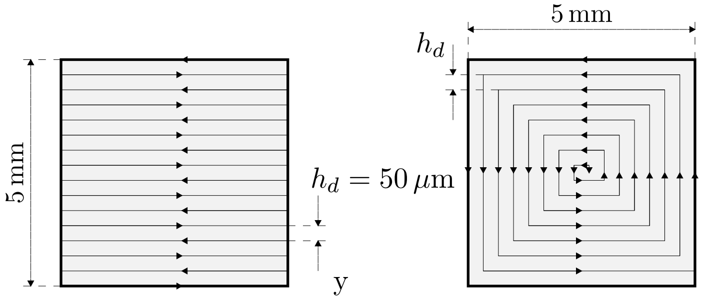

(a) parallel scanning (b) spiral scanning

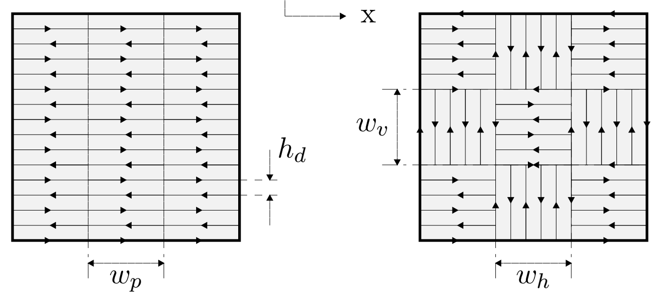

(c) paintbrush scanning (d) chessboard scanning

Figure 5.1: The four scanning strategies

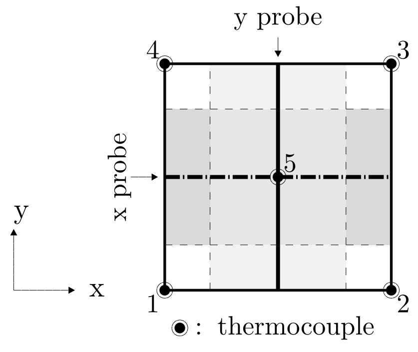

Figure 5.2: Probes and thermocouples position

tend to homogeneous energy deposition (see section 5.1). However, the highest scan speed one can use depends on the galvo head possibilities. Moreover, to avoid depositing less and less energy, the power has to be increased in the same proportion as v. Since laser powers are usually limited to a few dickers of W, a way to increase v without depositing less and less energy is the so-called *multiple scanning strategy*: the speed v is multiplied by an integer n ($n = 2, 3..$), the power is not modified but the laser beam goes through the scanning path not once but n times.

Figure 5.3 shows the evolution in time of the mean square of $\partial_x T$ and $\partial_y T$ as they are deduced from the numerical model (see section 5.2) for both the multiple scanning at high speed and the single scanning at low speed. This figure demonstrates the benefit of multiple scanning with $n = 10$.

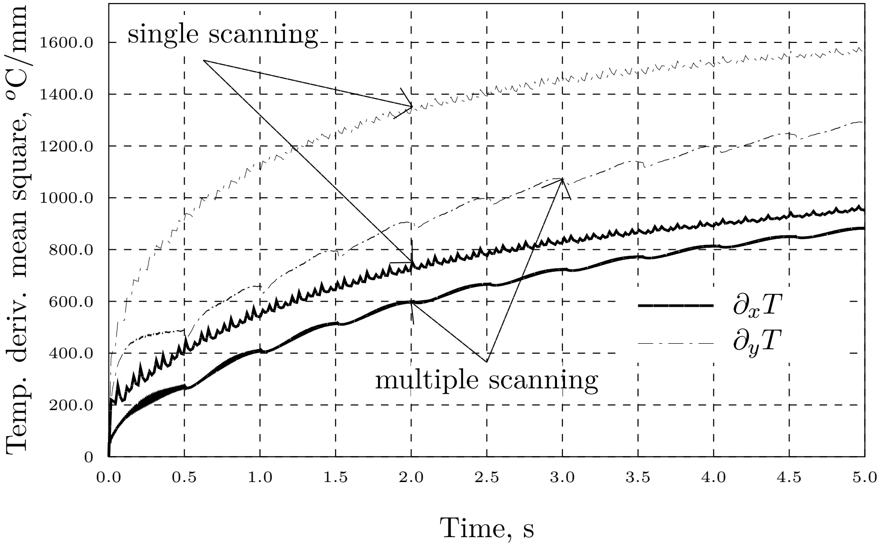

Figure 5.3: Mean square of the temperature partial derivatives (gold powder)

However even at high speed and reasonable power, the parallel scanning leads to balling and cracks on the two sides that are perpendicular to the scanning direction (figure 5.4).

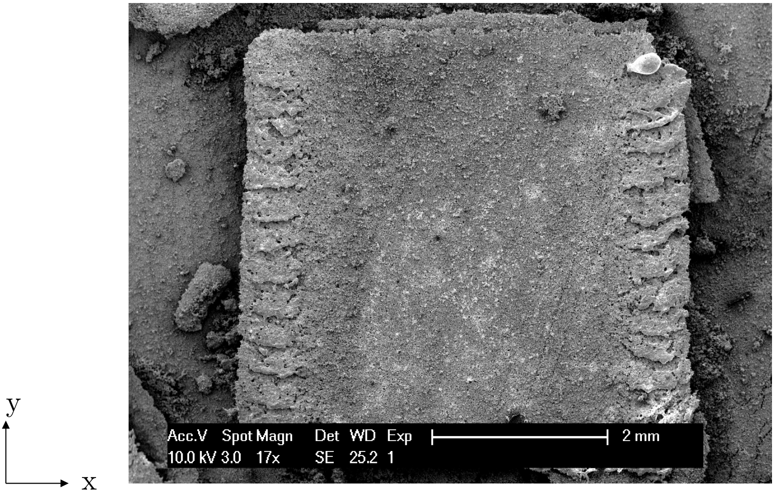

Figure 5.4: Parallel scanning in gold powder (scanning direction=x)

Overheating might be a first explanation to the crack problem. To confirm this hypothesis, a simulation of the above experiment has been performed (see section 5.2). On figure 5.5 we plot the maximal temperature profiles after the first scan which are measured along the two linear probes of figure 5.2. The profile in the x direction confirms a temperature rise near the sides of the platelet.

In comparison with thermal simulations, fluency[2] computations are faster. Unfortunately they are not able to anticipate any risk of overheating (figure 5.6). The overheating phenomena observed in figure 5.5 is actually not due to excessive energy deposition. It is caused by the way the energy is deposited in time.

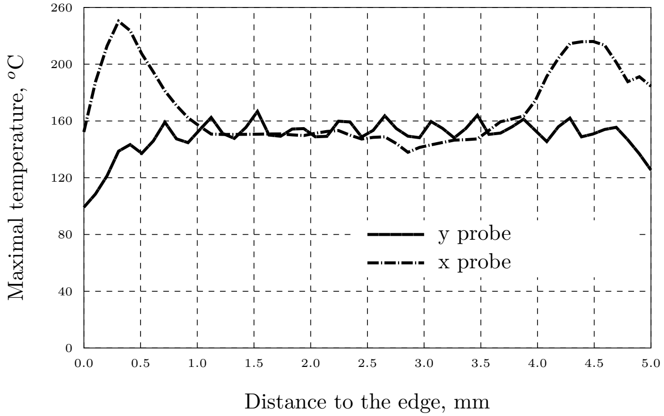

Figure 5.5: Maximal temperature profiles (gold powder)

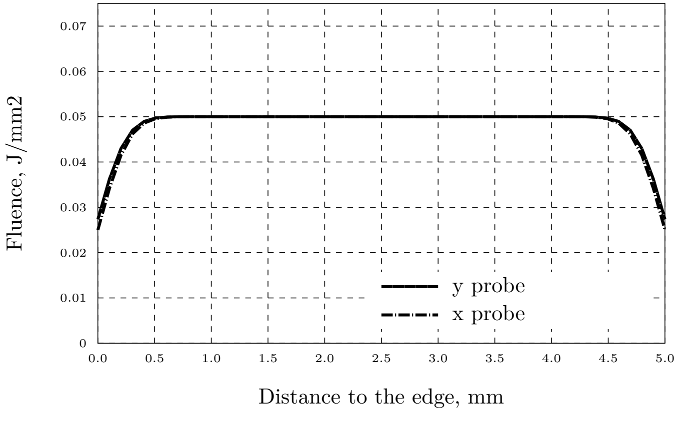

Figure 5.6: Fluency profiles along the linear probes (gold powder)

Thermal stresses can also be an explanation for the cracks observed on figure 5.4. In a parallel scanning strategy, the temperature

---

[2] the fluency is the sum of the laser intensity over the exposition time

gradient is *essentially* orthogonal to the scan direction. This fact is illustrated on figure 5.3 where it can be seen that the component $\partial_y T$ dominates the component $\partial_x T$.
In our case, the scan direction is parallel to the x-axis and the temperature gradient is almost parallel to the y-axis. The resulting inhomogeneous shrinkage causes residual *bending stresses* in the y-axis direction (the direction of ∇T). If these stresses are stronger than the mechanical resistance of the consolidated medium, they lead to cracks in the x-axis direction (the scanning direction) exactly like the cracks on figure 5.4.

5.4.2 Spiral scanning

A possible solution to avoid overheating near the sides perpendicular to the scanning direction and to equilibrate the two components $\partial_x T$ and $\partial_y T$ of the temperature gradient is to use spiral-like scanning (figure 5.1(b)).

If the scan speed is high enough, the spiral scanning leads to better results than the parallel line strategy. Figure 5.7 shows a sound platelet consolidated at high speed using a *multiple* spiral scanning.

The basic condition for the multiple scanning to work is that heat losses in the metal between each single scan are small compared to the deposited energy. For high conductive powders, it means that one has to choose high scan speed, high laser power and only small surfaces can be scanned. Simulation has been used to design the operating parameters (laser power and scan speed) used to produce the part of figure 5.7. The simulated temperature evolution is presented on figure 5.8 during ten scannings for the two thermocouples at vertex 1 and in the middle (figure 5.2). Due to symmetry, the thermocouples at vertices 2, 3 and 4 react like the thermocouple at vertex 1. It may also be observed on figure 5.8 that the piece temperature is increasing (a few hundred degrees) at each scan. If the powder is highly conductive, the multiple spiral scanning leads to very strong bonding between layers (figure 5.9).

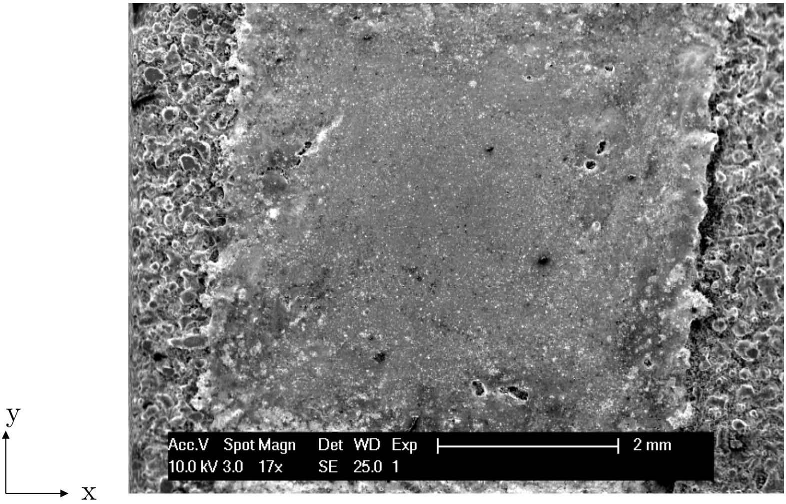

Figure 5.7: Multiple spiral scanning of gold powder

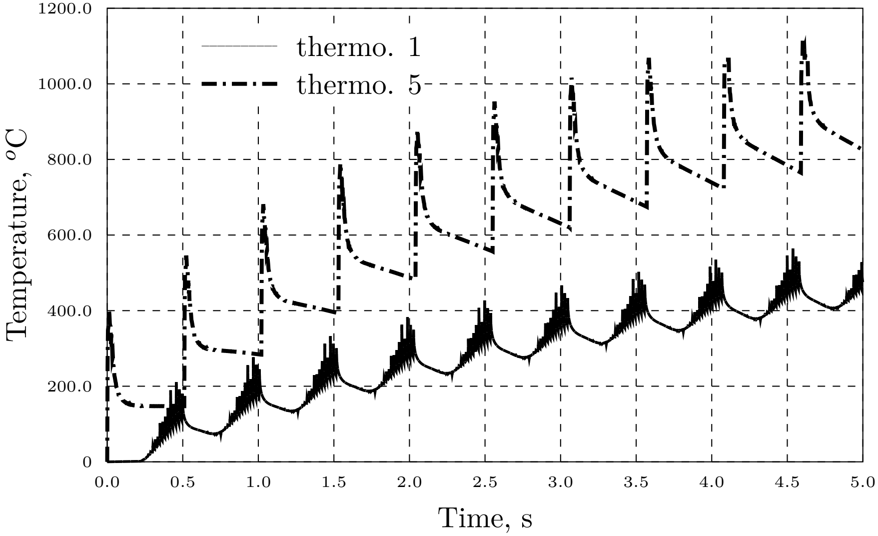

Figure 5.8: Temperature evolution in multiple spiral scanning (gold powder)

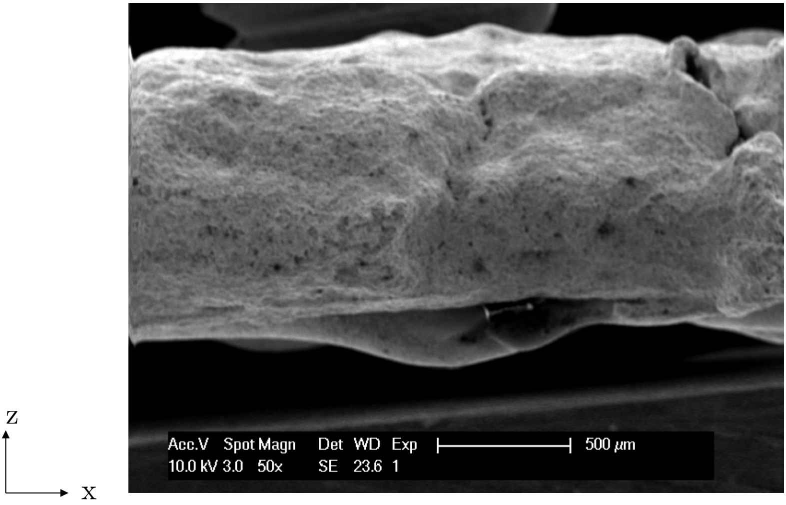

Figure 5.9: Layer bounding in gold powder under spiral scanning

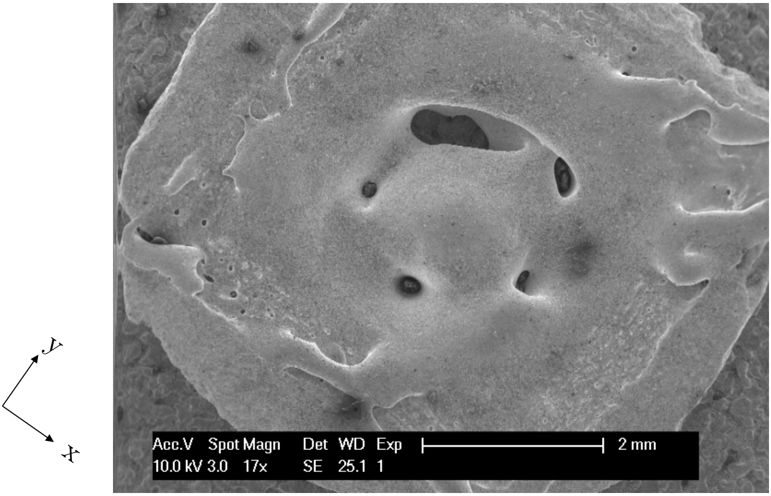

Figure 5.10: Loss of accuracy after a spiral scanning of gold powder

But the very good heat transfer has also a big impact in the x, y directions and on the final geometry of the part. Zones not illuminated by the laser might also be molten. In that case, the accuracy of the construction is lost, as can be seen on figure 5.10.

It has to be stressed that the spiral scanning strategy also leads to a serious overheating problem in the center of the part. The higher temperature in the middle is confirmed by the thermal model. A simulation of the experiment leading to the platelet of figure 5.10 has been performed and figure 5.11 shows the maximal temperature profiles along the linear probes of figure 5.2.

Figure 5.11 also represents the melting temperature level ($T_m = 1064.4^o$ C, table 5.1). Comparing the maximal temperature to the value T_m, we come to the conclusion that the material in a zone (approximately a square of width $w \simeq 1.25\,\mathrm{mm}$ in the middle of the platelet is completely melted (see figure 5.11). This simulation result can be linked to the experimental observations on figure 5.10. The molten region actually corresponds to the center of the platelet presenting a rough surface (balling) and surrounded by pores.

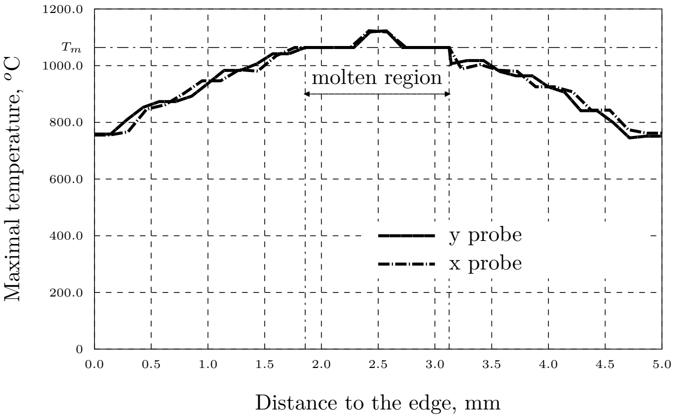

Figure 5.11: Simulation of the maximal temperature profiles after 10 spiral scannings (gold powder)

In the case of the low conductive powder, heat cannot be evacuated fast enough. The consequence is that it is difficult to find parameters[3] leading to good consolidation results with the multiple spiral scanning strategy. The best result we have obtained (10 scans with P=100 W and v=50 mm/s) are represented on figure 5.12. In addition to lack of accuracy, we observe balling and cracks everywhere.

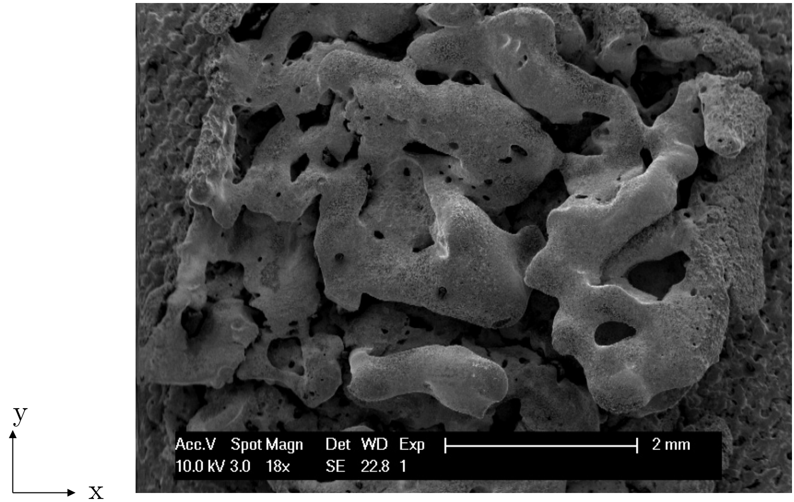

Figure 5.12: Spiral scanning on WC-steel coated powder

5.4.3 Paintbrush scanning

Paintbrush scanning is similar to parallel scanning. The difference is that the scan width w_p (figure 5.1(c)) is much smaller (in the following experiments $w = 2.5\,\text{mm}$). They can be used as an alternative to limit overheating and temperature gradients for both low and high conductivity powder. Parameters (power and scan speed) leading to dense parts and respecting the accuracy can be found. They are listed in table 5.2.

---

[3] e.g. power, scan speed and number of scans.

	Gold	WC-steel coated
Power P [W]	100	16.5
Speed v [mm/s]	100	150
Hatching distance h_d [μm]	50	50
Layer height e [μm]	50	50

Table 5.2: Parameters for paintbrush scanning

Figures 5.13 and 5.14 give examples of the consolidated quality obtained with gold and WC-steel coated powder respectively.

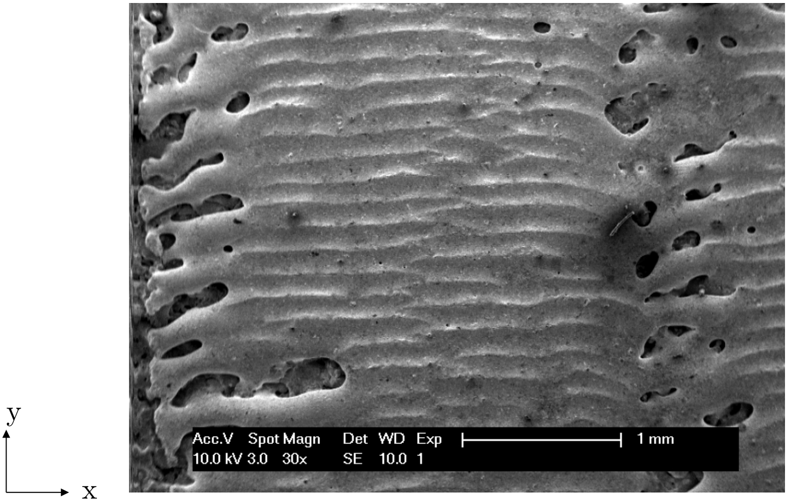

Figure 5.13: Paintbrush scanning of gold powder (scanning direction=x)

However the bonding between layers is not perfect, especially for the first layers, as illustrated by figure 5.15. This effect leads to delamination when tall parts are built.

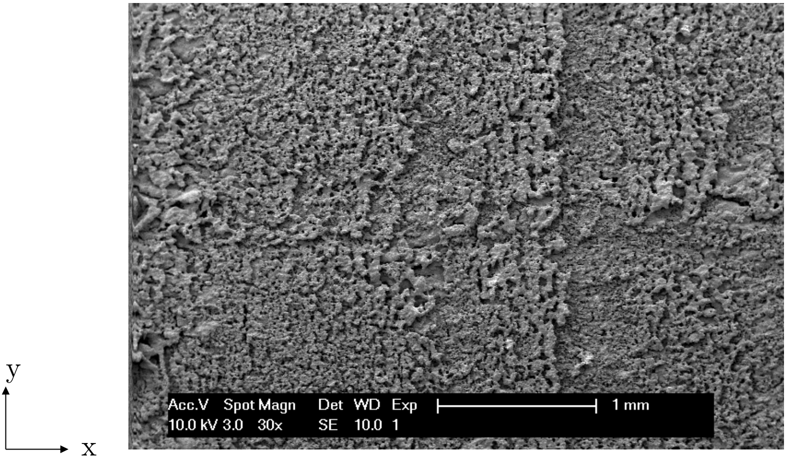

Figure 5.14: Paintbrush scanning of WC-steel coated powder (scanning direction=x)

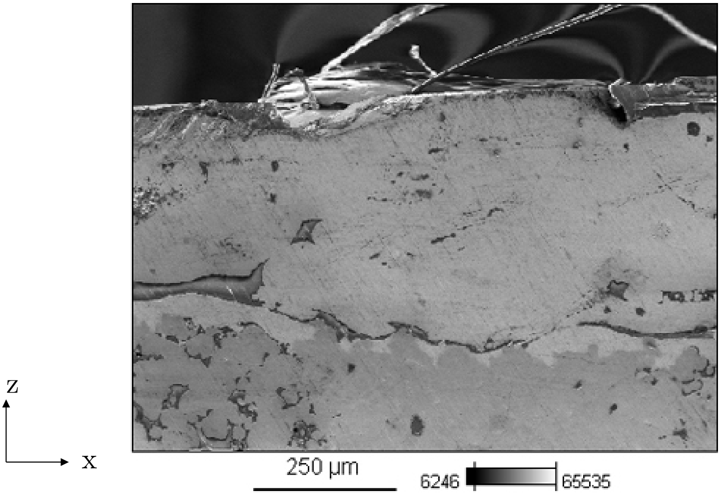

Figure 5.15: Layer bounding in gold powder under paintbrush scanning (scanning direction=x)

5.4.4 Chessboard scanning

The chessboard scanning strategy (figure 5.1(d)) consists of dividing the area to consolidate into small cells (width w_h and w_v). Parallel scanning in alternate directions is then applied to each cell. chessboard scanning can be seen as a *scaling down* of the standard parallel scanning strategy. This scaling down modifies the thermal dynamics and limits the temperature inhomogeneities. It is however important to scan the small cells in a *random* order. Figure 5.16 (respectively figure 5.17) presents a well consolidated platelet in gold powder (respectively in WC-steel coated powder). In both cases, the unit cell width is $w_h = w_v = 1\,\text{mm}$. The parameters are listed in table 5.3.

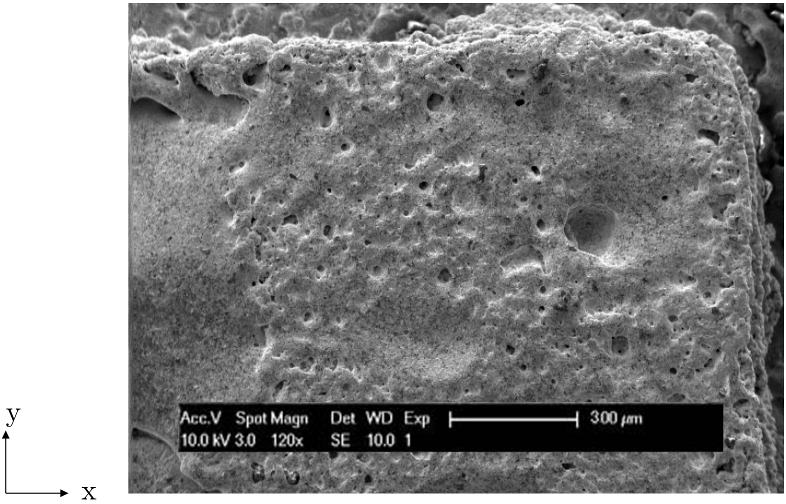

Figure 5.16: Chessboard scanning of gold powder

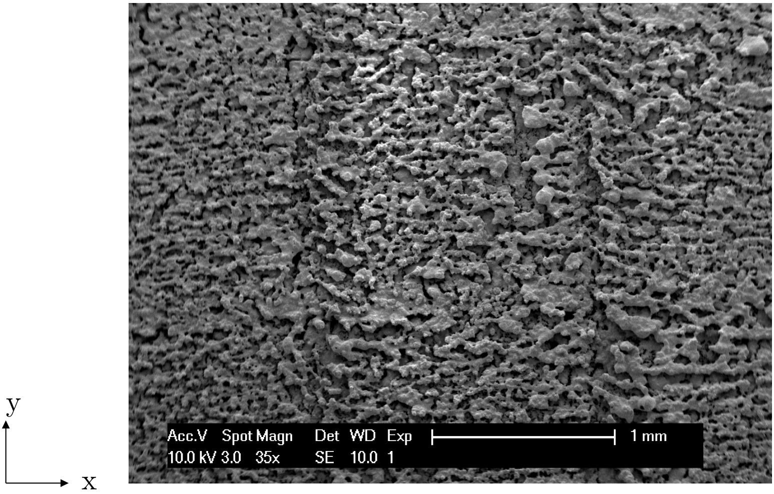

Figure 5.17: Chessboard scanning of WC-steel coated powder

	Gold	WC-steel coated
Power P [W]	100	16.5
Speed v [mm/s]	100	90
Hatching distance h_d [μm]	50	50
Layer height e [μm]	50	50

Table 5.3: Parameters for chessboard scanning

This strategy should be the best but the difficulty to create suitable CAD files prevented the optimization of the laser parameters.

5.5 Analyses

Analyses have been made on gold paintbrush-style scanned pieces, since they exhibit the best results. The following pieces have benn made with the parameters listed in table 5.2.

5.5.1 Accuracy analyses

A Keyence digital microscope VHX-600 (Génération 2) is used to achieve accuracy measurements on a 3D profilometry image. The analyzed piece is composed of five paintbrush stripes of 2 mm width each with a squared hole in the center (see figure 5.18).

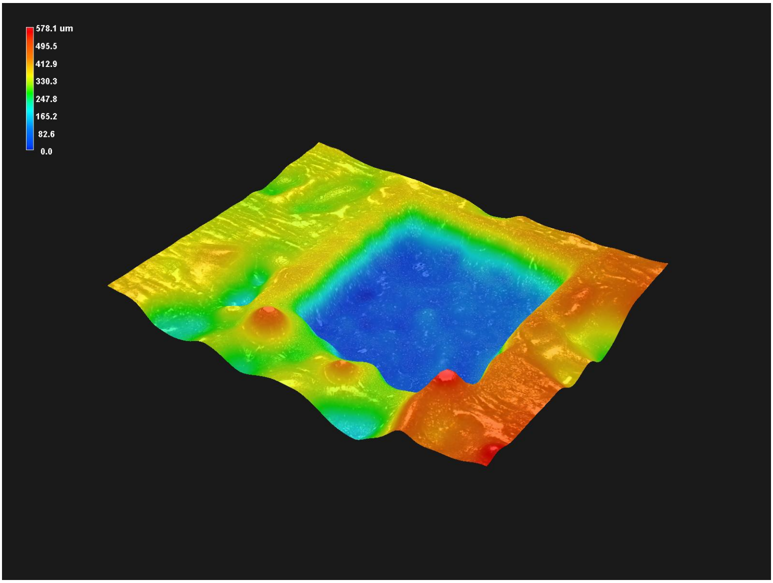

Figure 5.18: 3D profilometry of paintbrush stripes with hole

The side of the squared hole had to be 2 mm. In the profile measured on figure 5.19 it is 1.48 mm (length (D-C)).

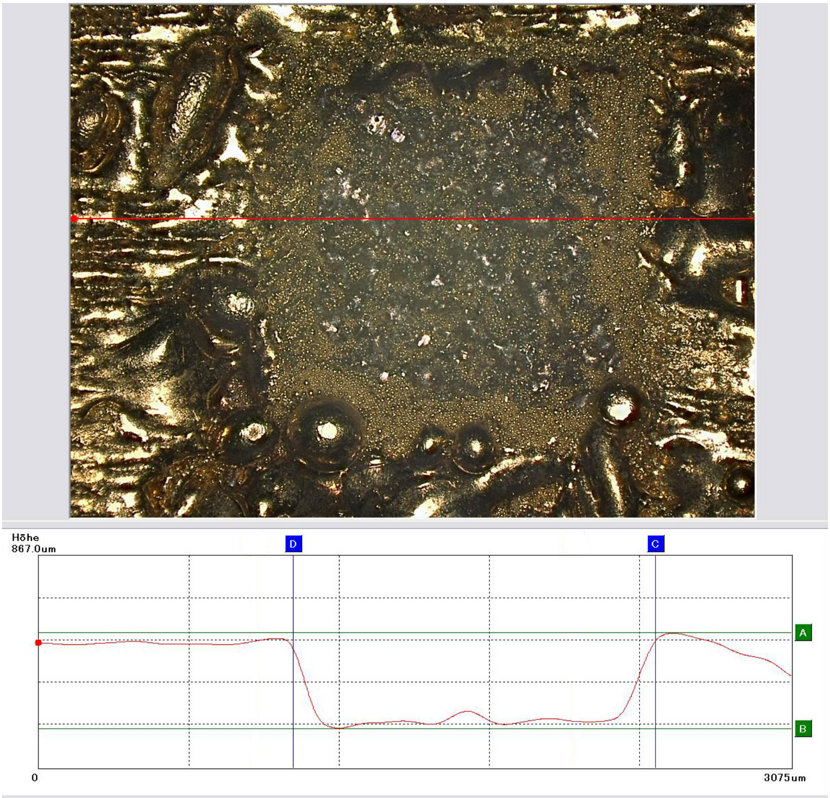

Figure 5.19: Profile of the hole between paintbrush stripes

The heat flux in the non-illuminated powder is responsible for this difference. The borders of the square solidify without being illuminated.

This phenomenon has been simulated by mean of the numerical model presented in section 5.2. We have considered the consolidation of a single layer on a substrate. The layer thickness was of 0.1 mm and the substrate was pure gold with a thickness of 2.4 mm. The real substrate is of course thicker (see figure 2.10) and is based on the moving z-table of the SLS machine (see figure 2.5). However those details have not to be taken into account since the heat penetration depth (as it is obtained after simulation) is of about 1 mm.

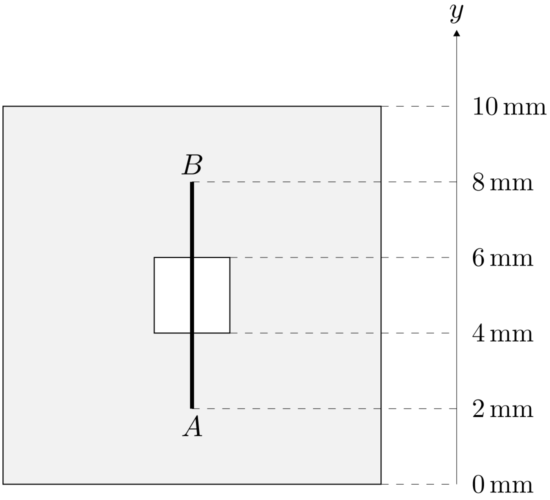

Figure 5.20: The part, the scan direction y and the studied profile AB

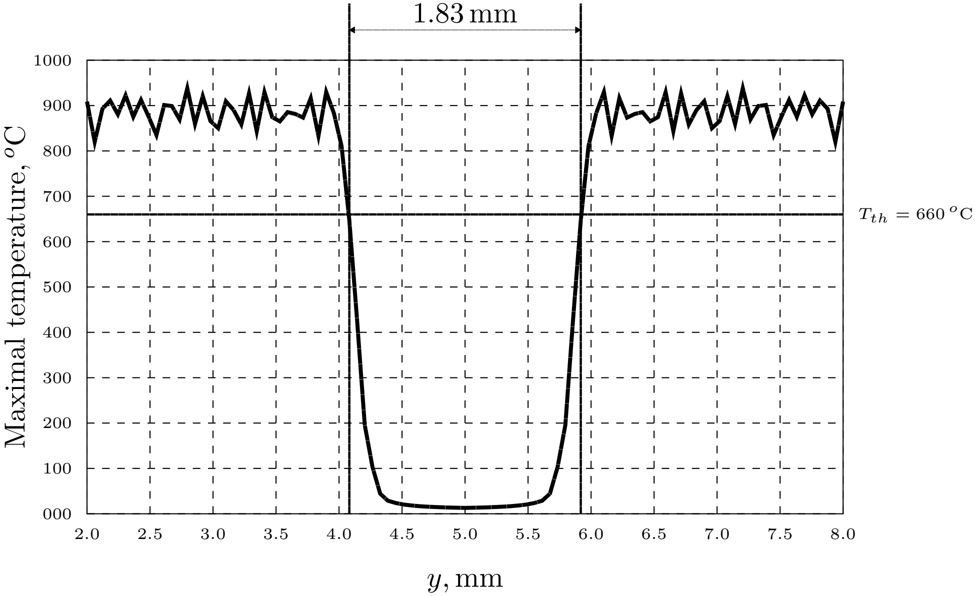

Figure 5.21: Maximal temperature profile (obtained by simulations)

The values of the thermal and absorption coefficients for the powder bed have been taken in table 5.1 except the thermal conductivity k. For this experiment, the value of table 5.1 ($k = 3.01\,\mathrm{W/m^oC}$) representing only 1% of the bulk thermal conductivity was likely too small. We have chosen a higher value:

$$k = 18.06\,\mathrm{W/m^oC}. \tag{5.1}$$

It corresponds to 6% of the bulk thermal conductivity and is still plausible [14]. The thermal coefficients for the substrate (pure gold) are also available from table 5.1.

The simulation result is the macroscopic temperature distribution T and its evolution in time. Information about the shape of the sintered part can be obtained by processing the temperature field T [14]. A possibility is to consider the maximal macroscopic temperature T_{max} reached by each point. In that case, the consolidation criterion for a point P may be $T_{max}(P) \geq T_{th}$ where T_{th} is a threshold temperature. By analogy with solid state sintering, the value of T_{th} is chosen to be 70% of the melting temperature T_m (absolute scale).

The maximal temperature profile along the segment AB (see figure 5.20) has been extracted from the simulation and has been represented on figure 5.21. The consolidation threshold is $T_{th} = 660\,^o\mathrm{C}$.

We observe that the simulation predicts a hole diameter of 1.83 mm, which is quite in agreement with the measured hole diameter of figure 5.19.

The square to square scanning strategy should overcome this loss of accuracy problem caused by heat diffusion, because of the smaller heated surface dimension involved.

5.5.2 EBSD analyses

Figure 5.22 shows a paintbrush scan of gold powder and an EBSD analysis of one of its border.

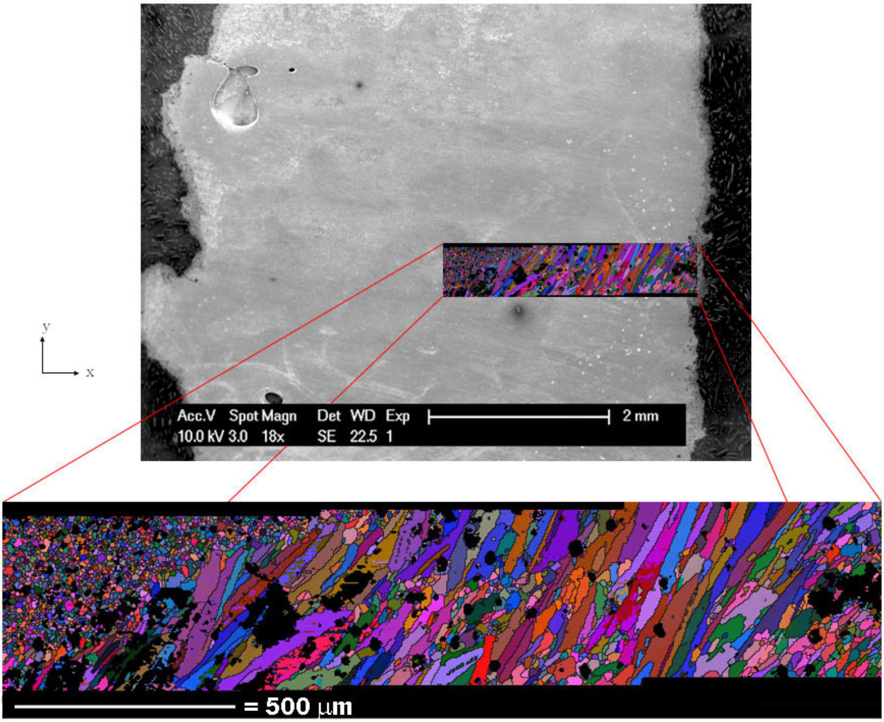

Figure 5.22: EBSD analysis of a paintbrush scanning

Each color corresponds to a different crystallographic orientation. There is no preferential orientation.

There are two different groups of grains. At the border, columnar grains can be seen, following the thermal gradients. At a certain distance from the border a transition occurs and equiaxed grains appear, with no preferential crystallographic orientation[1].

The transition can be explained by the same argument as in section 5.4.1. As shown by the simulations (see figure 5.5), the borders of the

---

[1] The use of Hunt's criterion [74] would be needed to ensure that a columnar-to-equiaxed transition really occurs in that case.

scanned area are overheated. The temperature reaches higher values and the thermal gradients are considerable. A part of the previously solidified grains is remelted. Therefore the solidifying material can keep the same crystallographic orientation and it is known, as studied in [75], that grains oriented towards the thermal gradient grow preferentially. On the contrary, at the center, the relatively large cooling rates and small temperature gradients lead to high liquid undercoolings and to the nucleation of equiaxed grains.

In general equiaxed grains, which lead to an isotropy of the mechanical properties, are preferable. So it appears that the columnar grains have to be avoided and scanning strategies favorable to equiaxed grains should be chosen. This EBSD analysis is another evidence that thermal gradients are not welcome.

A cut through the different layers of a piece made with paintbrush scanning has been analyzed via EBSD (see figure 5.23).

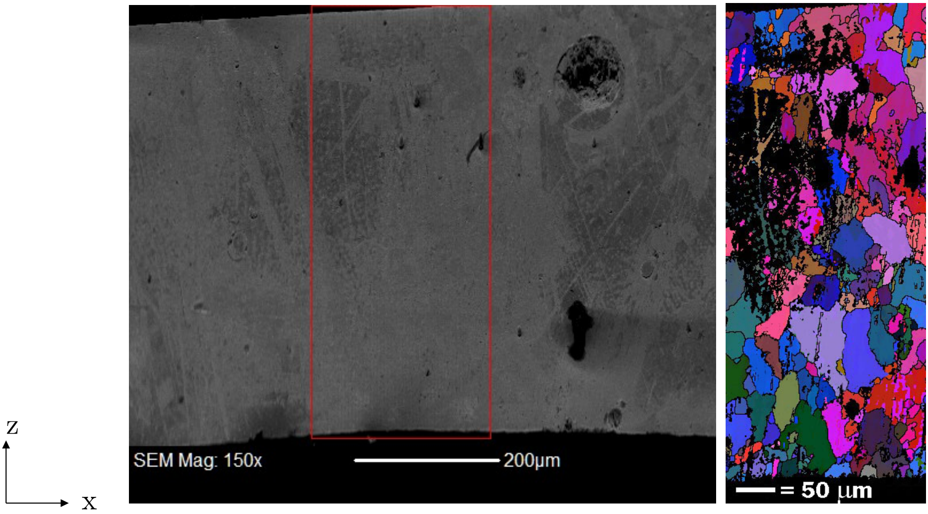

Figure 5.23: EBSD analysis through the different layers

The layers are 50 μm high. The black parts on the picture aren't necessarily pores but parts where the EBSD software couldn't find any crystallographic informations, maybe due to the presence of resin. There is no apparent cracks between them, and the grains have grown sometimes through two or three layers. When a layer is illuminated, the metal of the previous layer is remelted, and the previous crystallographic orientations is kept. This ensures a good bonding between the layers, and good mechanical properties can be expected.

Combining simulations and EBSD analysis helps choosing the best scanning strategies to get limited grain growth, isotropic material and good mechanical properties.

5.6 Conclusion

We have shown that the parallel scanning strategy has some drawbacks. It has to be used in a multi-scan mode to avoid consolidation problems. At least for high conductive powder, the situation can be improved by spiral scanning. However spiral scanning is difficult to generate for non convex domains.
An interesting alternative is to scale down the parallel scanning and to go either to paintbrush or to chessboard scanning strategies in multi-scan mode. Since the areas to consolidate are smaller, the temperature homogeneity is easier to maintain. EBSD analysis show the benefits that can be obtained from minimizing thermal gradients.
An important output of this chapter is that using the numerical model described in section 5.2 is an inexpensive and efficient way to evaluate the drawbacks and the benefits of a given scanning strategy. It is able to detect overheated zones or high temperature gradients. In the future, it could be combined to selection algorithms (e.g. genetic algorithms), to form a computer-based tool for generating adapted scanning strategies.

Chapter 6

Applications

The aim of this chapter is to show some applications of SLS/SLM on different pieces built either with pulsed or continuous power. The range of laser parameters used is very different for each powder and requires precise optimization. The benefits that can arise from the simulations of Chapters 3, 4 and 5 are finally stressed.

6.1 FHNW mold

The FHNW mold (see figure 6.1) is a test part proposed by the Hochschule für Technik (Bereich Transfer) in Windisch (CH) [76]. It was built with the H13 powder (see section 2.3.2). The parameters used are listed in table 6.1.

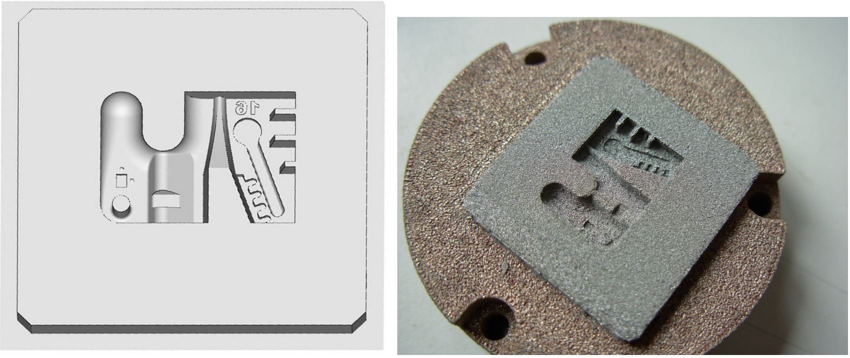

Figure 6.1: The FHNW mold

Mode Scanning strategy	Multimode parallel scanning
Power P [W]	8
Speed v [mm/s]	40
Pulse frequency f [kHz]	3
Hatching h_d [μm]	50
Layer height e [μm]	40

Table 6.1: Parameters for H13 powder

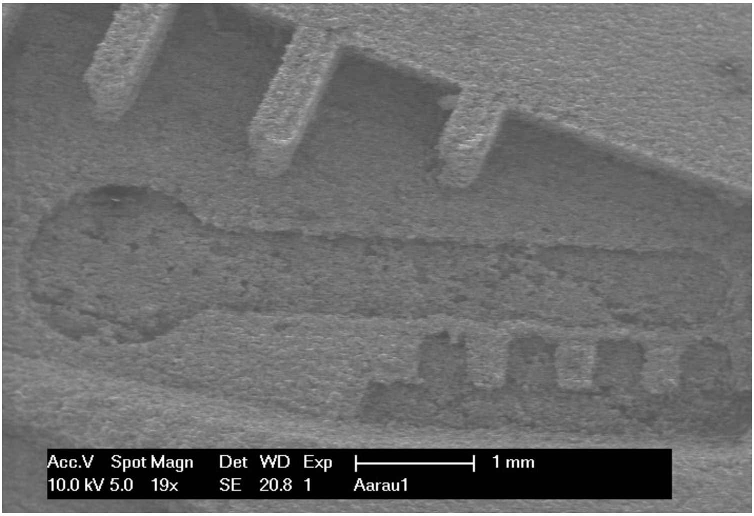

Figure 6.2: The FHNW mold - details

Profilometry analysis (see figures 6.3 and 6.4) are performed on the little strips shown in figure 6.2. The accuracy is +/-5 μm. The average density is 50% of the bulk density.

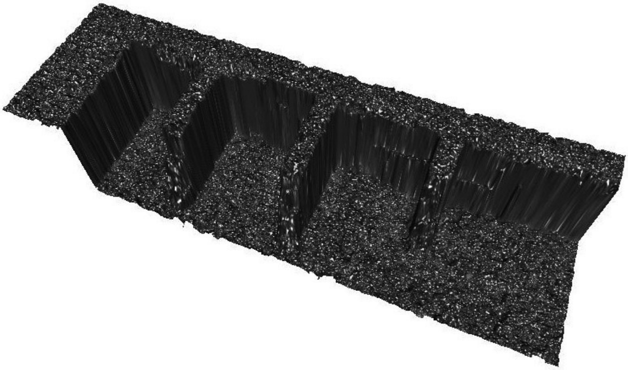

Figure 6.3: The FHNW mold - profilometry 1

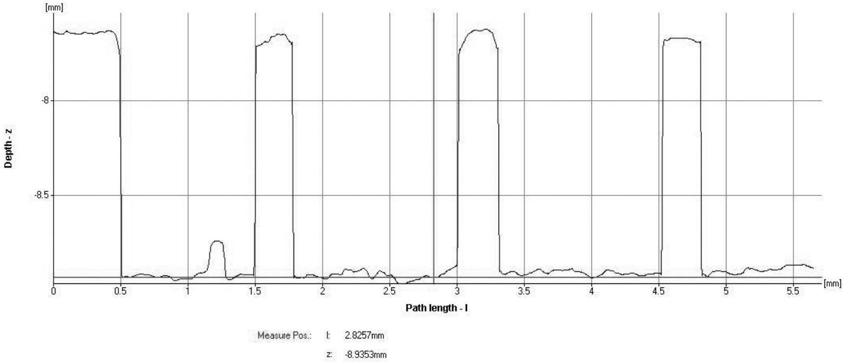

Figure 6.4: The FHNW mold - profilometry 2

6.2 Watch clasp

This piece was made out of silver powder (see section 2.3.3). The parameters used are listed in table 6.2:

Mode Scanning strategy	Multimode parallel scanning
Power P [W]	20
Speed v [mm/s]	10
Pulse frequency f [kHz]	5
Hatching h_d [μm]	50
Layer height e [μm]	40

Table 6.2: Parameters for silver powder

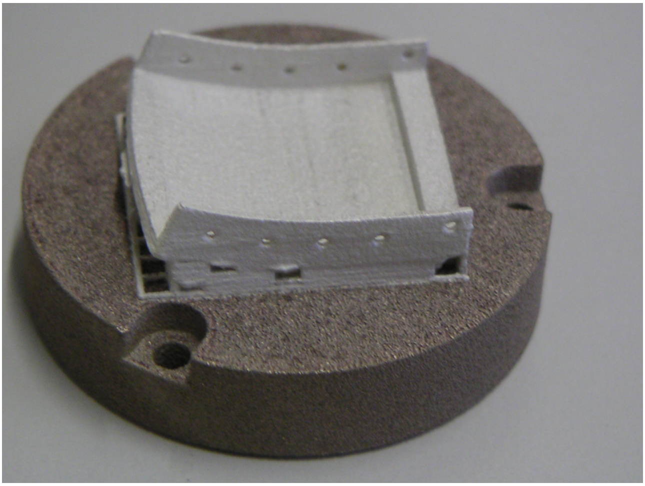

Figure 6.5: The watch clasp

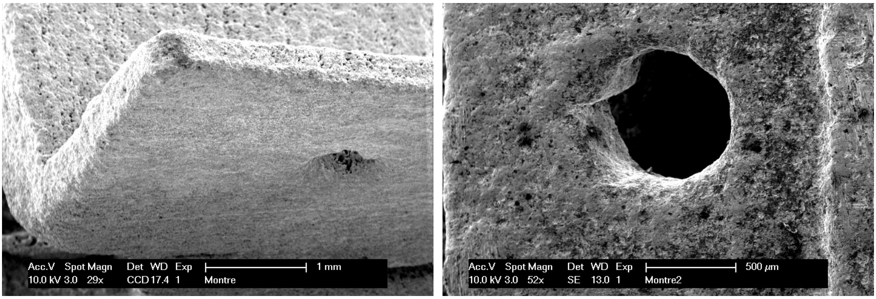

Figure 6.6: The watch clasp - details

The density is 65% of the bulk density.

6.3 Benchmark

In order to test the final accuracy of the pieces obtained with each powder, a benchmark (see figure 6.7) similar to the one described in [13] has been built with the best parameters found.

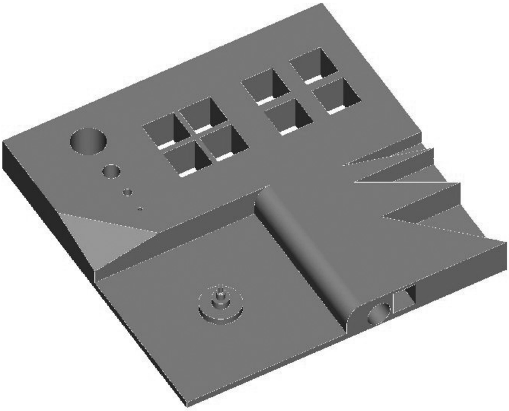

Figure 6.7: The benchmark

The dimensions of this benchmark part are summarized in table 6.3.

Form	Decreasing dimensions
Round holes	2 / 1/ 0.5 / 0.25 mm
Distance between square holes	1 / 0.5 / 0.3 mm
Superposed cylinders	2.5 / 1 / 0.5 / 0.25 mm
Angles	45 / 30 / 15 °

Table 6.3: Dimensions of the benchmark part

6.3.1 H13

The H13 powder is described in section 2.3.2. The parameters used are listed in table 6.1.

Pictures and details of the H13 benchmark part are shown on figure 6.8. Two of the four superposed cylinders were not built (500 and 250 microns diameter). The smallest of the four holes wasn't built (250 microns diameter). The average accuracy is +/-100 μm. The angles have an accuracy of +/-5°. The density of the piece is 50% of the bulk density.

6.3.2 Silver

The silver powder is described in section 2.3.3. The parameters used are listed in table 6.2.

Pictures and details of the Silver benchmark part are shown on figure 6.9. The four superposed cylinders were not built. The smallest of the four holes wasn't built (250 microns diameter). The average accuracy is +/-300 μm. The angles have an accuracy of +/-15°. The density of the piece is 65% of the bulk density.

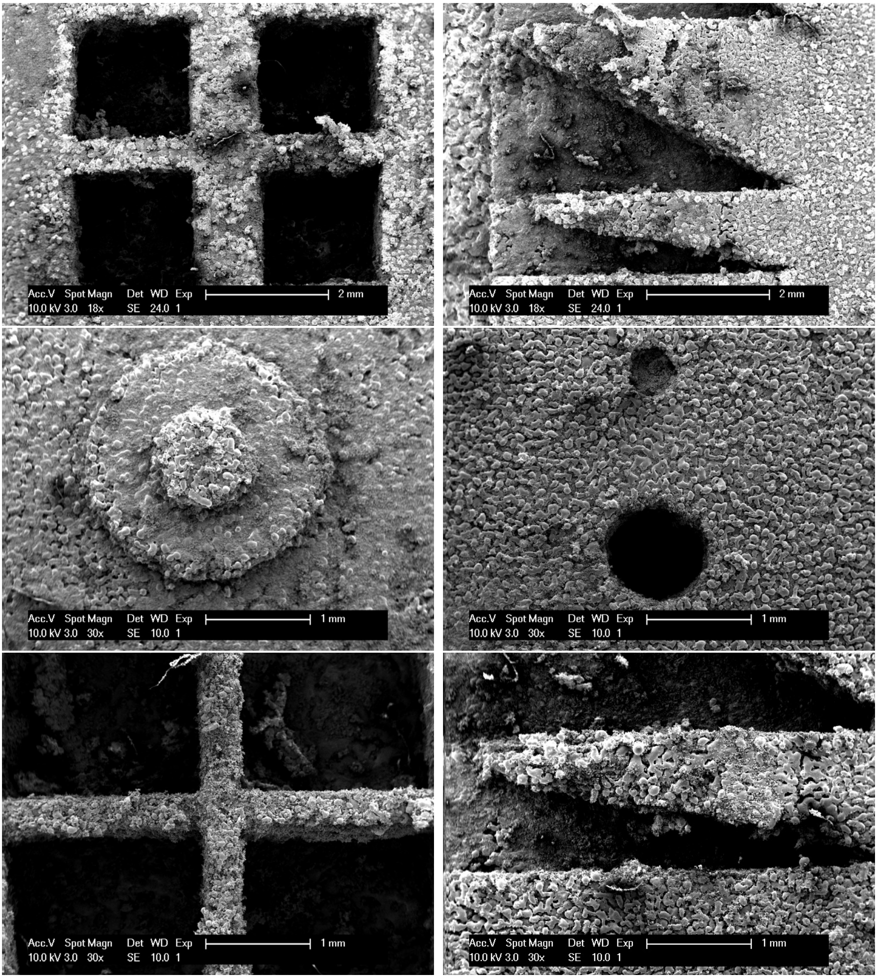

Figure 6.8: The H13 benchmark part

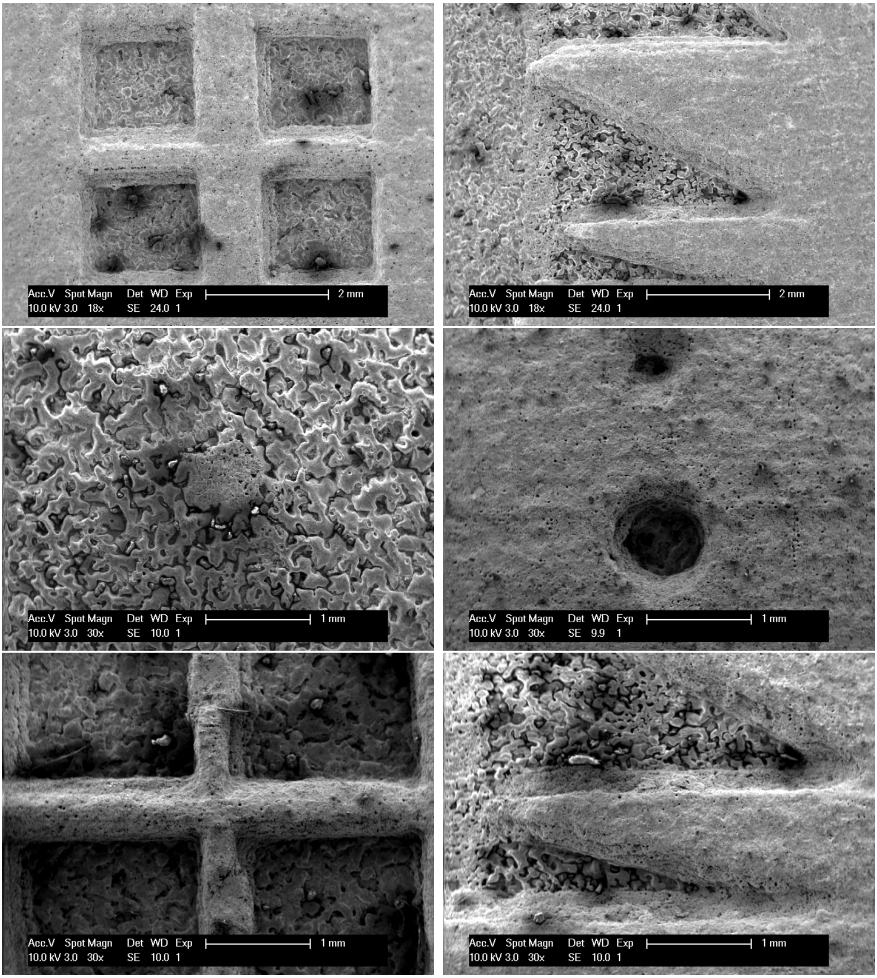

Figure 6.9: The Ag benchmark part

6.3.3 Gold

The gold powder is described in section 2.3.4. The gold benchmark part has been produced with the parameters listed in table 6.4:

Mode Scanning strategy	Multimode parallel scanning
Power P [W]	17.9
Speed v [mm/s]	40
Pulse frequency f [kHz]	10
Hatching h_d [μm]	50
Layer height e [μm]	50

Table 6.4: Parameters for gold powder

Only the squares and circles shapes have been successfully built (apart of the smallest of the four holes). The average accuracy is +/- 100μm.

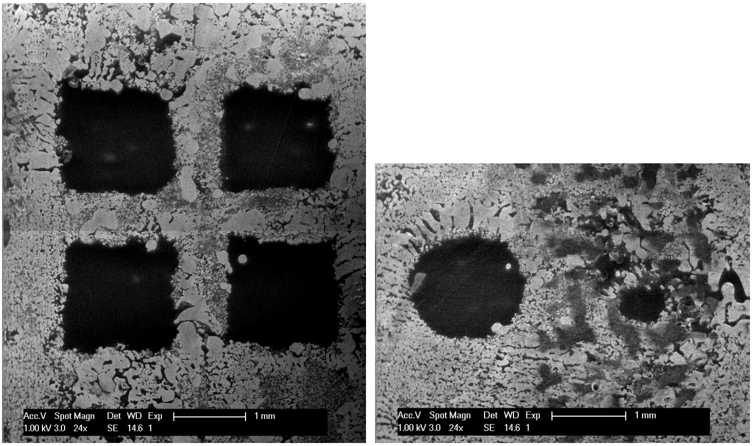

Figure 6.10: The Au benchmark

Pulsed mode has been prefered to continuous mode because of the higher accuracy possible even if the final density is not good. We have 82% density on picture 6.11 taken from the same benchmark.

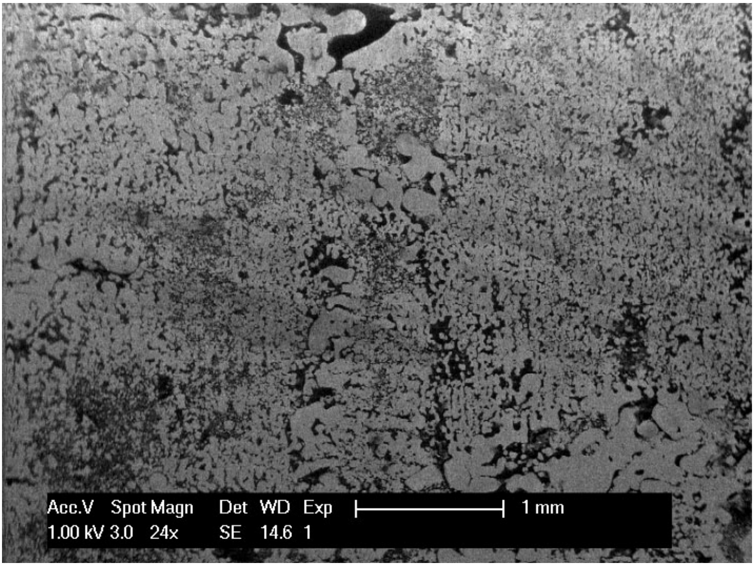

Figure 6.11: The Au benchmark - density

6.3.4 Remark

This benchmark study points out the advantages and drawbacks of a chosen set of parameters for each powder. Other sets of parameters have led to better density, but there was a decrease of accuracy, and vice versa. The sets proposed in this section are the best compromises found for the moment, but their presence in this chapter is only thought to be a starting point for further optimization studies.

6.4 A new way to build support structure

An European provisional patent has been submitted for the present invention. It is entitled *A Selective Laser Melting process using pulsed* *lasers for building objects* (*V/Réf.:6.0932 N/Réf.:P2068EP0P/13-95pg/am*). The main idea is to use laser alternatively in continuous mode and in pulsed mode to selectively build the object and the supports.

6.4.1 Background

In all Additive Manufacturing techniques, supports are needed when the object to build has overhangs of more than 30 degrees. An example of support structure is shown in figure 6.12 (supports in red). They have three functions:

- Avoid the collapsing of the object due to gravity during construction
- Avoid the destruction or displacement of the object by the powder deposition system (blade, hopper, etc.)
- Ensure regular thermal conditions in the consolidation zone, for example by evacuating heat to avoid intense local fusion

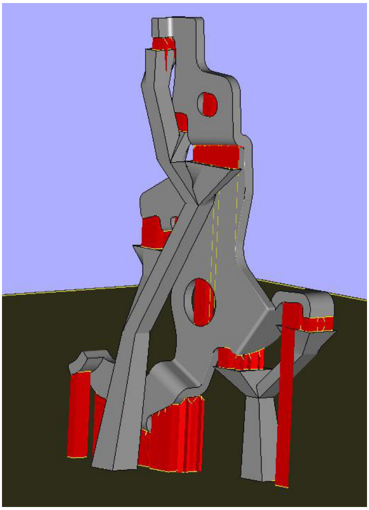

Figure 6.12: Example of support structure

For Selective Laser Melting the last two functions are the most important. The first one can be ignored since the object is built on a supporting powder bed.

The support structures are thus inevitable but pose many problems.

1. Time and material are needed to build them.
2. Their creation requires complex actions in CAD design which do not exist in commercial softwares.
3. After their building, the support structures have to be taken off the finished object. This process is difficult because access is often limited. It also leaves marks on surfaces which can be incompatible with aesthetical requirements.

To avoid the last disadvantage the support structure are usually designed in a way to minimize contact with the object. Since the obtained structure is more fragile, a compromise has to be found.

6.4.2 Support structure in pulsed mode

Today in SLM machines continuous laser are used to melt the powder completely . The quantity of liquid and the time it takes to get back to solid state can be influenced by the laser parameters. It can be shown that metallic particles undergo only superficial melting under short laser pulses. This is excellent for accuracy because the liquid has no time to spread. It only forms bonding between the particles. But the obtained objects are porous and their mechanical properties are much inferior to dense objects made with continuous lasers.

The idea of this invention is to use a pulsed radiation to create the supports, and a continuous radiation to build the objects. One may use two lasers or preferably the same laser in two modes. The resulting supports should have sufficient mechanical properties to resist to the deposition system and to evacuate heat, and should be easy to remove from the denser parts. Moreover designing complex support structures by CAD would not be anymore needed. Plain and simple supporting blocks should be sufficient.

6.4.3 Precise description of the building

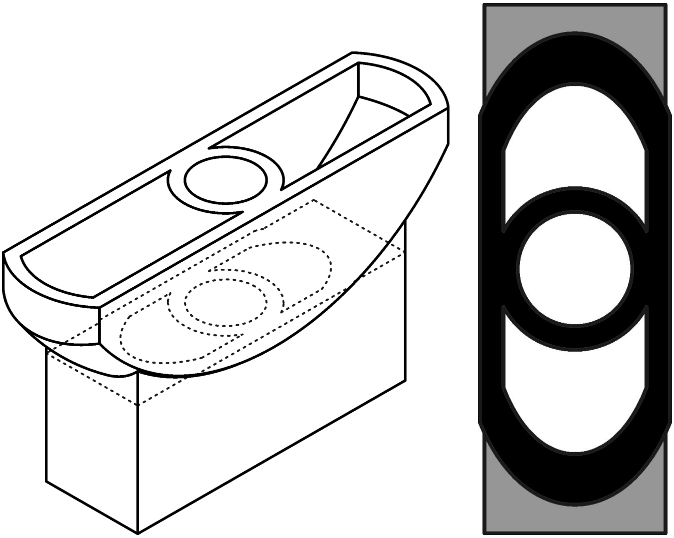

(a) (b)

Figure 6.13: A layer during the building of support structure

Figure 6.13(a) shows an example of an object with a block support structure. On figure 6.13(b) one can see a precise layer during the building of this part. The detailed procedure is the following :

1. a layer of powder is deposited on all of the bed
2. the object (black) is scanned by the laser in continuous mode
3. the support structure (grey) is scanned by the laser in pulsed mode

Then the same procedure is repeated for all the layers. At the end of the building process, the support structure is removed by sandblasting or by an equivalent process.

6.4.4 Preliminary experiments

Preliminary experiments have been made on silver objects (the silver powder is described in section 2.3.3) and the results are as expected (see figure 6.14).

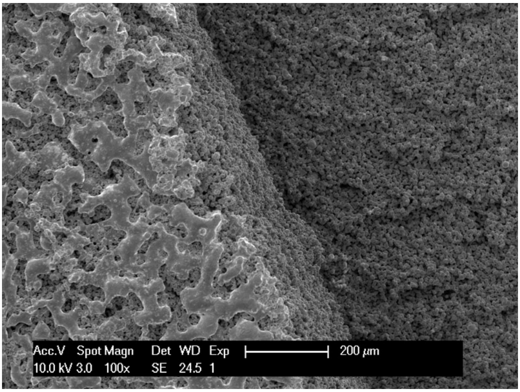

Figure 6.14: Supports made by pulsed laser (left side: piece in continuous mode / right side: support in pulsed mode)

It can be seen on the picture that the consolidation of the object is very different between the support part in pulsed mode (right) and the object in continuous mode (left). The mechanical properties are different as well, and, although the object is not fully dense, the support structure can be easily dissociated from the object, leaving it intact.

6.4.5 Perspectives

This new way to build support structure is a promising method to avoid most of the disadvantages of the usual structures. The CAD file is easy to generate, the building facilitated by the possibility to use plain blocks and the removing is simple and safe. One of the difficulty for the implementation of this technique in commercial SLM machines is that some of them use a fiber laser, which cannot be pulsed. The use of a Nd:YAG laser would overcome this problem.

6.5 Conclusion

Some examples of pieces built during this work are presented in sections 6.1, 6.2, 6.3 and 6.4. They are made with different powders and parameter sets. Density and accuracy have been measured for each of them, and a benchmark study allowed for a comparison between the different parts. A new way to build support structure has been proposed. The scanning strategies described in Chapter 5 have not yet been implemented for the building of pieces, due to the lack of software able to generate suitable CAD files. The use of paintbrush scanning or chessboard scanning should improve the density of the final parts.

The pieces presented in this chapter use both continuous and pulsed laser. Because they are made of different metallic powders, with very different physical properties, the range of useful laser parameters varies for each of them. Usually the laser parameter optimization is long and requires many experiments and iterations. Therefore the simulations described in Chapters 3, 4 and 5 are simple and unexpensive tools to rapidly determine the ranges of optimal laser parameters and scanning strategies leading either to accuracy or density, depending of the final application.

Chapter 7

Conclusion

7.1 Summary

Thanks to the development of an adequate SLS/SLM experimental platform, the consolidation process has been studied.

At a microscopic point of view, the formation of the interparticular neck has been observed with an innovative method allowing to isolate two particles and to illuminate them several times, taking electron micrographs of each step. Post-processing of these results is then made.

- The experimental results are compared with the predictions of a thermal model describing the interaction between a laser beam and a (spherical) grain. Two entries of this model, the absorption coefficient α of the laser into the grain and the heat exchange coefficient κ with the exterior are found using an original method. The thermal model leads to good predictions of the particles final sintering state.
- Two fluid flow models are derived to deduce from experimental results the so-called liquid lifetime during the formation of the interparticular neck. Although they are based on different considerations and hypotheses, the same results are found.

At a macroscopic point of view, four different scanning strategies have been investigated, in order to increase the final part density. A major conclusion of this study is that thermal gradients have to be limited. The experiments on a conductive and a non-conductive powder are compared to a three-dimensional model describing the laser-matter interactions and the temperature evolution of the scanned powder bed. This model is found to be an inexpensive and efficient way to qualify the drawbacks and the benefits of a given scanning strategy since it is able to detect overheated zones or high temperature gradients.

These studies are finally applied to the fabrication of several pieces. Different powders are compared via a benchmark study. Finally, a new way to build support structures during the construction, combining pulsed and continuous laser, is presented.

7.2 Perspectives

7.2.1 SLS

The developed experimental setup is able to give quantitative informations on powders of any composition and size (>10 μm). Combined to the derived thermal model, the final sintering state of the powder can be simulated for any laser parameters (power, pulse frequency, scan speed,..). The two fluid flow models give the possibility to compute the liquid lifetime directly from geometrical informations measured experimentally. However, a correct interpretation of the liquid lifetime should still be defined before comparing successfully our experimental results to numerical simulations of the sintering process (e.g. single-grain-like models).

7.2.2 SLM

Using the proposed numerical model, one can easily determine which scanning strategies can be efficient in limiting thermal gradients. The experimental work of optimizing both the laser parameters and scanning strategies should be greatly simplified and reduced to a small amount of precise experiments. EBSD analysis has proved to be an efficient way of studying the grain orientation.

In the future, the numerical models could be combined to selection algorithms (e.g. genetic algorithms) in a computer-based tool for generating automatically adapted scanning strategies.
Finally, the new method to build support structures should avoid most of the usual problems linked to their conception, their fabrication and their removing.

Appendix A

Washburn model: details

We consider a fluid of density ρ and viscosity μ which moves radially between two parallel plates (in the Oyz plane). The plates are spaced by a distance h (see figure A.1). We call γ_{LG} the surface tension between the liquid and the gas and the fluid cylinder has a radius R at time t (see figure A.1).

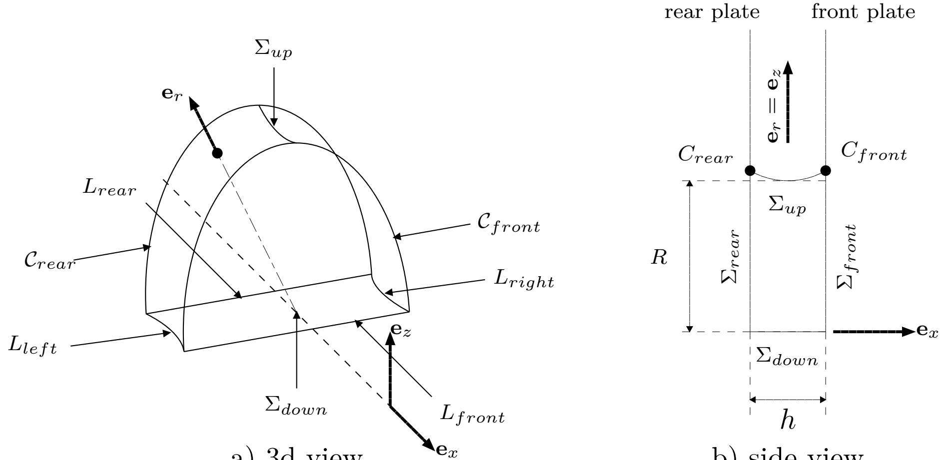

a) 3d view

b) side view

Figure A.1: The fluid between the plates

The fluid in the upper fluid domain undergoes the action of various external forces oriented in the $z-$direction (see figure A.1):

a) capillary forces related to the liquid-gas, liquid-solid and gas-solid interfaces,

b) pressure forces on the free surfaces,

c) friction forces on the interface between the fluid and the plates.

They are discussed in the following paragraphs:

A.1 Capillary forces

The capillary forces act along the curves delimiting the fluid domain (see Fig. A.1). There exist tow types of curves:

i) the curves $L_{right}, L_{rear}, L_{left}$ and L_{front} where only two phases (liquid-gas or liquid-solid) meet and which are called double curves,

ii) the curves C_{front} and C_{rear} where the three phases (liquid, solid and gas) meet and which are called triple curves.

A.1.1 Solid-gas capillary forces

We denote by $\mathbf{F}_{SG}^{cap}$ the result of the capillary forces linked to the interfaces solid–gas. The subscript S and G stand respectively for $\underline{\text{s}}$olid, $\underline{\text{g}}$as. The force $\mathbf{F}_{SG}^{cap}$ is expressed as a line integral along the curves where the plates and the gas meet. From Fig. A.1 it can be seen that only the triple curves C_{front} and C_{rear} are concerned. The solid-gas force pushes the fluid in the $\mathbf{e}_r$ direction (see Fig. A.1b)) and it has a linear density proportional to the solid-gas surface tension γ_{SG}. The conclusion is that

$$\mathbf{F}_{SG}^{cap} = \int_{C_{front} \cup C_{rear}} \gamma_{SG} \mathbf{e}_r \, \mathrm{d}l$$

After integration, we come to the conclusion that $\mathbf{F}_{SG}^{cap}$ is oriented in the $z-$direction with the amplitude

$$F_{SG}^{cap} = 4R\gamma_{SG}. \tag{A.1}$$

A.1.2 Solid-liquid capillary forces

We denote by $\mathbf{F}_{SL}^{cap}$ the result of the capillary forces linked to the interfaces solid-liquid. The subscript S and L stand again for $\underline{s}$olid and $\underline{l}$iquid. The force $\mathbf{F}_{SL}^{cap}$ is expressed as a line integral along the curves where the liquid meet the plates. From Fig. A.1 it can be observed that C_{front}, C_{rear} are a priori concerned as well as L_{front}, L_{rear}. It turns out that the triple curves C_{front} and C_{rear} do not actually contribute. The reason is that the solid-liquid interface bounded by those curves is a part of the considered body and the corresponding capillary forces are **internal** and not **external** and should not be taken into account in the momentum equation. As a consequence, the only solid-liquid capillary forces to consider are along the double lines L_{front}, L_{rear}. They are pulling the fluid in the $-\mathbf{e}_z$ direction (see Fig. A.1a)) and their linear density is proportional to the solid-liquid surface tension γ_{SL}:

$$\mathbf{F}_{SL}^{cap} = -\int_{L_{front} \cup L_{rear}} \gamma_{SL} \mathbf{e}_z \, \mathrm{d}l$$

After integration and taking into account that L_{front} and L_{rear} have the same length: $2R$ (see Fig. A.1a)), we come to the conclusion that $\mathbf{F}_{SL}^{cap}$ is oriented in the $z-$direction with the amplitude

$$F_{SL}^{cap} = -4R\gamma_{SL}. \tag{A.2}$$

A.1.3 Liquid-gas capillary forces

The last capillary force to consider is linked to the interface Σ_{up} between the liquid and the gas. The resultant is denoted $\mathbf{F}_{LG}^{cap}$ and can be computed as a line integral along the boundary $\partial\Sigma_{up}$ of the surface Σ_{up}. The density to integrate is $\gamma \mathbf{t} \times \mathbf{n}$ where $\gamma = \gamma_{LG}$ is the liquid-gas surface tension and where **n** is the outside normal to Σ_{up} and **t** the tangent to $\partial\Sigma_{up}$ positively oriented with respect to **n** (see Fig. A.2):

$$\mathbf{F}_{LG}^{cap} = \int_{\partial\Sigma_{up}} \gamma \mathbf{t} \times \mathbf{n} \, \mathrm{d}l.$$

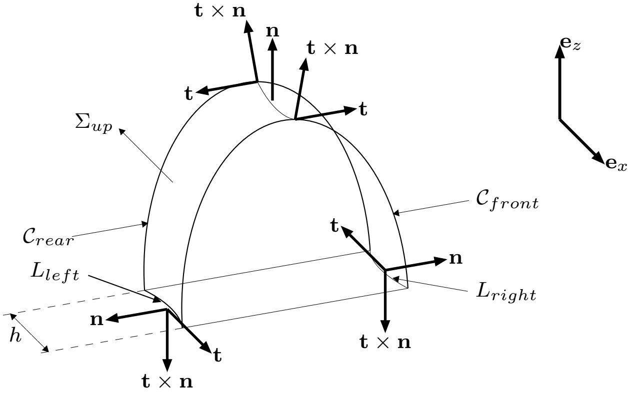

Figure A.2: The outside normal **n**, the positively oriented tangent **t** and the direction $\mathbf{t} \times \mathbf{n}$ of the liquid-gas capillary forces density.

To use the Washburn-Lucas hypothesis in the best conditions, we have to express $\mathbf{F}_{LG}^{cap}$ as a surface integral over Σ_{up}. To do this, we use the Stokes theorem. It tells that the line integral of $\gamma\mathbf{t} \times \mathbf{n}$ over $\partial\Sigma_{up}$ is opposite to the integral of the Laplace pressure[1] p_{lap} over Σ_{up}. The result is

$$\mathbf{F}_{LG}^{cap} = -\int_{\Sigma_{up}} p_{lap}\mathbf{n} \, \mathrm{d}\sigma.$$

---

[1] The Laplace pressure is connected to the curvature κ of Σ_{up}, $p_{lap} = \gamma\kappa$. By convention, the curvature κ is positive if the curvature center is inside Σ_{up}.

By considering the local equilibrium of any portion of the interface Σ_{up}, we can connect the Laplace pressure to the external pressure p_{out} and to the hydrostatic pressure p_{in} of the fluid: $p_{lap} = p_{in} - p_{out}$. The final expression we get for $\mathbf{F}_{LG}^{cap}$ is

$$\mathbf{F}_{LG}^{cap} = \int_{\Sigma_{up}} (p_{out} - p_{in})\mathbf{n}\,\mathrm{d}\sigma. \tag{A.3}$$

A.2 Pressure forces

The forces we consider here are the pressure forces on the free surfaces Σ_{up} and Σ_{down} (see figure A.1) with outside normal $\mathbf{n}$. The expression we find for their sum is

$$\mathbf{F}^{pres} = -\int_{\Sigma_{up}} p_{out}\mathbf{n}\,\mathrm{d}\sigma - \int_{\Sigma_{down}} p_{in}\mathbf{n}\,\mathrm{d}\sigma.$$

where the notations p_{out} and p_{in} are used for the external pressure and, respectively, the fluid hydrostatic pressure (see paragraph A.1). The *first part of the Washburn-Lucas hypothesis* consists of replacing the integral over Σ_{down} by an integral over the upper surface Σ_{up}:

$$\mathbf{F}^{pres} = -\int_{\Sigma_{up}} (p_{out} - p_{in})\mathbf{n}\,\mathrm{d}\sigma. \tag{A.4}$$

This assumption is justified if the fluid is closed to its equilibrium state. In the equilibrium state, the hydrostatic equation $\mathrm{grad}\, p_{in} = 0$ is valid and the sum of $p_{in}\mathbf{n}$ over Σ_{up} and Σ_{down} are opposed because of the gradient Theorem.

A.3 Viscosity forces at the interface fluid-plates

The last forces that we consider are the viscous friction forces acting on the interfaces Σ_{front} and Σ_{rear} (see Fig. A.1) of outside normal $\pm\mathbf{e}_x$.

These forces are obtained by integrating the shear stress σ_{rx}. We get the following formula for their sum $\mathbf{F}^{vis}$

$$\mathbf{F}^{vis} = \int_{\Sigma_{front}} \sigma_{rx}\mathbf{e}_r \mathrm{d}\sigma - \int_{\Sigma_{rear}} \sigma_{rx}\mathbf{e}_r \mathrm{d}\sigma.$$

The *second part of the Washburn-Lucas hypothesis* helps us to identify the shear stress. We assume that σ_{rx} takes the same value as in a steady radial flow with a corresponding total mass flow $Q = 2\pi Rh\dot{R}$ (see [77]). This assumption is justified by the fact that, far from the meniscus Σ_{up}, the fluid flow approaches a flow with adhesion conditions on the plates [40]. If we assume that the origin of the $x-$axis lies in the middle between the plates, one gets

$$\sigma_{rx} = \sigma_{rx}(x, r) = -\frac{6\mu Q}{\pi h^3 r}x$$

and after integration and taking into account that the surfaces Σ_{front} and Σ_{rear} are semi-circles, we conclude that $\mathbf{F}^{vis}$ is collinear to $\mathbf{e}_z$ with an amplitude

$$F^{vis} - \frac{12\mu R^2\dot{R}}{h}. \tag{A.5}$$

A.4 Balance equation

The equation of motion in the $z-$direction involves the component P of the fluid momentum along $\mathbf{e}_z$. It reads

$$\frac{d}{dt}P = F_{LG}^{cap} + F_{SG}^{cap} + F_{SL}^{cap} + F^{vis} + F^{pres}$$

where F_{LG}^{cap} and F^{pres} are the $z-$components of the capillary force (A.3) and of the pressure force (A.4) and where F_{SG}^{cap}, F_{SL}^{cap} and F^{vis} are as in (A.1), (A.2) and (A.5). The momentum $\mathbf{P}$ is obtained by suming the momentum density over the fluid domain. The *third part of the Washburn-Lucas hypothesis* assumes that the radial fluid velocity is homogeneous, with an amplitude $\dot{R}$ and leads to a simple expression for the momentum density: $\rho\dot{R}\mathbf{e}_r + \upsilon\mathbf{e}_x$ where υ is an unkown (and unimportant) axial velocity. If we neglect the meniscus curvature in the x direction, the fluid domain is a semi-cylinder (see Fig. A.1) and the momentum in the $z - direction$ is $P = \rho h R^2 \dot{R}$.

The forces on the right-hand side of the equation of motion may now be replaced by their expressions (A.1)-(A.5). The main observation is that the the capillary force F_{LG}^{cap} between the liquid and the gas annihilates the pressure force[1] F^{pres}. After further simplifications, we end up with a scalar relation

$$\rho(R\ddot{R} + 2\dot{R}^2) = \frac{4\gamma_{LG}}{h}\cos\theta_E - \frac{12\mu}{h^2}R\dot{R}. \tag{A.6}$$

---

[1] This is actually the direct consequence of the second part in the Washburn-Lucas hypothesis.

Appendix B

Pictures for the determination of the critical times t_1^* and t_2^*

Figures B.1 and B.2 are taken using Method B (see section 3.2.2) and used for the determination of the critical times t_1^* and t_2^* related to the powers P_1=5.8 W and P_2=4.2 W (see section 3.3.1). The transition between non-molten and molten powder turns to be sharp and thus the determination of the critical times is quite obvious.

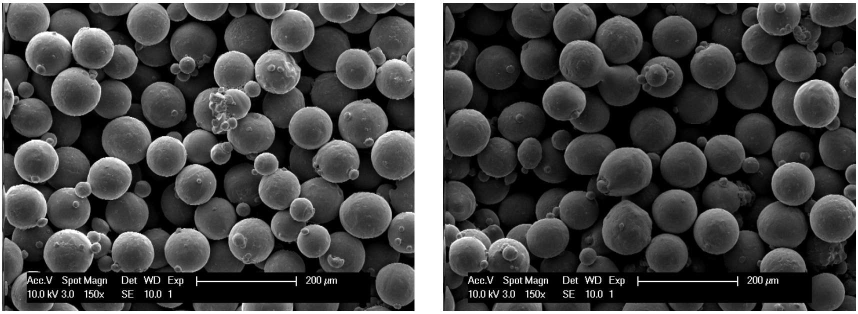

(a) t=25 ms

(b) t=30 ms

Figure B.1: Determination of the critical time t_1^*

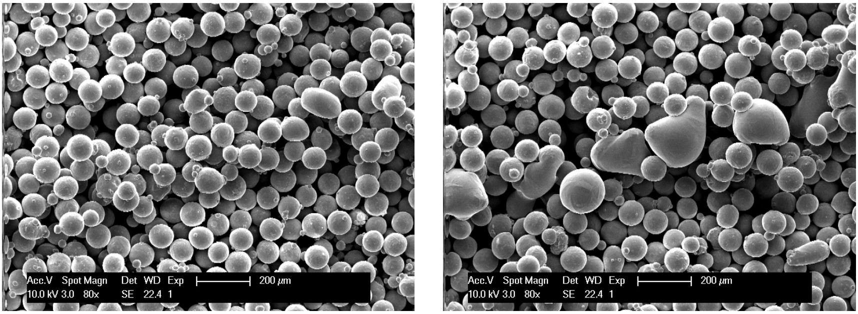

(a) t=50 ms

(b) t=60 ms

Figure B.2: Determination of the critical time t_2^*

Appendix C

Effect of the Π-shaper

The beam shape without Π-shaper is shown on figure C.1. The beam shape after using the Π-shaper is depicted in figure C.2.

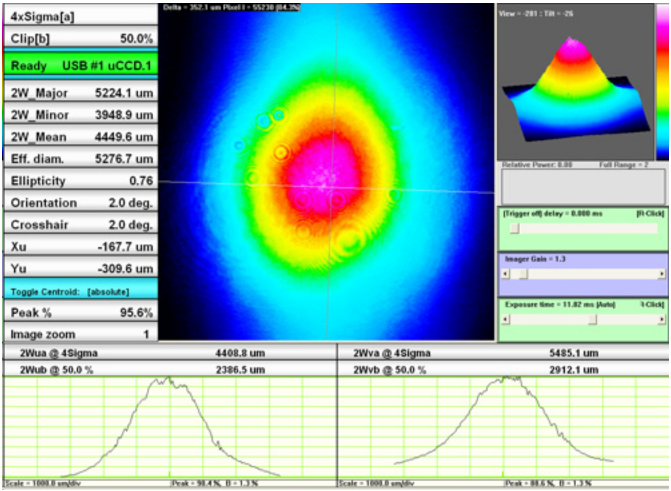

4xSigma[a]
Clip[b] 50.0%
Ready USB #1 uCCD.1
2W_Major 5224.1 um
2W_Minor 3948.9 um
2W_Mean 4449.6 um
Eff. diam. 5276.7 um
Ellipticity 0.76
Orientation 2.0 deg.
Crosshair 2.0 deg.
Xu -167.7 um
Yu -309.6 um
Toggle Centroid: [absolute]
Peak % 95.6%
Image zoom 1

Delta = 352.1 um Pixel I = 55230 (84.3%)
View = -281 : Tilt = -26
Relative Power: 0.00 Full Range = 2
[Trigger off] delay = 0.000 ms [R-Click]
Imager Gain = 1.3
Exposure time = 11.82 ms [Auto] 1-Click]

2Wua @ 4Sigma 4408.8 um
2Wub @ 50.0 % 2386.5 um
2Wva @ 4Sigma 5485.1 um
2Wvb @ 50.0 % 2912.1 um

Scale = 1000.0 um/div
Peak = 90.4%, B = 1.3%
Scale = 1000.0 um/div
Peak = 88.6%, B = 1.3%

Figure C.1: Beam without Π-shaper

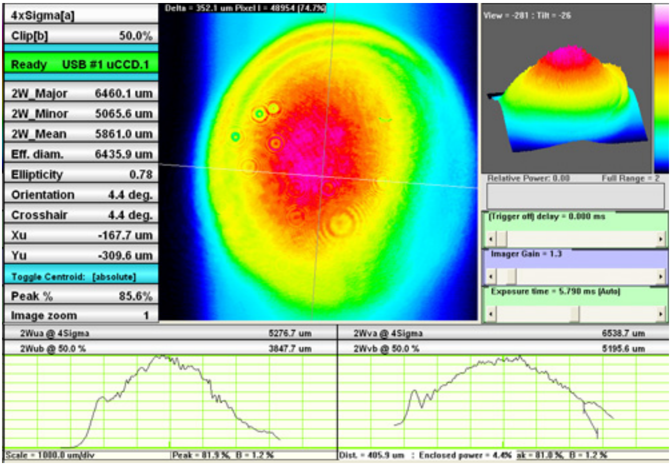

4xSigma[a]
Clip[b] 50.0%
Ready USB #1 uCCD.1
2W_Major 6460.1 um
2W_Minor 5065.6 um
2W_Mean 5861.0 um
Eff. diam. 6435.9 um
Ellipticity 0.78
Orientation 4.4 deg.
Crosshair 4.4 deg.
Xu -167.7 um
Yu -309.6 um
Toggle Centroid: [absolute]
Peak % 85.6%
Image zoom 1
Delta = 352.1 um Pixel I = 48954 (74.7%)
View = -281 : Tilt = -26
Relative Power: 0.00 Full Range = 2
(Trigger off) delay = 0.000 ms
Imager Gain = 1.3
Exposure time = 5.790 ms (Auto)
2Wua @ 4Sigma 5276.7 um
2Wub @ 50.0 % 3847.7 um
2Wva @ 4Sigma 6538.7 um
2Wvb @ 50.0 % 5195.6 um
Scale = 1000.0 um/div
Peak = 81.9 %, B = 1.2 %
Dist. = 405.9 um : Enclosed power = 4.4% ak = 81.8 %, B = 1.2 %

Figure C.2: Beam with Π-shaper

Since these images are taken with the camera described in section 2.1.1 and thus before the focalistation lens, figures C.1 and C.2 do not reflect the laser beam shape at the focal point, but its Fourier transform in order to get respectively gaussian and top-hat shapes at the focal point [78].

Bibliography

[1] Castle Island. Worldwide guide to rapid prototyping. http://home.att.net/ castleisland/home.htm.

[2] N.Karapatis, J.P.S.van Griethuysen, and R.Glardon. Direct rapid tooling: A review of current research. *Rapid Prototyping Journal*, 4(2):77–89, 1998.

[3] N.Karapatis. *A Sub-Process approach of Selective Laser Sintering*. PhD thesis, EPFL, 2002. No.2506.

[4] G.N.Levy, R.Schindel, and J.P.Kruth. Rapid manufacturing and rapid tooling with layer manufacturing (lm) technologies, state of the art and future perspectives. *CIRP Annals - Manufacturing Technology*, 52(2):589 – 609, 2003.

[5] I.Yadroitsau. *Fabrication directe d'objets 3D par fusion sélective laser à partir des poudres métalliques*. PhD thesis, Université Jean-Monnet, 2008.

[6] T.Wohlers. *Wohlers report 2009*. Wohlers Associates, 2009.

[7] R.P.George. A response to "triz on rapid prototyping - a case study for technology foresight". *The TRIZ Journal*, oct 2007.

[8] L.Castillo. Study about the rapid manufacturing of complex parts of stainless steel and titanium. *TNO report with the collaboration of AIMME*, 2005.

[9] J.P.Kruth, P.Mercelis, L.Froyen, and M.Rombouts. Binding mechanisms in selective laser sintering and selective laser melting. In D.L.Bourell, J.J.Beaman, R.H.Crawford, H.L.Marcus, and J.W.Barlow, editors, *Proceedings of the 10th Solid Freeform Fabrication Symposium*, Austin, Texas, 2004.

[10] F.Abe, K.Osakada, Y.Kitamura, M.Matsumoto, and M.Shiomi. Manufacturing of titanium parts for medical purposes by selective laser melting. In *Proc. 8th Int. Conf. Rapid Prototyping*, 2000.

[11] EOS Electro Optical Systems. `http://www.eos.info/`.

[12] Phenix Systems. `http://www.phenix-systems.com/`.

[13] J.P.Kruth, B.Vandenbrouke, J.Vaerenbergh, and P.Mercelis. Benchmarking of Different SLS-SLM Processes as Rapid Manufacturing Techniques. In *Int.Conf.Polymers & Moulds Innovations*, Gent,Belgium, April 20-23, 2005.

[14] S.Kolossov. *Non-Linear Model and Finite Element Simulation of the Selective Laser Sintering Process*. PhD thesis, EPFL, 2005. 3178.

[15] C.André. *Modélisation quantitative du procédé de frittage sélectif par laser: relation paramètres/microstructure*. PhD thesis, EPFL, 2007. 3716.

[16] M.Borkovec and W.De Paris. The fractal simension of the apollonian sphere packing. *Fractals*, 2(4):521–526, 1994.

[17] R.K.McGeary. Mechanical packing of spherical particles. *J. Amer. Ceram. Soc.*, 44:513, 1961.

[18] J.A.Elliott, A.Kelly, and A.H.Windle. Recursive packing of dense particle mixtures. *Journal of material science*, 21:1249–1251, 2002.

[19] Alfa Aesar. http://www.alfa-chemcat.com.

[20] Sandvik Osprey Ltd. http://www.smt.sandvik.com/.

[21] Nippon Atomized Metal Powders Corporation. http://www.atomize.co.jp.

[22] Hilderbrand et Cie Sa. http://www.hilderbrand.ch.

[23] C.M. Fernandesa, V.M. Ferreiraa, A.M.R. Senosa, and M.T. Vieirab. Stainless steel coatings sputter-deposited on tungsten carbide powder particles. *Surface and Coatings Technology*, 176:103–108, 2003.

[24] M.Dafflon, B.Lorent, and R.Clavel. A micromanipulation setup for comparative tests of microgrippers. *ISR06, Münich*, 2006.

[25] A.J.Schwartz, M.Kumar, and B.L.Adams. *Eletron Backscatter Diffraction in Materials Science*. Kluwer Academic/Plenum Publishers, 2000.

[26] D.Favez. *Soudage laser or-acier: métallurgie et procédé*. PhD thesis, EPFL, 2009. 4353.

[27] G.Arthur. Porosity and permeability changes during the sintering of copper powder. *J. Inst. Metals*, 83(7):329–336, 1954-1955.

[28] R.Morgan, C.J.Sutcliffe, and W.O'Neill. Density analysis of direct metal laser re-melted 316l stainless steel cubic primitives. *Journal Of Materials Science*, 39:1195–1205, 2004.

[29] R.M.German. *Sintering theory and practice*. Wiley and Sons, 1996.

[30] F.Klocke and C.Wagner. Coalescence behaviour of two metallic particles as base mechanism of selective laser sintering. *CIRP Ann Manuf Technol*, 52(1):177–180, 2003.

[31] N.K.Tolochko, S.E.Mozzharov, I.A.Yadroitsev, T.Laoui, L.Froyen, V.I.Titov, and M.B.Ignatiev. Balling processes during selective laser treatment of powders. *Rapid Prototyping Journal*, 10(2):78–87, 2004.

[32] P.Fischer, H.Leber, V.Romano, H.P.Weber, N.Karapatis, C.André, and R.Glardon. Microstructure of near infrared pulsed laser sintered Titanium samples. *Applied Physics A*, 2003. published online.

[33] P.Fischer, V.Romano, H.P.Weber, N.P.Karapatis, E.Boillat, and R.Glardon. Sintering of commercially pure Titanium powder with a Nd:YAG laser source. *Acta Materialia*, 51(6):1651–1662, 2003.

[34] G.Mie. Beiträge zur Optik trüber Medien, speziell kolloidaler Metallösungen. *Ann.Phys.*, 25(4):377–445, 1908.

[35] E.Boillat. Détermination des coefficients de transfert et d'absorption. LGPP internal archives, 2009.

[36] E.Magenes, R.H.Nochetto, and C.Verdi. Energy error estimates for a linear scheme to approximate nonlinear parabolic problems. *Mathematical modelling and numerical analysis*, 21(4):655–678, 1987.

[37] W.J.Huppmann and H.Riegger. Modelling of rearrangement processes in liquid phase sintering. *ACTA METTALURGICA*, 23:965–971, 1975.

[38] L.A.Anestiev and L.Froyen. Model of the primary rearrangement processes at liquid phase sintering and selective laser sintering due to biparticle interaction. *Journal of Applied Physics*, 86(7):4008–4017, 1999.

[39] Y.D.Shikhmurzaev. Moving contact lines in liquid-liquid-solid systems. *J.Fluid Mech*, 334:211–249, 1997.

[40] M.K.Schwiebert and W.H.Leong. Underfill flow as viscous flow between parallel plates driven by capillary action. *Components, Packaging, and Manufacturing Technology, Part C, IEEE Transactions on*, 19(2):133–137, Apr 1996.

[41] E.W.Washburn. The dynamics of capillary flow. *Physical review*, 17(3):273–283, 1921.

[42] B.V.Zhmud, F.Tiberg, and K.Hallstensson. Dynamics of capillary rise. *Journal of colloid and interface science*, 228(2):263–269, 2000.

[43] S.Levine, J.Lowndes, E.J.Watson, and G.Graham Neale. A theory of capillary rise of a liquid in a vertical cylindrical tube and in a parallel-plate channel. *Journal of Colloid and Interface Science*, 73(1):136–151, 1980.

[44] C.Huh and S.G.Mason. The steady movement of a liquid meniscus in a capillary tube. *Journal of Fluid Mechanics Digital Archive*, 81(03):401–419, 1977.

[45] T.D.Blake. The physics of moving wetting lines. *Journal of Colloid and Interface Science*, 299(1):1 – 13, 2006.

[46] Y.D.Shikmurzaev. *Capillary flows with forming interfaces.* Chapman and Hall, 2008.

[47] C.Huh and L.E.Scriven. Hydrodynamic model of steady movement of a solid/liquid/fluid contact line. *Journal of colloid and interface science*, 35(1):85, 1971.

[48] O.V.Voinov. Hydrodynamics of wetting. *Fluid.Dyn.*, 11:714–721, 1976.

[49] H.K.Moffat. Viscous and resistive eddies near a sharp corner. *J.Fluid Mech.*, 18, 1964.

[50] E. B.Dussan. On the spreading of liquids on solid surfaces: static and dynamic contact lines. *Annual Review of Fluid Mechanics*, 11(1):371, 1979.

[51] C.Huh and S.G.Mason. Effects of surface roughness on wetting (theoretical). *Journal of colloid and interface science*, 60(11), 1977.

[52] C.G.Ngan and E.B.Dussan. On the dynamics of liquid spreading on solid surfaces. *Journal of Fluid Mechanics*, 209:191, 1989.

[53] R.L.Hoffman. A study of the advancing interface. *Journal of Colloid and Interface Science*, 50(2):228, 1975.

[54] L.H.Tanner. The spreading of silicone oil drops on horizontal surfaces. *J.Phys.D: Appl.Phys.*, 12:1473–1785, 1979.

[55] S.Schiaffino-A.A.Sonin. On the theory for the arrest of an advancing molten contact line on a cold solid of the same material. *Phys.Fluids*, 9(8):2227–2233, 1997.

[56] J.Koplik, J.R.Banavar, and J.F.Willemsen. Molecular dynamics of poiseuille flow and moving contact lines. *Physical review letters*, 60(13):1282, 1988.

[57] P.A.Thompson and M.O.Robbins. Simulations of contact-line motion: slip and the dynamic contact angle. *Physical review letters*, 63(7):766, 1989.

[58] Y.D.Shikhmurzaev. The moving contact line on a smooth solid surface. *International Journal of Multiphase Flow*, 1993.

[59] Y.D.Shikhmurzaev. Mathematical modeling of wetting hydrodynamics. *Fluid Dynamics Research*, 13(1):45 – 64, 1994.

[60] E. Schäffer and P. Wong. Contact line dynamics near the pinning threshold: A capillary rise and fall experiment. *Phys. Rev. E*, 61(5):5257–5277, May 2000.

[61] W.P.Kotorynski. Viscous flow in axisymmetric pipes with slow variations. *Computers and fluids*, 24(6):685–717, 1994.

[62] W.F.Gale and T.C.Totemeier. *Smithells Metals Reference Book (8th Edition).* Elsevier Butterworth-Heinemann, 2004.

[63] H.Pohl, A.Simchi, I.Munther, and H.Calefi Dias. Thermal stresses in direct metal laser sintering. In D.L.Bourell and al., editors, *Solid Freeform Fabrication Symposium Proceedings*, pages 366–372, 2001.

[64] M. Rombouts, J.P. Kruth, L. Froyen, and P. Mercelis. Fundamentals of selective laser melting of alloyed steel powders. *CIRP Annals - Manufacturing Technology*, 55(1):187 – 192, 2006.

[65] P. Mercelis and J.P. Kruth. Residual stresses in selective laser sintering and selective laser melting. *Rapid Prototyping Journal*, 12(5):254–265, 2006.

[66] L.Ma and H.Bin. Temperature and stress analysis and simulation in fractal scanning-based laser sintering. *The International Journal of Advanced Manufacturing Technology*, 34(9):898–903, 2007. 10.1007/s00170-006-0665-5.

[67] M.F. Zaeh, G. Branner, and T.A. Krol. A three dimensional fe-model for the investigation of transient physical effects in selective laser melting. In P.J.Bártolo et al., editor, *Innovative developments in design and manufacturing, Advanced Research in Virtual and Rapid Prototyping.* Taylor and Francis, 2009.

[68] A.V. Gusarov, I. Yadroitsev, Ph. Bertrand, and I. Smurov. Heat transfer modelling and stability analysis of selective laser melting. *Applied Surface Science*, 254(4):975 – 979, 2007. Laser synthesis and processing of advanced materials - E-MRS-P Symposium.

[69] G.H.Meyer. Multidimensional Stefan problems. *SIAM J.Numer.Anal.*, 10:522–538, 1973.

[70] A.V.Gusarov, T.Laoui, L.Froyen, and V.I.Titov. Contact thermal conductivity of a powder bed in selective laser sintering. *International Journal of Heat and Mass Transfer.*, 46:1103–1109, 2003.

[71] C.Argento and D.Bouvard. Modeling the effctive thermal conductivity of random packing of spheres through densification. *International Journal of Heat and Mass Transfer.*, 39(7):1343–1350, 1996.

[72] E.Boillat. Finite Element Methods on Non-Conforming Grids by Penalizing the Matching Constraint. *M2AN*, 37(2), 2003.

[73] MATWEB. Material Property Data. `http://www.matweb.com/`.

[74] J.D. Hunt. Steady state columnar and equiaxed growth of dendrites and eutectic. *Materials science and engineering*, 65(1):75–83, 1984.

[75] M.Rappaz, Ch.-A.Gandin, J.-L.Desbiolles, and Ph.Thévoz. Predicition of grain structure in various solidification processes. *Metallurgical and Materials Transactions A*, 27A, 1996.

[76] Hochschule für Technik in Windisch (CH). `http://www.fhnw.ch/technik/`.

[77] E.Boillat. Ecoulement de poiseuille stationnaire dans une symétrie polaire. LGPP internal archives, 2009.

[78] K.Lizuka. *Elements of Photonics*, volume 1. John Wiley & Sons, New York, 2002.

[79] J.Jhabvala, T.Antignac, E.Boillat, and R.Glardon. Study and simulation of different scanning strategies in SLM. In P.J.Bártolo et al., editor, *Innovative developments in design and manufacturing, Advanced Research in Virtual and Rapid Prototyping*. Taylor and Francis, 2009.

[80] J.Jhabvala, M.Dafflon, E.Boillat, and R.Glardon. Influence of the process parameters on the liquid bridges between particles in SLS. In P.J.Bártolo et al., editor, *Virtual and Rapid Manufacturing, Advanced Research in Virtual and Rapid Prototyping*, pages 553–558. Taylor and Francis, 2007.

Curriculum Vitae

Jamasp Jhabvala

Personal Information:
Date of birth: 7th December 1978.
Place of birth: Geneva, Switzerland.

Education:
2005-2010: PhD student at LGPP (Laboratoire de Gestion et Procédés de Production) at EPFL
2003: Master degree in Material Science at LC (Laboratoire de Céramiques) at EPFL
1998-2003: Student in Material Science at EPFL

Publications
2010: Influence of the thermal gradients on SLM pieces built with different scanning strategies. Submitted to *The International Journal of Advanced Manufacturing Technology*
2010: On the effect of scanning strategies in the Selective Laser Melting process. To be published in *Virtual and Physical Prototyping.*
2009: Study and simulation of different scanning strategies in SLM. In *Innovative developments in design and manufacturing, Advanced Research in Virtual and Rapid Prototyping.* See [79]. *Best Paper Award.*
2007: Influence of the process parameters on the liquid bridges between particles in SLS. In *Virtual and Rapid Manufacturing, Advanced Research in Virtual and Rapid Prototyping.* See [80].